NASA CONTRACTOR REPORT

NASA CR-1658

RESEARCH AND DEVELOPMENT STUDY OF A PERISTALTIC ACTION MICROINCH ACTUATOR

by Carlo La Fiandra

Prepared by
PERKIN-ELMER CORPORATION
Norwalk, Conn.
for Electronics Research Center

NATIONAL AERONAUTICS AND SPACE ADMINISTRATION • WASHINGTON, D. C. • SEPTEMBER 1970

1. Report No.	2. Government Accession No.	3. Recipient's Catalog No.
NASA CR-1658		

4. Title and Subtitle	5. Report Date
RESEARCH AND DEVELOPMENT STUDY OF A PERISTALTIC ACTION MICROINCH ACTUATOR	September 1970
	6. Performing Organization Code
7. Author(s)	8. Performing Organization Report No.
Carlo La Fiandra	
9. Performing Organization Name and Address	10. Work Unit No.
Perkin-Elmer Corporation Norwalk, Connecticut	11. Contract or Grant No. NAS 12-2012
	13. Type of Report and Period Covered Contractor Report
12. Sponsoring Agency Name and Address	
National Aeronautics and Space Administration Washington, D.C. 20546	14. Sponsoring Agency Code

15. Supplementary Notes
References: p. 116.

16. Abstract

The Perkin-Elmer Corporation undertook the task of developing microinch actuator technology and hardware capable of meeting the stringent requirements for either a segmented or a deformable active-optics space-qualified mirror system. The program objectives were met. The Perkin-Elmer Corporation successfully demonstrated a working peristaltic microinch actuator, and successfully advanced actuator technology. This report describes the various theories and models explaining the basis of operation of the actuator, the actuator itself, and the tests performed.

T: Peristaltic microinch actuator.

17. Key Words (Selected by Author(s))	18. Distribution Statement
1. Actuators 2. Mirrors	Unclassified - Unlimited

19. Security Classif. (of this report)	20. Security Classif. (of this page)	21. No. of Pages	22. Price*
Unclassified	Unclassified	122	$3.00

*For sale by the Clearinghouse for Federal Scientific and Technical Information Springfield, Virginia 22151

TABLE OF CONTENTS

LIST OF ILLUSTRATIONS

LIST OF ILLUSTRATIONS (Continued)

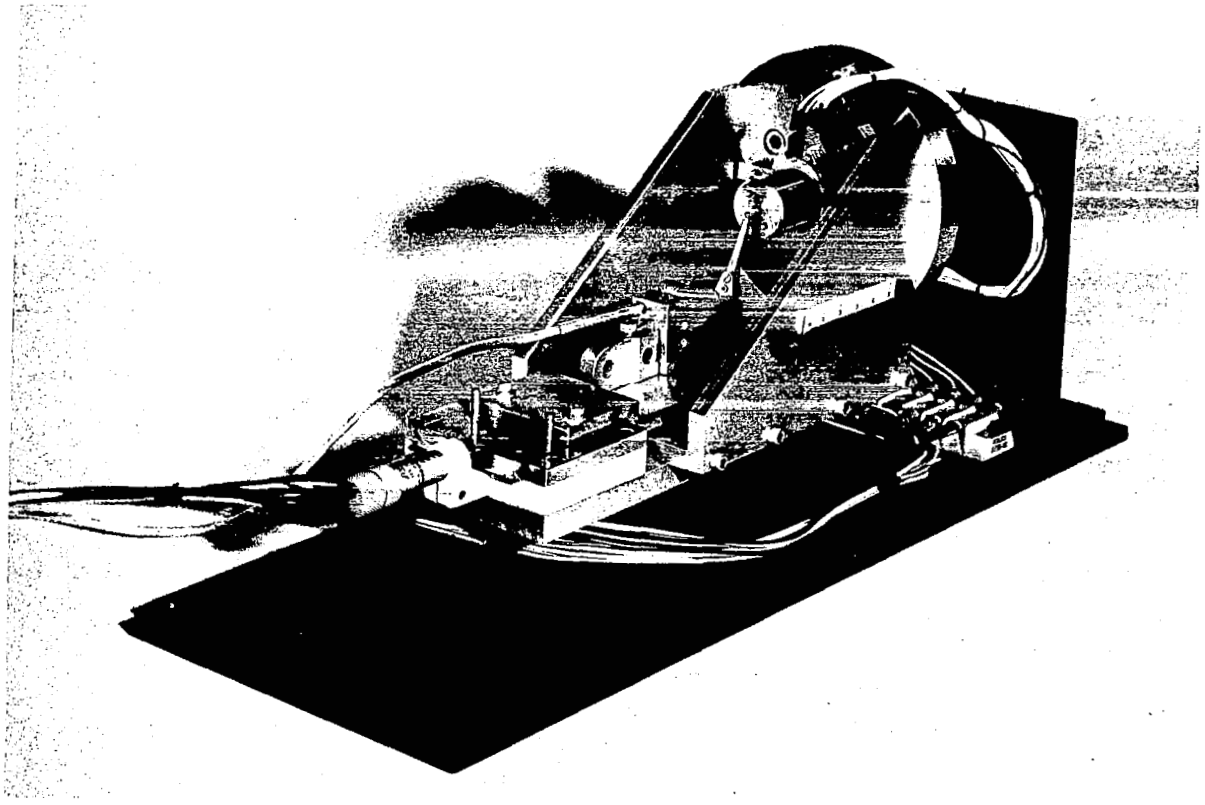

Actuator in Test Setup

RESEARCH AND DEVELOPMENT STUDY OF A PERISTALTIC ACTION MICROINCH ACTUATOR

By Carlo LaFiandra

The Perkin-Elmer Corporation
Norwalk, Connecticut

SUMMARY

The Perkin-Elmer Corporation undertook the task of developing microinch actuator technology and hardware capable of meeting the stringent requirements for either a segmented or a deformable active-optics space-qualified mirror system. The program objectives were met. The Perkin-Elmer Corporation successfully demonstrated a working peristaltic microinch actuator, and successfully advanced actuator technology. This report describes the various theories and models explaining the basis of operation of the actuator, the actuator itself, and the tests performed.

INTRODUCTION

This final report of the research and development study of a peristaltic action microinch actuator is being submitted at the completion of Contract No. NAS 12-2012 issued by the Electronics Research Center of the National Aeronautics and Space Administration.

A key element in the development of a primary mirror active optical system for an orbiting astronomical telescope is the actuator itself. The actuator device must provide the servo-controlled force and displacement with the necessary precision and reliability.

The developmental need for an actuator for the Segmented Optics became apparent in the Active Optical Systems for Space Stations Project (NASA Contract NAS 1-5198), and the actuator need is present also in the Deformable Active Optics work being done currently by Perkin-Elmer for Langley Research Center (Contract No. NAS 1-7103). Many ideas for actuators had been generated and tested by Perkin-Elmer in the laboratory in both of these two projects. The most promising of these ideas had been developed to the point where thorough investigation and development of 1/50 wavelength displacement was warranted.

This contract just completed directed the Perkin-Elmer Corporation to develop through analysis and evaluation the technology on fractional wavelength actuators and the necessary hardware. The Advanced Actuator Project objective was to develop actuator technology (in both theory and practice) that would meet the requirements described herein for precision, range, efficiency, response time, and reliability in a space-type environment. The project was centered around the actuator techniques that meet the requirements of space optical systems of the future.

The technique developed was the piezoelectric peristaltic actuator. The peristaltic actuator principle*, which should not be confused with the "inch worm" principle, is the result of extensive analysis and some laboratory testing.

*Invented by H. J. Robertson of Perkin-Elmer

We, at Perkin-Elmer, had developed and tested magnetostrictive peristaltic actuators designed for the Segmented Active Optics type of application. The problems associated with magnetic field fringing effects in a magnetostrictive unit are avoided by the piezoelectric type of unit.

We believe that the basic principle of peristaltic action for the actuator has advantages over the "inch-worm" principle because of the method of holding the armature. The peristaltic actuator uses multiple area contact between the armature and the sleeve, whereas, the "inch worm" used point or line contact between the armature and the sleeve. If desired, it is theoretically possible to operate the peristaltic actuator in an inch-worm mode.

The difference between the two principles manifests itself when both devices operate in small steps with load. The "inch worm" has basic technical problems in moving with small enough increments when a restraining load is present. It can be erratic and, when movement takes place, the step is generally too large for use in either a Segmented or Deformable Active Optics mirror system. We believe that part of the reason for the erratic motion is traceable to the point contact principle used in holding the stationary end of the actuator armature to the sleeve and/or the inevitable bending that results in inch-worm types of structures. The load is transferred from the armature to the sleeve via the two point contacts (or, at best, two line contacts). The load transfer is correspondingly concentrated and structural bending action takes place inside the device. The high loads are avoided in the peristaltic device since the load transfer from the armature to the sleeve takes place over numerous elements (or large areas). Thus, the peristaltic actuator does not have high concentrated loads and the corresponding bending in the elements is reduced significantly.

Perkin-Elmer investigated and applied the most appropriate techniques to solve the piezoelectric microinch actuator problem. We developed a practical actuator solution by conducting thorough analysis and evaluation in conjunction with carefully instructed laboratory work. The contract ran for a period of 14 months and did result in the furtherance of actuator technology along with working hardware. Both aspects of the development achieved program objectives. The hardware produced as a result of this contract

consisted of three types actuators working on essentially the same basic principle but modified slightly to help establish various performance parameters.

This report includes a complete description of the various analytical models describing actuator behavior and, in addition, a thorough description of the hardware and the various tests performed with it. The correlation between analytical and experimental results was demonstrated and is also presented.

DESCRIPTION OF ACTUATOR

Before discussing the actual construction features of the actuator, it is appropriate to briefly review the requirements since it is most important for the reader to understand the physical properties of an Active Optics type of actuator and to define technical difficulties that must be overcome to obtain these characteristics.

Requirements

$\lambda/50$ Wave displacement capability. -- The accuracy to which a diffraction-limited mirror should be figured in order to put 95 percent of the maximum possible energy into the central diffraction ring is 1/50 wavelength (RMS). It has been found possible to achieve this level of precision in monolithic mirrors such as the 36-inch solid fused-quartz mirror used in Stratoscope II, and to approach the value in the Segmented Active Optics. This is the standard of accuracy that will be required for future orbiting astronomical telescopes using Active Optics. It is necessary to position the segments or to deform the surface by force actuators to at least this precision. A 1/50 wavelength at 6328Å is approximately 0.5×10^{-6} inch. Therefore, the actuator must have controlled displacements of less than 0.5-microinch for wavelengths in the visible region of the spectrum. For ultraviolet applications, positioning accuracy would have to be better than 0.1 microinch to achieve ultraviolet diffraction-limited performance.

When the actuator is used as a precision force generator in the Perkin-Elmer Deformable Mirror applications, the displacement must be convertible to a precision force with a magnitude of ±2 pounds. This force level, in turn, corresponds to $\pm 1/2\lambda$ of displacement with a thin deformable mirror of fused quartz 1/2 inch thick, an f/D ratio of 3, and actuator spacing of

3 inches over a 30-inch diameter. While there are many physical principles that can be exploited to yield a precisely controlled force of the 2-pound level, there are other requirements (listed below) that further limit the choice. Specifically, the requirement for a power-off memory eliminates magnetic galvanometer coil approaches.

Power-off mechanical memory. -- The actuator should maintain the last controlled position (or force) when the power is turned off. This requirement corresponds to a mechanical memory. This feature will permit the telescope power to be turned off without having the mirror figure degenerate completely. Thus, when the optical system is reactivated, the control system will be able to proceed directly with fine alignment of the surface rather than starting with a completely misaligned surface.

Reversible displacements. -- Actuator devices that can produce a very small displacement in one direction frequently cannot produce this small displacement in the opposite direction. Furthermore, even when a device can make reversible displacements, very frequently that displacement occurs with excessive backlash or frontlash.

Since the actuator must be used in a servo loop configuration, it is desirable that the actuator be bilateral in nature; i.e., appropriately applied forces to the actuator cause the actuator armature to translate in either direction. Although servo systems have been built with locking type of actuators, such as locking worms, servo experience indicates that this type of a system is more difficult to stabilize because of the nonlinear nature of the servo load on the actuator. The very small displacement characteristic of the actuator as previously discussed is a potentially helpful requirement to minimize this bilateral requirement.

Large dynamic range. -- There are two ranges that must be considered. One range is that imposed by initial misalignment of the mirror segments or initial gross distortion of the deformable mirror due to the removal of 1-g forces. Since either of these adjustments needs be made only once per observation period, most of it could be done as a separate function. The other range is that due to thermal deformation and warping as well as to long-term material instability or creep.

Based on a typical supporting structure for a 120-inch mirror, the maximum displacement due to thermal cycling alone has been estimated to be 0.010 inch. The displacement would be correspondingly higher for larger structures.

It would be desirable, from the standpoint of minimizing moving parts and simplifying the control electronics, to be able to achieve a large dynamic range and precise positioning ability in the same actuator. However, this is by no means a rigid requirement. The functions of coarse and fine positioning might also be divided between two or more actuators operating in tandem.

Low power requirements. -- It is obvious that the average power drain must be maintained below the continuous power level available with enough surplus to operate other peripheral equipment and still allow for statistically possible malfunctions. Low power dissipation in the actuator is necessary to prevent thermal distortion of the mirror itself. Since the work to be done is extremely small, on the order of 1 microwatt equivalent per step, it is desirable to have a relatively efficient actuator to reduce the undesirable spurious effects that arise as a result of the additional dissipation. A zero-power requirement, during the time no displacements or forces are required, would be desirable and would allow the mirror to maintain its last corrected configuration during power-off operations of the space telescope.

The ability to operate in a space environment. -- Considerations of the problems of cold welding, evaporation, change of state, and change of properties and dimensions with temperature change and radiation bombardment must be made in the design of an actuator expected to operate reliably in space over a period of years. Hermetic seals, lubrication, and special temperature or pressure controls should be minimized or avoided.

Ability to work against an opposing force. -- The forces opposing actuator displacement in a space environment in the Segmented Active Optics case are small but not zero, and are due primarily to friction and inertia. For the Deformable Active Optics case, these forces are primarily due to mirror spring constant. Although the mirror segments might have a fairly large inertial mass, large forces are not necessarily required to displace them.

However, the smaller the force available and the shorter the time it is applied, the smaller the spring constant required between mirror and actuator will be, with a consequent degradation of the system response time.

Adequate response time. -- The required speed of response is estimated to be a rate of displacement of 3 microinches per second for a typical supporting structure for a 120-inch mirror. For larger mirrors the requirement would be correspondingly higher.

A displacement rate of 3 microinches per second may not seem to be a fast response. However, there are devices that Perkin-Elmer has rejected on the basis of this requirement.

Achievements

The first working piezoelectric peristaltic actuator has achieved a performance of bidirectional, sequential, controlled steps from 1/50 to 1/25 of a wavelength of visible light under varying load conditions of up to 1000 grams axially and transversely applied to the actuator. The actuator control zone is 2.0 inches and, with a step size of 1/50 wave (0.5 microinch), the dynamic control range is 4,000,000 to 1.

In addition, the piezoelectric peristaltic actuator has the following inherent characteristics:

(1) Ability to make very small steps against an opposing force.

(2) Reversible motion with no backlash.

(3) No power required for holding when not running.

(4) Low power consumption (essentially no power dissipated in actuator itself; only in the control electronics).

(5) Fast response time.

(6) High mechanical stability.

(7) Large dynamic range for motion and speed.

(8) Simple and rugged construction.

Construction Features

Three of the actuator assemblies built and tested are shown in Figures 1, 2, and 3. These figures and the frontispiece photograph show the basic simplicity of the device. The actuator is of two-piece construction consisting of an appropriately fitted solid Invar rod and a ceramic piezoelectric crystal. Essentially the device is a hollow ceramic crystal which under normal ambient conditions and no-voltage conditions is interference fitted onto the Invar shaft. If under this condition an attempt is made to move the Invar shaft with respect to the piezoelectric crystal, a restraining force appears. This force is a function of the amount of interference and the coefficient of friction. The interference fit produces the load holding capability under no-voltage conditions. An interference fit of between 50 to 100 micro-inches appears optimum. At any given section of the crystal, the interference fit can be reduced to zero with the application of a specific minimum voltage.

When the hollow crystal blank is purchased from the manufacturer, it has a silver coating fused to both the inside and the outside diameter. The inside is reworked during fabrication to the specified diameter and, in the process, the silver is removed. This removes the inside electrode for which the Invar shaft is substituted during operation. The outside silver, which is approximately 0.0007 inch, is not reduced in thickness. Grooves are subsequently ground on the outside to a depth sufficient to remove bands of the silver electrode with a minimum of crystal material removal. The resulting piezoelectric crystal now appears as a hollow cylinder with electrode rings on the outer

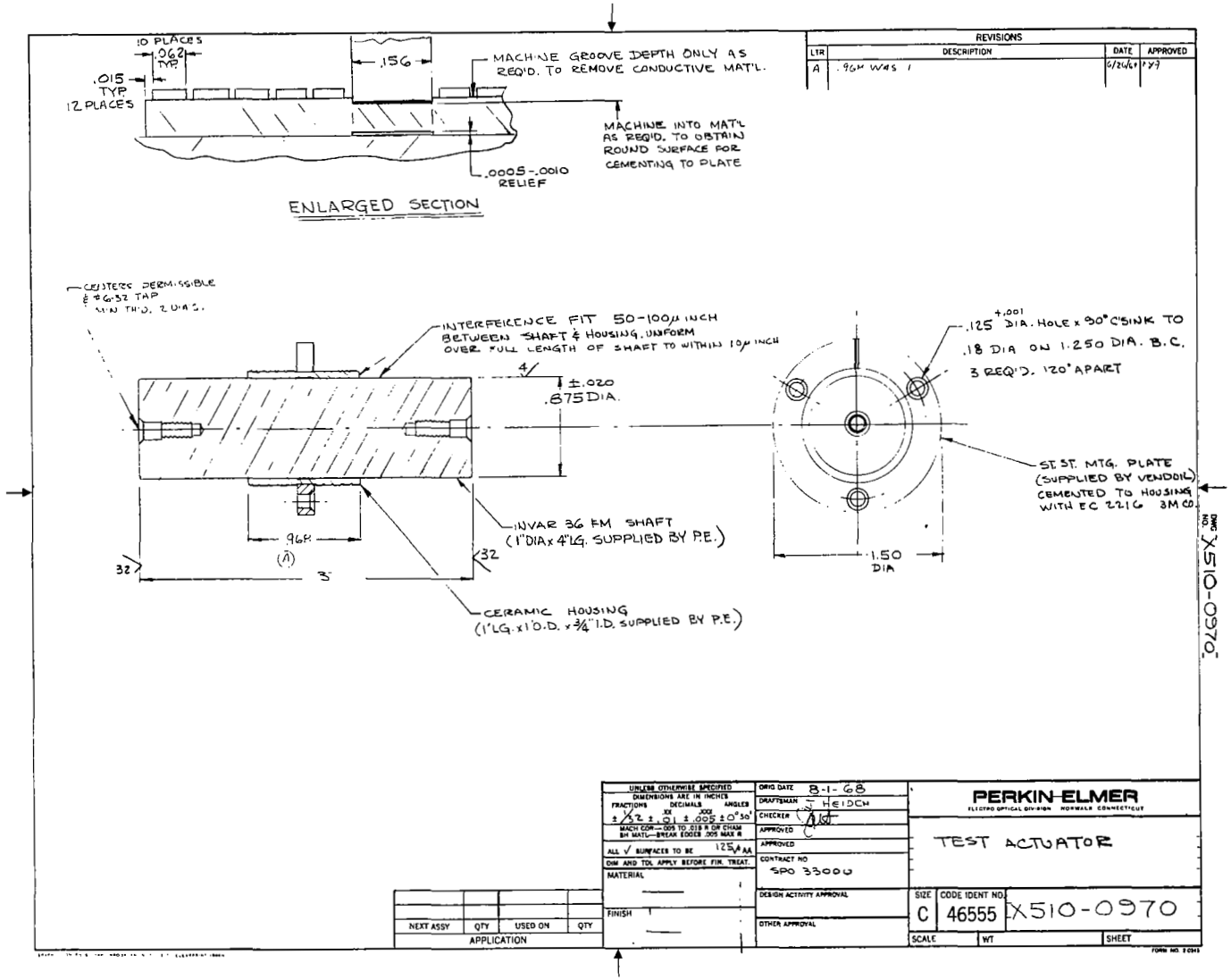

Figure 1. Test Actuator Assembly No. 1 (10 Electrodes)

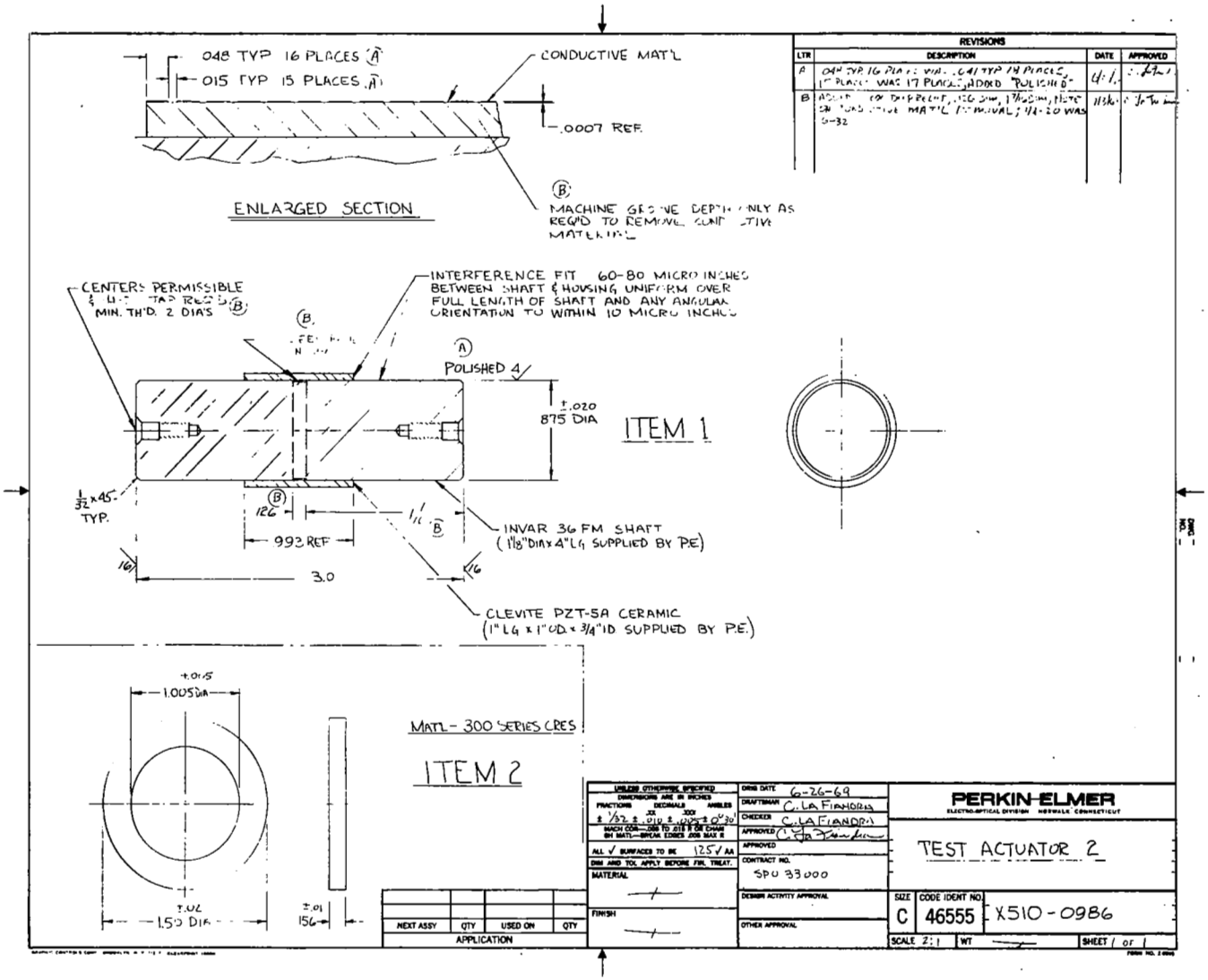

Figure 2. Test Actuator Assembly No. 2 (16 Electrodes)

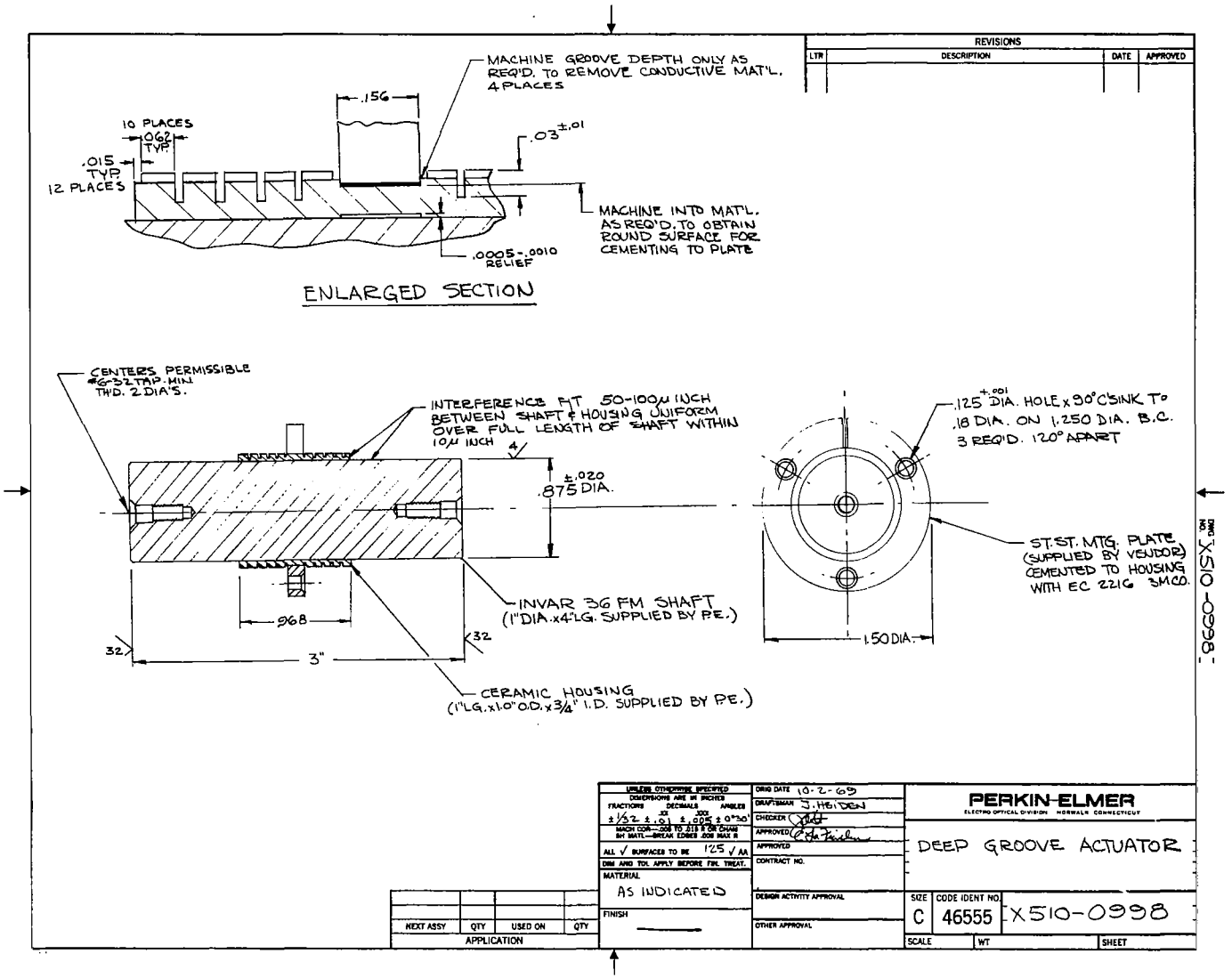

Figure 3. Deep Groove Actuator

circumference running the full length. In the first actuator fabricated and tested, the length in the center of the crystal had the electrodes removed to enable a mounting flange to be attached. The actuator design is flexible enough to permit this flange to be located anywhere along the length of the crystal. Test actuator No. 2 had no electrode material removed and the flange could be placed anywhere along its length. The inside of the piezoelectric crystals are honed to bring them to the desired diameter and finish. The outside diameters of the Invar shafts are lapped using pitch laps and optical polishing compound. The finish of the shaft is approximately 1-1/2 to 2 microinches. (Measurements taken were based on ASA B46.1 - 1962, Surface Texture and Surface Measurement Specification.)

The analysis of the characteristics of operation of the actuator shows that the location of the mounting flange is important since it determines the characteristic step shape of the actuator. The first actuators with the mounting flange in the middle produced the characteristic step shape depicting maximum displacement occurring during the middle of the step. The analysis showed that, if the flange were placed elsewhere on the crystal, the step shape would be appropriately modified. To prove this, it was first necessary to establish the fact that you do indeed obtain the same step characteristic by either mounting the actuator via the center located flange and monitoring the Invar shaft, or mounting the actuator on the Invar shaft and monitoring the flange. This interchangeability was proven with experimentation. That is, the same output step ensued from the actuator if the mounting and monitoring locations were interchanged. Once this was proven, an analysis-based prediction was made describing the step shape when the crystal end was monitored. The results of the experimentation with the actuator supported the prediction. This analysis and these results are described in the analytical section of this report.

Relative motion is made to occur between the Invar shaft and the ceramic piezoelectric crystal by appropriately pulsing the outer band electrodes on the crystal. The various actuators fabricated have either 10 electrodes or 16 electrodes with the same crystal length. The 10-electrode crystal has the mounting flange in the middle, while the 16-electrode crystal has no flange and a smaller width electrode. The gap between electrodes was maintained constant

at 0.015 inch in both instances. For the electrode spacing a tradeoff was made between the fixed length of crystal obtained, the maximum member of electrodes desired, the minimum gap between electrodes to prevent arc-over, the electrode length required to easily make contact, the voltage necessary to drive the crystal, and the depolarization voltage of the crystal. It is felt the PZT-5A purchased from the Clevite Corporation is satisfactory for the current configuration. Contact with the ring electrodes is accomplished in either of two ways. "Fingers", held by an insulator, press against the electrodes when the actuator is mounted by the center flange or wires are pigtailed on the electrodes using conductive epoxy adhesive when the actuator is run with the Invar shaft mounted. These techniques alleviate the problem of tieing the insulating block to the crystal. The actual details of the electrical pulsing technique used is described in this report in the electrical section.

Mounting Technique

In order to make any measurements of the operating characteristics of the actuators, it is necessary to mount the device in some prescribed manner. As the actuators were manufactured with a collar centrally located on the piezoelectric element expressly for mounting, this collar was the primary means of support. Collectively, there were three distinct methods used to mount and support the actuator.

The most widely used support technique was to forcibly clamp the collar at three roughly equally spaced locations around the collar. The collar was clamped against a half-inch thick steel plate off which also was mounted the adjustable mount for the Brown & Sharpe Electronic Indicator. The large portion of our measurements were taken in this configuration. This mounting technique is shown in Figure 4.

The second mounting technique used was to mount the device by clamping the collar at only one local area. Deliberate effort was made to assure that the rest of the collar and actuator was free to deflect. The technique is shown in Figure 5. This mounting configuration was of interest because it clearly indicated that the mounting flange was being substantially deformed during the step sequence. The data on this is presented in the section pertaining to data.

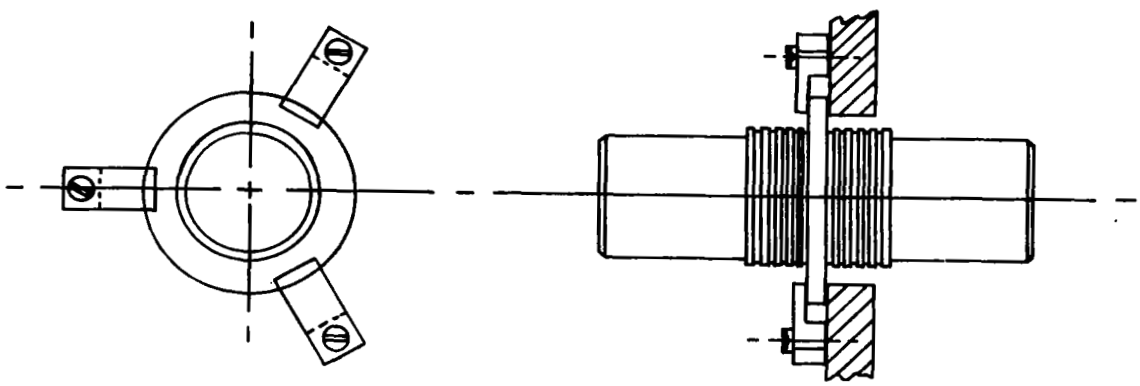

Figure 4. Actuator With Fully Clamped Collar

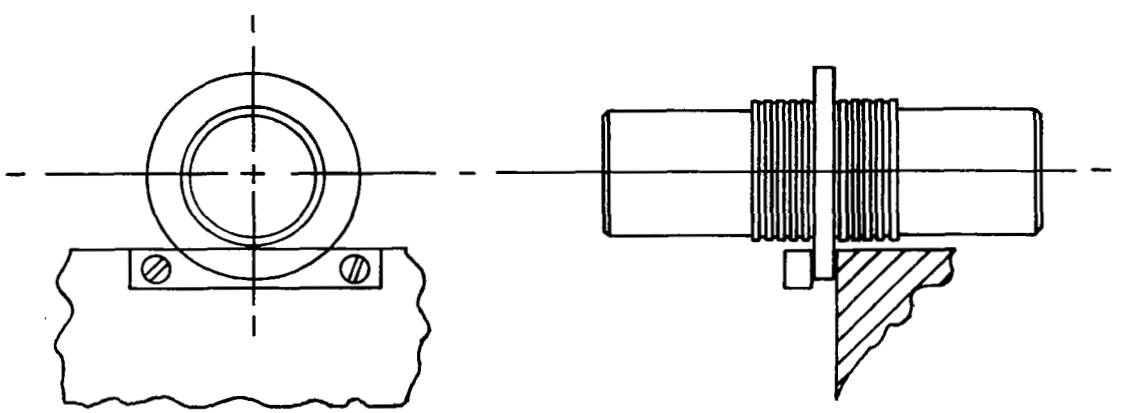

Figure 5. Actuator With Local Clamp

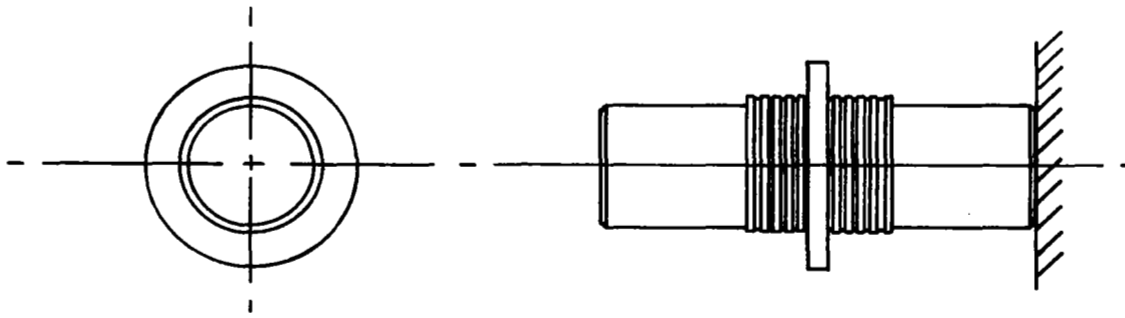

Figure 6. Actuator With Mounted Shaft

The third mounting technique was to mount the Invar shaft. This is shown in Figure 6. In this configuration, displacement measurements can be made at either end of the piezoelectric cylinder and at the mounting collar.

DESCRIPTION OF ELECTRONICS

The peristaltic actuator was designed to require the application of a relatively unique set of voltage waveforms. As these waveforms were not available from any existing electronic hardware, it was necessary to design and construct the necessary electronic system. This electronic system began with a set of manual switches and evolved into one with solid-state digital logic and high voltage amplifiers.

The manual switch system allowed any actuator electrode to be energized or de-energized at will. In this manner, initial observations of the actuator performance were obtained. Operating characteristics of this system that prompted further electronic development were:

(1) Lack of precise simultaniety of multiple switching operations

(2) Relatively slow switching sequence rate

(3) Tedium of producing repetitive stepping cycles

The second generation of the electronic system utilized solid-state electronic components. This system included both solid-state digital logic and high voltage amplifiers. With this system, investigations were performed to determine the optimum wave shape for the voltages applied to the piezoelectric electrodes. The various waveforms are shown in Figure 7.

Waveforms B and C are modifications of waveform A (Figure 7). They were achieved by passing the waveform A voltages through R-C low-pass filters with relatively long or short time constants before they were applied to the actuator electrodes.

Waveforms E and F are again modifications of waveform D. For waveform E, waveform D was used to switch on and off the high voltage that was modulated to produce a $1 + \cos \omega t$ waveform for the even numbered electrodes and a $1 - \cos \omega t$

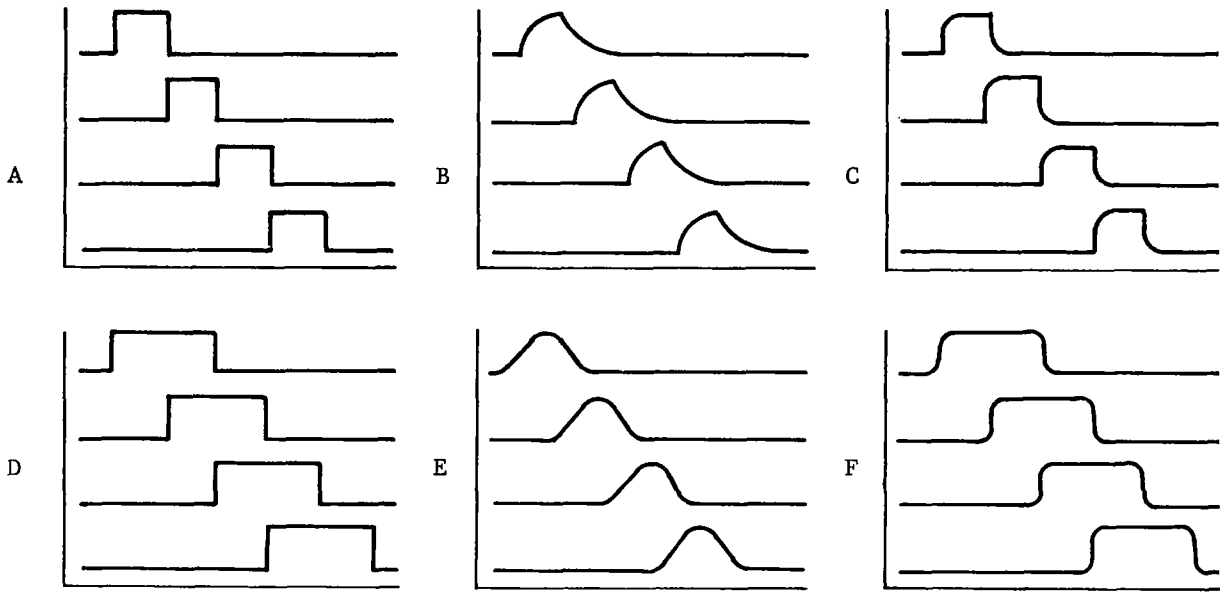

Figure 7. Waveforms of Voltages Applied to Piezoelectric Electrodes

waveform for the odd-numbered electrodes. Waveform F was obtained in the same manner as waveform E with the modification that the high voltage waveform was distorted away from the above description by feeding the signal through a non-linear circuit.

The only waveform that produced reliable stepping motion was observed to be the square wave potentials with each "on" cycle overlapping the previous and following sequential waveforms by one-half the "on" time of the square wave, waveform D. This is the waveform used for all subsequent testing and operation.

As a result of the successful performance tests performed with the above electronic system, additional features were built into the breadboard system. These provided incorporation of a built-in clock in place of an external signal generator; forward and reverse direction logic in place of rearranging output leads to change direction; a threshold and polarity detector to control actuator step direction, thereby allowing closed-loop operation. With this electronic system the bulk of the experimental data was obtained. The block diagram of this final breadboard electronic system is given in Figure 8.

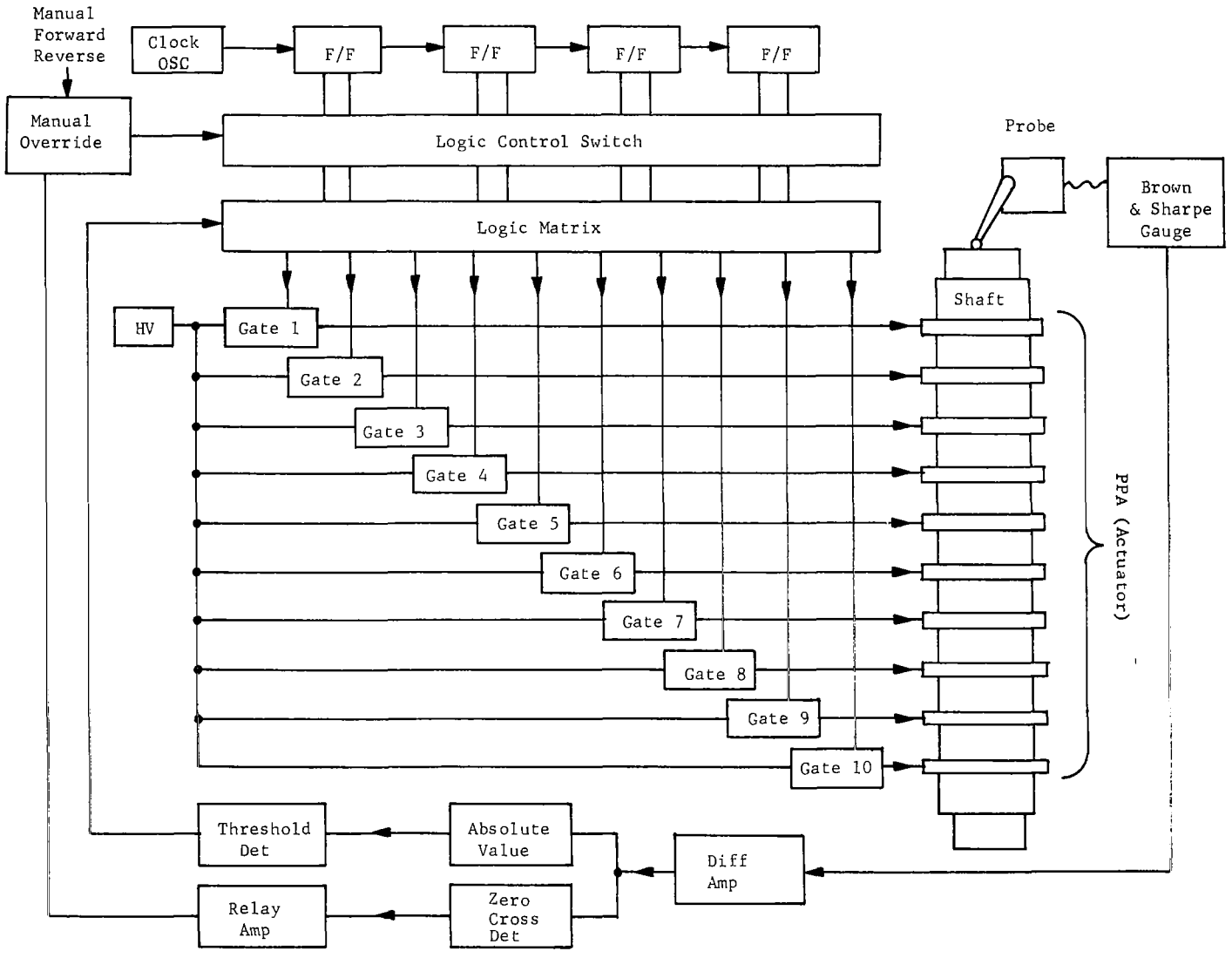

Figure 8. Block Schematic of Submillionth-of-an-Inch Servo System with Peristaltic Piezoelectric Actuator

With the introduction of the 16-electrode actuator, extensive modification to the electronics became necessary again. It was elected to build a complete new electronic system incorporating all the features that we felt were necessary and deleting those features that we deemed to be unnecessary. This system was designed to conform to the following characteristics:

(1) To be packaged in a deliverable form

(2) To be autonomous except for the high voltage power supply and displacement transducer.

(3) To provide manual control of step direction and rate

(4) To accommodate both 10-electrode and 16-electrode actuators.

For the control logic portion of this new electronic system, two competitive designs were developed. The first design was based upon integrated circuits, and included the above design characteristics plus the following characteristics:

(1) A given step always begins at the start of the counting sequence

(2) A step in process is completed before the actuator can stop or reverse direction.

The schematic diagram for this system is contained in Figure 9.

The second control logic designed was patterned after the system used in the breadboard electronics. This system is built up from discrete components and provides only the necessary functions listed above. It was decided to use this approach in the final package since we had already breadboarded this type of system and we were more familiar with the discrete component construction than with the integrated circuit construction.

The block diagram of the final electronic system is given in Figure 10. The complete schematic diagram will be supplied under separate cover to ERC.

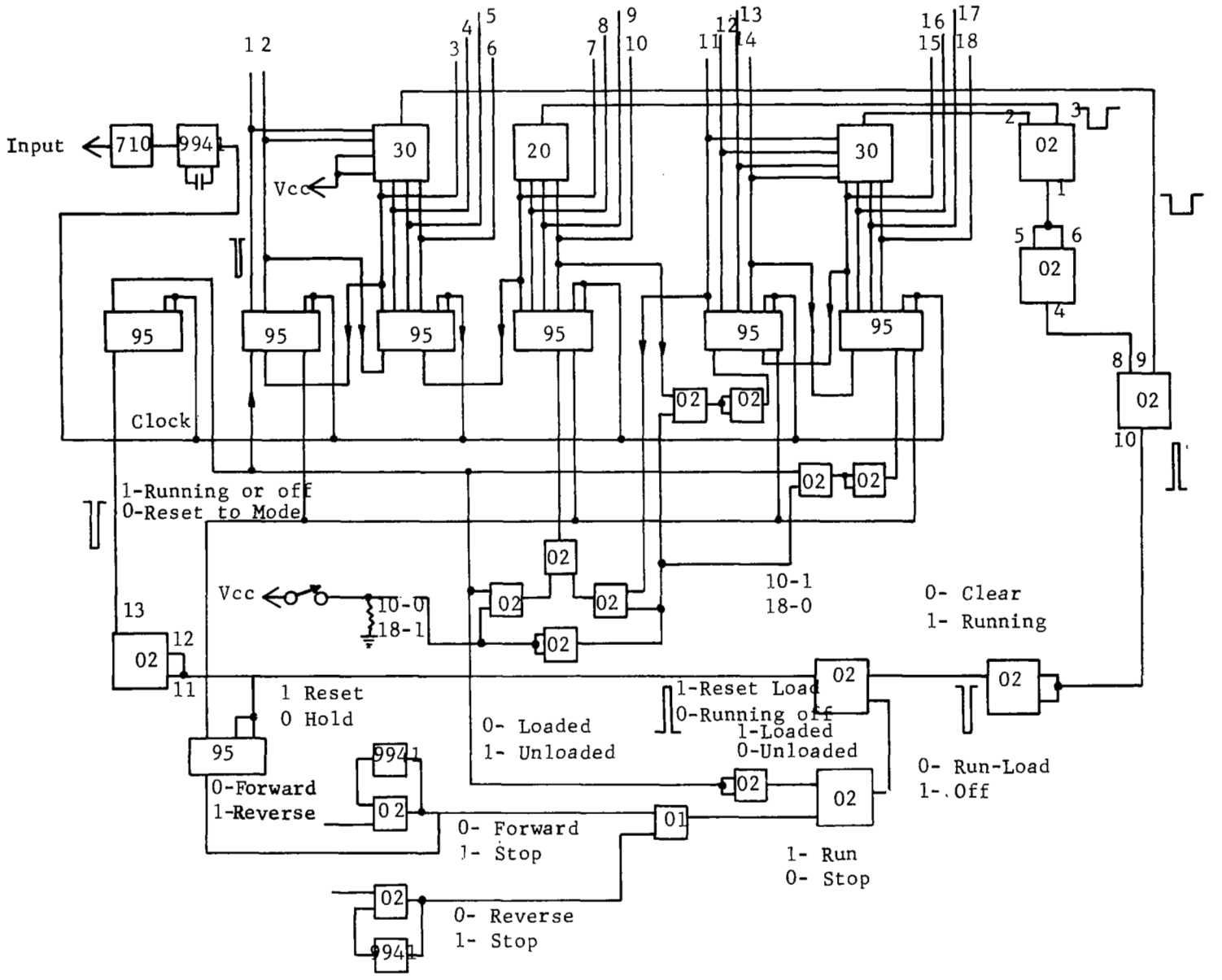

Figure 9. Integrated Circuit Control Logic

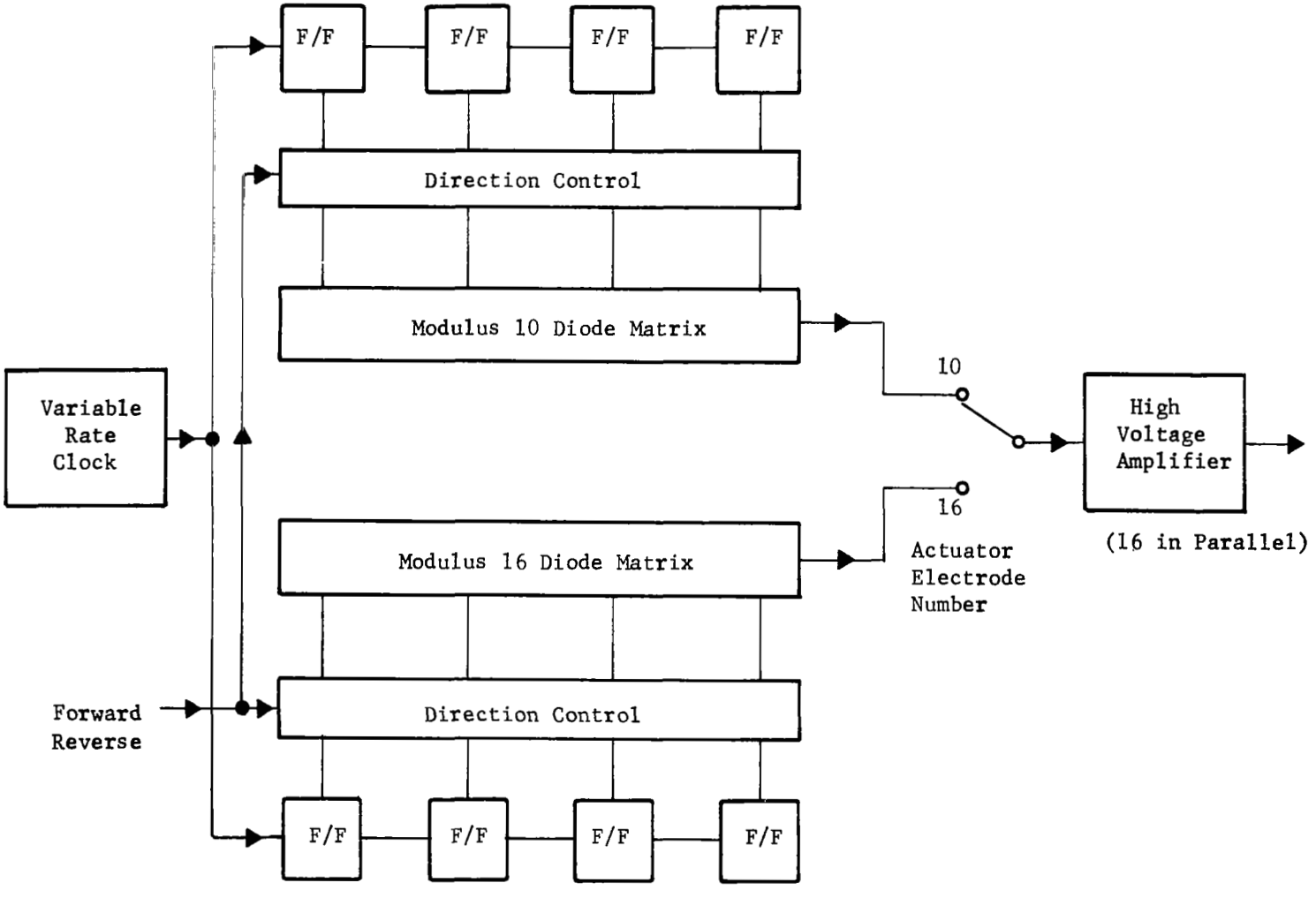

Figure 10. Block Diagram of Final Drive Electronics

Key features of the final electronic system are:

(1) Front Panel Controls:

(a) Single switch for selection of number of electrodes on actuator.

(b) Fast or slow rise time to reduce power supply loading when very fast step rates are not required.

(c) Toggle switch for Forward-off-Reverse control.

(d) Four-decade range switch for internal clock rate--variable from one step per second to one thousand steps per second.

(e) Fine control for internal clock--varies clock rate from coarse control setting to one-tenth of coarse control setting--allows a minimum speed of approximately one-tenth of one step per second.

(2) Rear Panel Connections:

(a) High voltage power supply connections.

(b) Bias supply connections--to provide ability to effectively increase or decrease the amount of the interference fit between the piezoelectric sleeve and the Invar shaft.

(3) Internal Features:

(a) Self-contained low-voltage power supplies.

(b) Built-in cooling fan to allow extended operation at the fast rise time setting for maximum step rates.

Appendix A of this report contains a brief operation manual for the electronics box.

ACTUATOR ANALYTICAL STUDY

The analytical work on the peristaltic actuator is divided into three parts. Part 1 concerns the calculation of surface displacements of the shaft caused by shrink-fitting a piezoelectric tube on the shaft, and of the shrink pressure between the tube and the shaft. Part 2 deals with a study of local separation between the tube and the shaft when the tube is electrically excited by applying voltage to any ring of silver coating on it. The axial displacement of the piezoelectric tube relative to the shaft caused by the application of voltage in presence of friction is considered in Part 3. It is this relative motion that is observed as the output displacement of the actuator either at an end of the shaft if the mounting plate is grounded, or at the mounting plate if the shaft is grounded. A number of simplifying assumptions have been made and only a linear static analysis has been attempted. Nonetheless, the correlation between the analysis and the experiment is good. The mathematical notations are separately defined for each of the three parts and should not be interchanged. Any symbol used does not necessarily denote the same thing in the three parts.

Part 1, Deformation of Actuator Shaft Due to Shrink Fit

A piezoelectric tube is shrink-fitted on a solid cylindrical shaft of Invar. This causes deformations in both the shaft and the tube. In general, the shrink pressure is nonuniform, but will be taken as approximately uniform. Analytical solutions of the problem are available in Refs. 1 and 2. According to the author of Ref. 2, the computed results of the two solutions show close correspondence in all except minor details. The method of Ref. 1 is relatively simple for computational purpose and will, therefore, be used here.

The deformation of a shaft due to a finite band of uniform pressure on its surface may be obtained by the application of the solution of a different problem. This is the problem of deformation of the shaft surface due to another kind of pressure distribution, hereafter to be called the basic pressure loading as shown in Figure 11(a). The pressure distribution of Figure 11(b) is the same as that of Figure 11(a) except that the direction of pressure is reversed and the origin is shifted to the right through a distance b. Superposition of pressure distributions of Figures 11(a) and 11(b) yields the required pressure

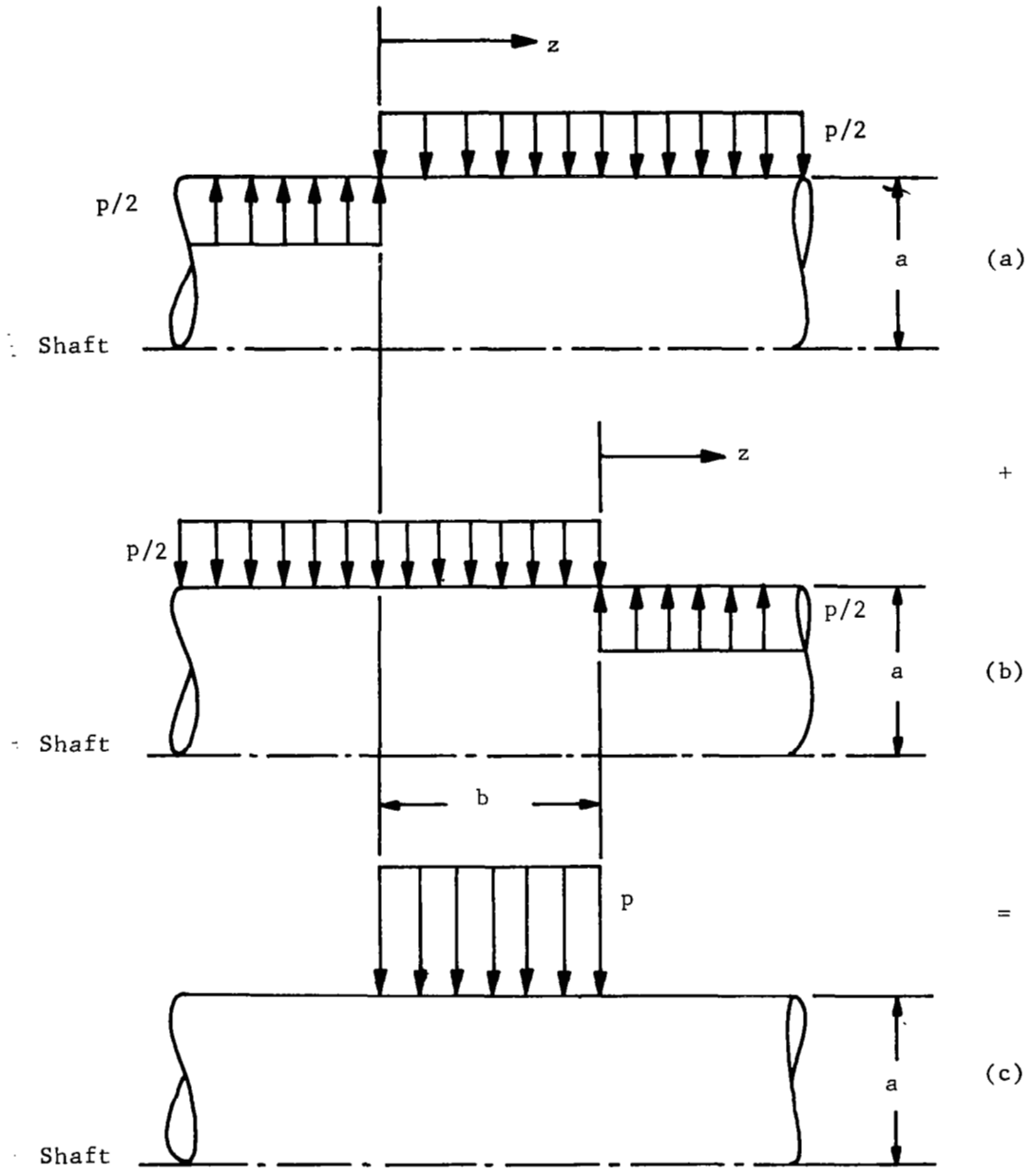

Figure 11. Shrink Pressure as a Superposition of Two Cases of Basic Pressure Loading

uniformly distributed over a width b as shown in Figure 11(c). The following equations, all taken from Ref. 1 except where otherwise stated, are for the case of the basic pressure loading of Figure 11(a). The notation used in these equations is as follows:

r = radial direction or coordinate

z = axial direction or coordinate

u = radial displacement

w = axial displacement

E = Young's modulus

ν = Poisson's ratio

a = radius of the cylinder

p = step pressure due to shrink fit as shown in Figure 11(c)

b = width of the pressure band = length of piezoelectric tube

$i = \sqrt{-1}$

J_n = Bessel function of the first kind and n^{th} order

I_n = modified Bessel function of the first kind and n^{th} order

The relationship between J_n and I_n is obtained for real t from p.128 of Ref. 3

$$J_n(2i\sqrt{t}) = i^n I_n(2\sqrt{t})$$

$$= (i\sqrt{t})^n \left[\frac{1}{n!} + \frac{t}{1!(n+1)!} + \frac{t^2}{2!(n+2)!} + \frac{t^3}{3!(n+3)!} + \cdots\cdots\right]$$

$$I_n(2\sqrt{t}) = t^{n/2}\left[\frac{1}{n!} + \frac{t}{1!(n+1)!} + \frac{t^2}{2!(n+2)!} + \frac{t^3}{3!(n+3)!} + \cdots\cdots\right] \quad (1\text{-}1)$$

$$I_o(2\sqrt{t}) = \left[\frac{1}{0!} + \frac{t}{1!1!} + \frac{t^2}{2!2!} + \frac{t^3}{3!3!} + \cdots\cdots\right]$$

$$= \sum_{n=1}^{\infty} \frac{t^{n-1}}{[(n-1)!]^2} \quad (1\text{-}2)$$

$$I_1(2\sqrt{t}) = \left[\frac{1}{1!} + \frac{t}{1!2!} + \frac{t^2}{2!3!} + \frac{t^3}{3!4!} + \ldots\right]\sqrt{t}$$

$$= \sqrt{t}\sum_{n=1}^{\infty} \frac{t^{n-1}}{(n-1)!n!} \tag{1-3}$$

Again from Ref. 1,

$$u_o = -\frac{pa(1-\nu)}{2E} \tag{1-4}$$

$$k = \frac{(2j-1)\pi}{4a} \tag{1-5}$$

$$m = -2(1-\nu) - k^2a^2\left[1 - \left\{\frac{I_o(ka)}{I_1(ka)}\right\}^2\right] \tag{1-6}$$

At the surface of the cylinder,

$$u_a = u_o \frac{8(1+\nu)}{\pi} \sum_{j=1}^{\infty} \frac{1}{(2j-1)m} \sin kz \tag{1-7}$$

$$w_a = -u_o \frac{4(1+\nu)}{\pi(1-\nu)} \sum_{j=1}^{\infty} \frac{1}{(2j-1)m} \left\{ka + \left[2(1-\nu) - ka\frac{I_o(ka)}{I_1(ka)}\right] \frac{I_o(ka)}{I_1(ka)}\right\} \cos kz \tag{1-8}$$

I_o (ka) and I_1 (ka) can be calculated from Eqs. (1-2) and (1-3) by substituting

$$t = \frac{k^2a^2}{4} \tag{1-9}$$

Computer program to calculate u_a and w_a.--

Input: p, a, ν, Δz, E

Calculate:

$$u_o = - pa\,(1-\nu)/2E$$

$$u_{ou} = u_o \times 8(1+\nu)/\pi;\quad u_{ow} = - u_o \times 4(1+\nu)/[\pi(1-\nu)]$$

$$m_o = -2(1-\nu);\quad z = 0$$

Repeat for $j' = 1, 2, \ldots\ldots \infty$:

$$j = 2j' - 1$$

$$k_j = \pi j/4a;\quad t_o = k_j^{\,2}\, a^2/4$$

$$I_o = 1;\quad I_1 = 1;\quad t = 1$$

Repeat for $n = 1, 2, \ldots\ldots \infty$:

$$t \leftarrow t_o t/(n-1)^2$$

$$I_o \leftarrow I_o + t$$

$$I_1 \leftarrow I_1 + t/n$$

$$I_1 \leftarrow \sqrt{t_o}\, I_1$$

$$R_j = I_o/I_1$$

$$m_j = m_o - k_j^{\,2}\, a^2(1 - I_o^{\,2}/I_1^{\,2})$$

$$\Sigma_1 = \Sigma_2 = \Sigma_3 = 0$$

Repeat for $j' = 1, 2, \ldots\ldots \infty$:

$$j = 2j' - 1$$

$$\Sigma_1 \leftarrow \Sigma_1 + (\sin k_j z)/m_j j$$

$$\Sigma_2 \leftarrow \Sigma_2 + 1/jm_j$$

$$\Sigma_3 \leftarrow \Sigma_3 + \left[k_j a + \left\{2(1-\nu) - k_j a\, R_j\right\} R_j\right] \cos k_j z$$

$$u_a = u_{ou} \times \Sigma_1$$

$$w_a = u_{ow}\,(\Sigma_2 + \Sigma_3)$$

$$z \leftarrow z + \Delta z$$

Repeat for as many Δz as required

In practice, the above repeated calculations are to be terminated for some finite values of n and j'.

Numerical Calculations. -- u_a and w_a are obtained from a computer program based on the foregoing outline. The following data are used:

$$a = 0.4375 \text{ in}, \quad \nu = 0.26, \quad E = 21 \times 10^6 \text{ psi},$$

$$dz = 0.05 \text{ in}, \quad p = p_o = 65 \text{ psi},$$

where p_o = shrink-fit pressure, assumed uniform, calculated as follows:

By Eq.(3) of Ref. 2,

u_{r_1} = radial displacement of the inside of the piezoelectric cylinder

$$= \frac{a p_o}{E_1} \left[\frac{(1+\nu_1) + (1-\nu_1)\, a^2/a_1^2}{1 - a^2/a_1^2} \right], \tag{1-10}$$

where a_1 = outer radius of the cylinder, a = inner radius of the cylinder, E_1 = Young's modulus of the piezoelectric material, ν_1 = Poisson's ratio for the piezoelectric material. With $a_1 = 0.5005$ in., $a = 0.4375$ in., $E_1 = 9.14 \times 10^6$ psi and $\nu_1 = 0.31$, we have

$$u_{r_1} = \frac{0.4375 \times p_o}{9.14 \times 10^6} \left[\frac{(1+0.31)+(1-0.31) \times 0.4375^2/0.5005^2}{1 - 0.4375^2/0.5005^2} \right]$$

$$= 0.3728 \times 10^{-6}\ p_o \text{ in.}$$

By Eq.(4) of Ref. 2,

u_{r_2} = radial displacement of the outer surface of the shaft

$$= \frac{(1-\nu) a\ p_o}{kE}, \tag{1-11}$$

where k is to be obtained from Figure 2 of Ref. 2 for the given value of b/2a. With b = 1.0 in., a = 0.4375 in., b/2a = 1/ 2 x 0.4375 = 1.143. The corresponding value of k is approximately 1.25.

$$u_{r_2} = \frac{(1-0.26) \times 0.4375\ p_o}{1.25 \times 21 \times 10^6} = 0.0123 \times 10^{-6}\ p_o \text{ in.}$$

Now for compatibility of displacements we must have

$$u_{r_1} + u_{r_2} = \delta_r = \text{specified radial shrink;}$$

therefore,

$$(0.3728 + 0.0123) \times 10^{-6}\ p_o = 25 \times 10^{-6} \text{ in.}$$

Therefore, $p_o \simeq 65$ psi.

The computer calculations are given in Table I and are plotted in Figure 12.

The surface displacements of Table I and Figure 12 are for the basic pressure loading of Figure 11(a). The displacements due to a pressure band of width b = 1 in. can be obtained as previously explained and as shown in Figure 11. Figure 13 gives plots of radial and axial surface displacements due to this pressure band.

If the central relief is taken into consideration, the shrink fit pressure may be approximated by two uniform pressure bands as shown below. The surface

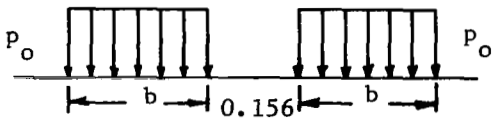

displacements for each band may be calculated exactly as above and superposed to obtain the resultant distribution. However, p_o may have to be recalculated because b = 0.422 in. is different now. b/2 a = 0.422/(2 x 0.4375) = 0.4822. For this value of b/2a, k ≃ 1.3 from Figure 2 of Ref. 2. This is not much

TABLE I
COMPUTER PRINTOUT OF SURFACE DISPLACEMENTS

Z	u_a	w_a	Z	u_a	w_a
.000	.0000E 00	-.3726E-06	.000	.0000E 00	-.3726E-06
.050	-.2492E-06	-.4029E-06	-.050	.2492E-06	-.4029E-06
.100	-.3540E-06	-.4256E-06	-.100	.3540E-06	-.4256E-06
.150	-.4251E-06	-.4373E-06	-.150	.4251E-06	-.4373E-06
.200	-.4653E-06	-.4354E-06	-.200	.4653E-06	-.4354E-06
.250	-.4887E-06	-.4265E-06	-.250	.4887E-06	-.4265E-06
.300	-.5044E-06	-.4086E-06	-.300	.5044E-06	-.4086E-06
.350	-.5093E-06	-.3856E-06	-.350	.5093E-06	-.3856E-06
.400	-.5142E-06	-.3578E-06	-.400	.5142E-06	-.3578E-06
.450	-.5132E-06	-.3260E-06	-.450	.5132E-06	-.3260E-06
.500	-.5132E-06	-.2923E-06	-.500	.5132E-06	-.2923E-06
.550	-.5116E-06	-.2556E-06	-.550	.5116E-06	-.2556E-06
.600	-.5094E-06	-.2184E-06	-.600	.5094E-06	-.2184E-06
.650	-.5088E-06	-.1795E-06	-.650	.5088E-06	-.1795E-06
.700	-.5062E-06	-.1403E-06	-.700	.5062E-06	-.1403E-06
.750	-.5064E-06	-.1006E-06	-.750	.5064E-06	-.1006E-06
.800	-.5047E-06	-.6025E-07	-.800	.5047E-06	-.6025E-07
.850	-.5049E-06	-.2036E-07	-.850	.5049E-06	-.2036E-07
.900	-.5049E-06	.2036E-07	-.900	.5049E-06	.2036E-07
.950	-.5047E-06	.6025E-07	-.950	.5047E-06	.6025E-07
1.000	-.5064E-06	.1006E-06	-1.000	.5064E-06	.1006E-06
1.050	-.5062E-06	.1403E-06	-1.050	.5062E-06	.1403E-06
1.100	-.5088E-06	.1795E-06	-1.100	.5088E-06	.1795E-06
1.150	-.5094E-06	.2184E-06	-1.150	.5094E-06	.2184E-06
1.200	-.5116E-06	.2556E-06	-1.200	.5116E-06	.2556E-06
1.250	-.5132E-06	.2923E-06	-1.250	.5132E-06	.2923E-06
1.300	-.5132E-06	.3260E-06	-1.300	.5132E-06	.3260E-06
1.350	-.5142E-06	.3578E-06	-1.350	.5142E-06	.3578E-06
1.400	-.5093E-06	.3856E-06	-1.400	.5093E-06	.3856E-06
1.450	-.5044E-06	.4086E-06	-1.450	.5044E-06	.4086E-06
1.500	-.4887E-06	.4265E-06	-1.500	.4887E-06	.4265E-06

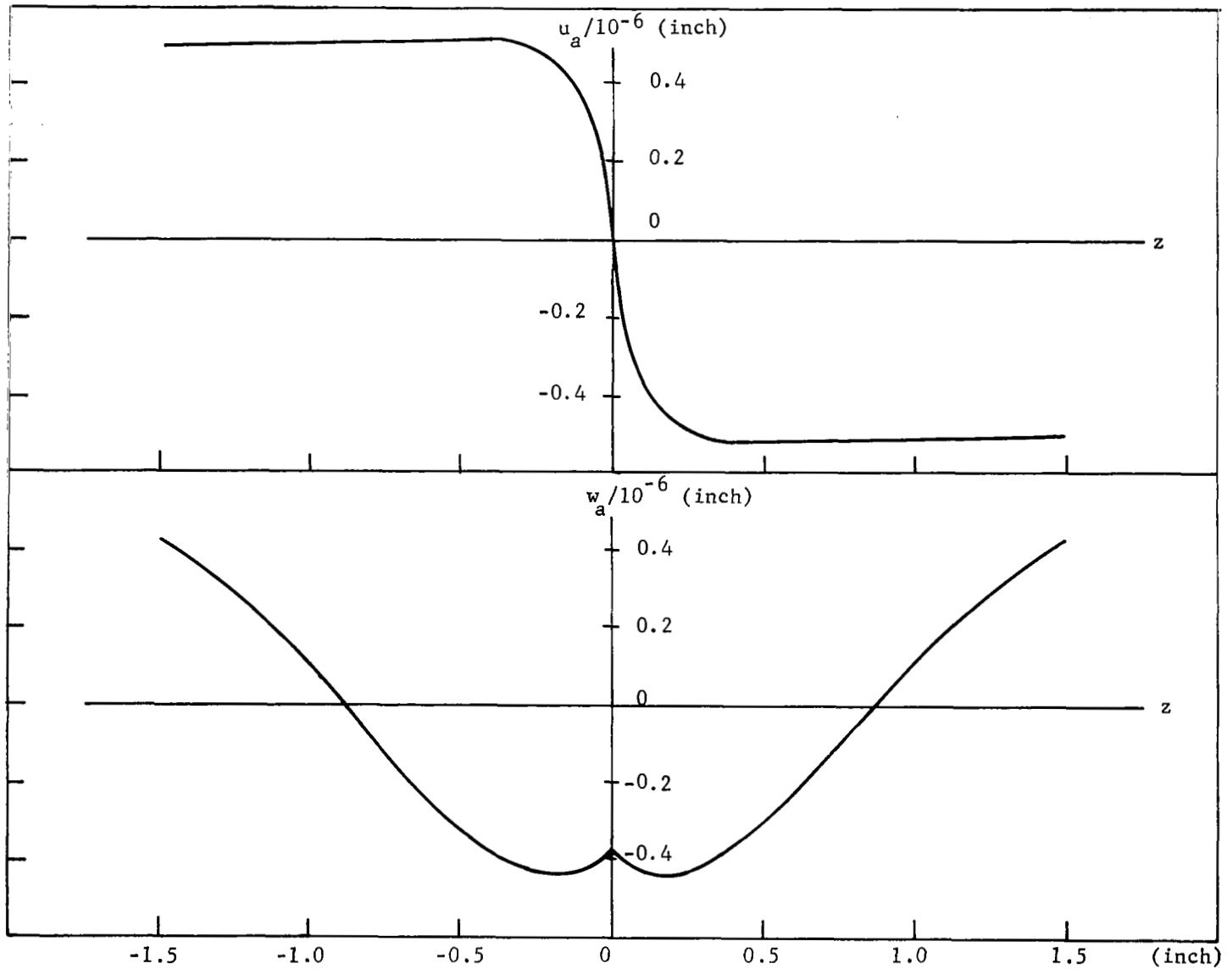

Figure 12. Surface Displacements Due to Basic Pressure Loading

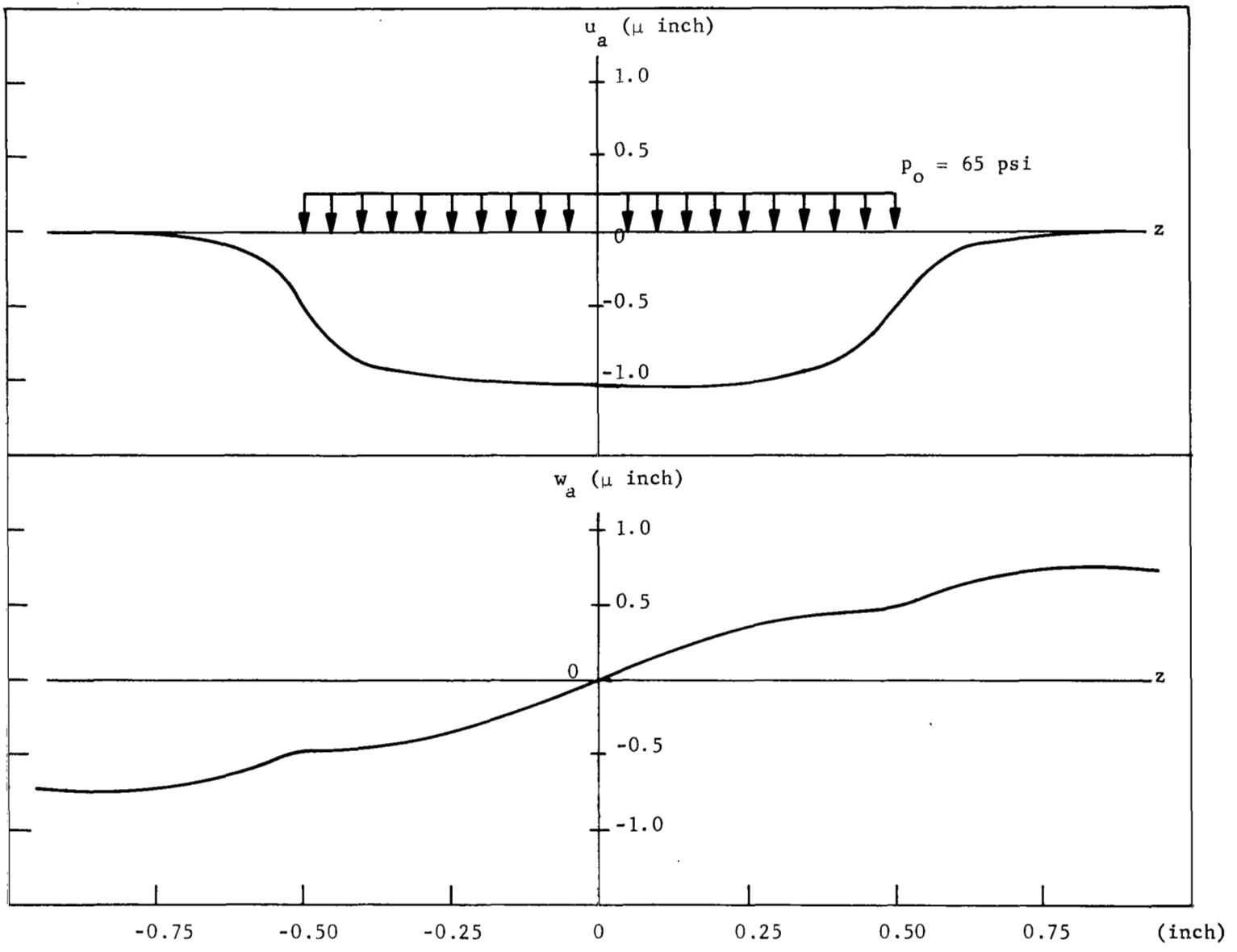

Figure 13. Surface Displacements of Shaft Due to Shrink Fit Without Central Relief

different from k as previously used. Therefore, p_o will not change significantly. The surface displacement plots for this case are given in Figure 14.

Conclusion. -- As shown in Figure 14, the maximum radially inward displacement of the outer surface of the shaft is approximately 1 microinch. The radially outward displacement of the inner surface of the piezoelectric tube must then be approximately 24 microinches so as to make up a total of 25 microinches of radial interference between the tube and the shaft. Consequently, the shaft may be assumed to be rigid in comparison with the tube.

Part 2, Local Separation Between Shaft and Piezoelectric Tube Due to Application of Voltage

The piezoelectric tube is a thin walled shell of anisotropic material whose dimensions are changed when it is subjected to an electric voltage. Its mean radius and length are increased and the wall thickness is reduced. This causes a reduction in the shrink pressure between the shell and the shaft. If the voltage is applied over the entire surface of the shell, the pressure reduction takes place all over its inner surface. If the voltage is restricted to one or more conducting rings of silver coating on the shell, the reduction in pressure is confined to the inner surface in the regions of the rings. The voltage on any ring required to null the shrink pressure may be denoted by V_o. Any increase in voltage over V_o causes the ring surface to lift and separate from the shaft locally. This separation, which is due to the radial piezoelectric growth of a ring, will be considered in this section. The axial displacement of the shell is ignored here, but will be considered later in Part 3.

Equations of elastic thin shell theory from Ref. 4 will be used here. The anisotropic nature of the piezoelectric material is ignored and the shell is assumed to be isotropic. Figure 15 shows the geometry and the loading of the shell. The pressure over the width (a-b) of a ring is assumed to be uniform and its direction is opposite to that of the shrink pressure,which is not shown in the figure. The notation used in the analysis is as follows:

R = mean radius of the shell (in.)

t = wall thickness of the shell (in.)

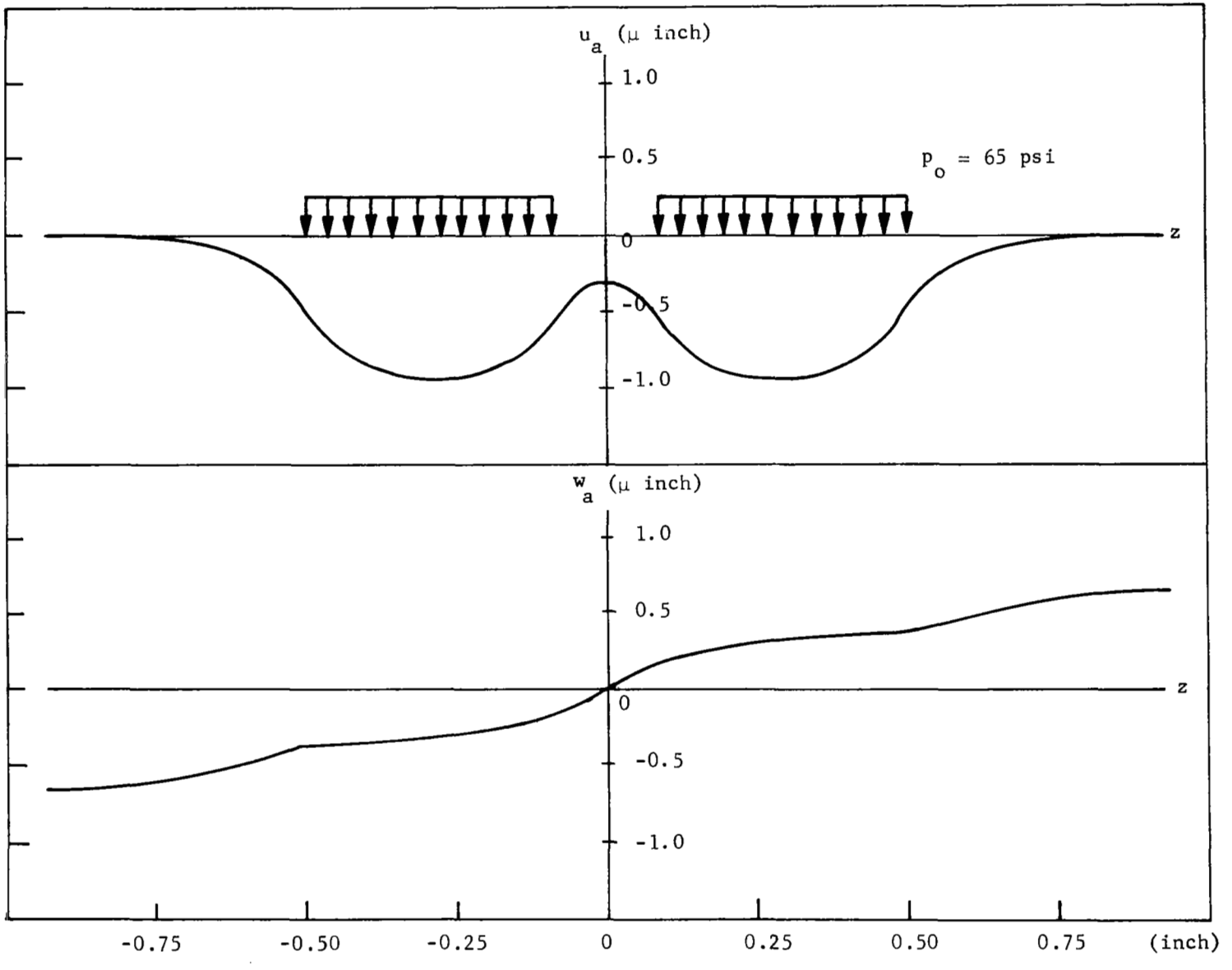

Figure 14. Surface Displacements of Shaft Due to Shrink Fit With Central Relief

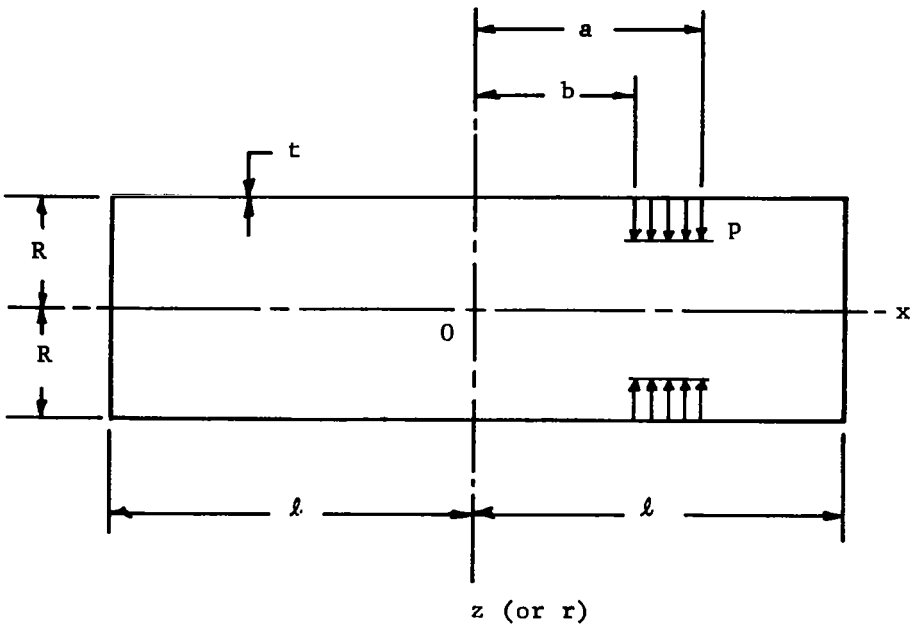

Figure 15. Geometry of Piezoelectric Tube Treated as a Thin Shell

2ℓ = length of the shell (in.)

p = intensity of band pressure (psi)

a = distance of the right edge of the pressure band from the middle cross section of the shell (in.)

b = distance of the left edge of the pressure band from the middle cross section of the shell (in.)

w = w(x) = radial displacement (in.)

E = Young's modulus of elasticity (psi)

ν = Poisson's ratio

D_o = flexural rigidity = $Et^3/12(1-\nu^2)$ (lb in.)

Z = Z(x) = applied radial load (psi)

From Ref. 4, the differential equation governing the radial displacement of the shell is

$$\frac{d^4w}{dx^4} + 4\beta^4 w = \frac{Z}{D_o} \tag{2-1}$$

where

$$\beta^4 = \frac{Et}{4R^2D_o} = \frac{3(1-\nu^2)}{R^2t^2} \tag{2-2}$$

General solution of Eq. (2-1) is

$$w = e^{\beta x}(C_1 \cos \beta x + C_2 \sin \beta x) + e^{-\beta x}(C_3 \cos \beta x + C_4 \sin \beta x) + F(x), \tag{2-3}$$

where F(x) is a particular solution of Eq. (2-1). For the three branches of the deflection curve, represented by i = 1, 2, and 3, respectively, the external radial load and the particular solutions are

$$\left.\begin{aligned} &i = 1,\ -\ell \le x \le b,\ Z = 0,\ F(x) = 0 \\ &i = 2,\ b \le x \le a,\ Z = p,\ F(x) = \frac{pR^2}{Et} \\ &i = 3,\ a \le x \le \ell,\ Z = 0,\ F(x) = 0 \end{aligned}\right\} \tag{2-4}$$

The general solution for the three branches of the deflection curve may then be written as

$$w_i = e^{\beta x}(C_{1i} \cos \beta x + C_{2i} \sin \beta x) + e^{-\beta x}(C_{3i} \cos \beta x + C_{4i} \sin \beta x) + n \frac{pR^2}{Et} \tag{2-5}$$

where $n = 0$ for $i = 1$ and 3, and $n = 1$ for $i = 2$.

Three successive differentiations of Eq. (2-5) with respect to x give the following:

$$\frac{dw_i}{dx} = \beta e^{\beta x}\left[(C_{1i} + C_{2i}) \cos \beta x + (C_{2i} - C_{1i}) \sin \beta x\right] - \beta e^{-\beta x}\left[(C_{3i} - C_{4i}) \cos \beta x + (C_{3i} + C_{4i}) \sin \beta x\right] \tag{2-6}$$

$$\frac{d^2w_i}{dx^2} = 2\beta^2 e^{\beta x}(C_{2i} \cos \beta x - C_{1i} \sin \beta x) - 2\beta^2 e^{-\beta x}(C_{4i} \cos \beta x - C_{3i} \sin \beta x) \tag{2-7}$$

$$\frac{d^3w_i}{dx^3} = 2\beta^3 e^{\beta x}\left[(C_{2i} - C_{1i}) \cos \beta x - (C_{1i} + C_{2i}) \sin \beta x\right] + 2\beta^3 e^{-\beta x}\left[(C_{3i} + C_{4i}) \cos \beta x + (C_{4i} - C_{3i}) \sin \beta x\right] \tag{2-8}$$

The 12 constants C_{ji}, $j = 1, 2, 3, 4$, $i = 1, 2, 3$ in Eq. (2-5) can be evaluated by applying the boundary conditions and conditions of continuity.

Bending moment M_x and shear force Q_x are zero at both ends, which are free.

(1) $\frac{d^2w_1}{dx^2} = 0$ at $x = -\ell$

(2) $\frac{d^2w_3}{dx^2} = 0$ at $x = \ell$

(3) $\frac{d^3w_1}{dx^3} = 0 \quad \text{at } x = -\ell$

(4) $\frac{d^3w_3}{dx^3} = 0 \quad \text{at } x = \ell$

Deflections of branches 1 and 2 are equal at x = b, and those of branches 2 and 3 are equal at x = a.

(5) $w_1 = w_2 \quad \text{at } x = b$

(6) $w_2 = w_3 \quad \text{at } x = a$

Slopes of branches 1 and 2 are equal at x = b, and those of branches 2 and 3 are equal at x = a.

(7) $\frac{dw_1}{dx} = \frac{dw_2}{dx} \quad \text{at } x = b$

(8) $\frac{dw_2}{dx} = \frac{dw_3}{dx} \quad \text{at } x = a$

Bending moments for branches 1 and 2 are equal at x = b, and those for branches 2 and 3 are equal at x = a.

(9) $\frac{d^2w_1}{dx^2} = \frac{d^2w_2}{dx^2} \quad \text{at } x = b$

(10) $\frac{d^2w_2}{dx^2} = \frac{d^2w_3}{dx^2} \quad \text{at } x = a$

Shear forces for branches 1 and 2 are equal at x = b, and those for branches 2 and 3 are equal at x = a.

(11) $\frac{d^3w_1}{dx^3} = \frac{d^3w_2}{dx^3} \quad \text{at } x = b$

(12) $\frac{d^3w_2}{dx^3} = \frac{d^3w_3}{dx^3} \quad \text{at } x = a.$

Substitution of these 12 conditions in Eqs. (2-5) through (2-8) yields the following 12 equations.

$$e^{-\beta\ell}(C_{21}\cos\beta\ell + C_{11}\sin\beta\ell) - e^{\beta\ell}(C_{41}\cos\beta\ell + C_{31}\sin\beta\ell) = 0 \tag{2-9}$$

$$e^{\beta\ell}(C_{23}\cos\beta\ell - C_{13}\sin\beta\ell) - e^{-\beta\ell}(C_{43}\cos\beta\ell - C_{33}\sin\beta\ell) = 0 \tag{2-10}$$

$$e^{-\beta\ell}\left[(C_{21} - C_{11})\cos\beta\ell + (C_{11} + C_{21})\sin\beta\ell\right] + e^{\beta\ell}\left[(C_{31} + C_{41})\cos\beta\ell + (C_{31} - C_{41})\sin\beta\ell\right] = 0 \tag{2-11}$$

$$e^{\beta\ell}\left[(C_{23} - C_{13})\cos\beta\ell - (C_{13} + C_{23})\sin\beta\ell\right] + e^{-\beta\ell}\left[(C_{33} + C_{43})\cos\beta\ell + (C_{43} - C_{33})\sin\beta\ell\right] = 0 \tag{2-12}$$

$$e^{\beta b}(C_{11}\cos\beta b + C_{21}\sin\beta b) + e^{-\beta b}(C_{31}\cos\beta b + C_{41}\sin\beta b) = e^{\beta b}(C_{12}\cos\beta b + C_{22}\sin\beta b) + e^{-\beta b}(C_{32}\cos\beta b + C_{42}\sin\beta b) + pR^2/Et \tag{2-13}$$

$$e^{\beta a}(C_{12}\cos\beta a + C_{22}\sin\beta a) + e^{-\beta a}(C_{32}\cos\beta a + C_{42}\sin\beta a) = e^{\beta a}(C_{13}\cos\beta a + C_{23}\sin\beta a) + e^{-\beta a}(C_{33}\cos\beta a + C_{43}\sin\beta a) - pR^2/Et \tag{2-14}$$

$$e^{\beta b}\left[(C_{11}+C_{21})\cos\beta b+(C_{21}-C_{11})\sin\beta b\right]$$
$$-e^{-\beta b}\left[(C_{31}-C_{41})\cos\beta b+(C_{31}+C_{41})\sin\beta b\right]$$
$$=e^{\beta b}\left[(C_{12}+C_{22})\cos\beta b+(C_{22}-C_{12})\sin\beta b\right] \tag{2-15}$$
$$-e^{-\beta b}\left[(C_{32}-C_{42})\cos\beta b+(C_{32}+C_{42})\sin\beta b\right]$$

$$e^{\beta a}\left[(C_{12}+C_{22})\cos\beta a+(C_{22}-C_{12})\sin\beta a\right]$$
$$-e^{-\beta a}\left[(C_{32}-C_{42})\cos\beta a+(C_{32}+C_{42})\sin\beta a\right] \tag{2-16}$$
$$=e^{\beta a}\left[(C_{13}+C_{23})\cos\beta a+(C_{23}-C_{13})\sin\beta a\right]$$
$$-e^{-\beta a}\left[(C_{33}-C_{43})\cos\beta a+(C_{33}+C_{43})\sin\beta a\right]$$

$$e^{\beta b}\left(C_{21}\cos\beta b-C_{11}\sin\beta b\right)-e^{-\beta b}\left(C_{41}\cos\beta b\right.$$
$$\left.-C_{31}\sin\beta b\right)=e^{\beta b}\left(C_{22}\cos\beta b-C_{12}\sin\beta b\right) \tag{2-17}$$
$$-e^{-\beta b}\left(C_{42}\cos\beta b-C_{32}\sin\beta b\right)$$

$$e^{\beta a}\left(C_{22}\cos\beta a-C_{12}\sin\beta a\right)-e^{-\beta a}\left(C_{42}\cos\beta a-C_{32}\sin\beta a\right) \tag{2-18}$$
$$=e^{\beta a}\left(C_{23}\cos\beta a-C_{13}\sin\beta a\right)-e^{-\beta a}\left(C_{43}\cos\beta a-C_{33}\sin\beta a\right)$$

$$e^{\beta b}\left[(C_{21}-C_{11})\cos\beta b-(C_{11}+C_{21})\sin\beta b\right]$$
$$+e^{-\beta b}\left[(C_{31}+C_{41})\cos\beta b+(C_{41}-C_{31})\sin\beta b\right]$$
$$=e^{\beta b}\left[(C_{22}-C_{12})\cos\beta b-(C_{12}+C_{22})\sin\beta b\right] \tag{2-19}$$
$$+e^{-\beta b}\left[(C_{32}+C_{42})\cos\beta b+(C_{42}-C_{32})\sin\beta b\right]$$

$$
\begin{aligned}
&e^{\beta a}\left[(C_{22} - C_{12})\cos\beta a - (C_{12} + C_{22})\sin\beta a\right] \\
&\quad + e^{-\beta a}\left[(C_{32} + C_{42})\cos\beta a + (C_{42} - C_{32})\sin\beta a\right] \\
&= e^{\beta a}\left[(C_{23} - C_{13})\cos\beta a - (C_{13} + C_{23})\sin\beta a\right] \\
&\quad + e^{-\beta a}\left[(C_{33} + C_{43})\cos\beta a + (C_{43} - C_{33})\sin\beta a\right]
\end{aligned}
\tag{2-20}
$$

Now, introduce the following functions:

$$
\left.
\begin{aligned}
f_1(x) &= e^{\beta x}\cos\beta x \\
f_2(x) &= e^{-\beta x}\cos\beta x \\
f_3(x) &= e^{\beta x}\sin\beta x \\
f_4(x) &= e^{-\beta x}\sin\beta x
\end{aligned}
\right\}
\tag{2-21}
$$

Further, for k = 1, 2, 3, and 4, let

$$
\left.
\begin{aligned}
\lambda_k &= f_k(\ell) \\
\mu_k &= f_k(b) \\
\alpha_k &= f_k(a)
\end{aligned}
\right\}
\tag{2-22}
$$

Equations (2-9) through (2-20) then reduce to the following equations:

$$\lambda_4 C_{11} + \lambda_2 C_{21} - \lambda_3 C_{31} - \lambda_1 C_{41} = 0 \tag{2-23}$$

$$-\lambda_3 C_{13} + \lambda_1 C_{23} + \lambda_4 C_{33} - \lambda_2 C_{43} = 0 \tag{2-24}$$

$$
\begin{aligned}
&(\lambda_4 - \lambda_2) C_{11} + (\lambda_4 + \lambda_2) C_{21} + (\lambda_1 + \lambda_3) C_{31} \\
&\quad + (\lambda_1 - \lambda_3) C_{41} = 0
\end{aligned}
\tag{2-25}
$$

$$
\begin{aligned}
&-(\lambda_1 + \lambda_3) C_{13} + (\lambda_1 - \lambda_3) C_{23} + (\lambda_2 - \lambda_4) C_{33} \\
&\quad + (\lambda_2 + \lambda_4) C_{43} = 0
\end{aligned}
\tag{2-26}
$$

$$
\begin{aligned}
&\mu_1 C_{11} + \mu_3 C_{21} + \mu_2 C_{31} + \mu_4 C_{41} - \mu_1 C_{12} - \mu_3 C_{22} \\
&\quad - \mu_2 C_{32} - \mu_4 C_{42} = pR^2/Et
\end{aligned}
\tag{2-27}
$$

$$\alpha_1 C_{12} + \alpha_3 C_{22} + \alpha_2 C_{32} + \alpha_4 C_{42} - \alpha_1 C_{13} - \alpha_3 C_{23} - \alpha_2 C_{33} - \alpha_4 C_{43} = - pR^2/Et \tag{2-28}$$

$$(\mu_1 - \mu_3) C_{11} + (\mu_1 + \mu_3) C_{21} - (\mu_2 + \mu_4) C_{31} + (\mu_2 - \mu_4) C_{41} - (\mu_1 - \mu_3) C_{12} - (\mu_1 + \mu_3) C_{22} + (\mu_2 + \mu_4) C_{32} - (\mu_2 - \mu_4) C_{42} = 0 \tag{2-29}$$

$$(\alpha_1 - \alpha_3) C_{12} + (\alpha_1 + \alpha_3) C_{22} - (\alpha_2 + \alpha_4) C_{32} + (\alpha_2 - \alpha_4) C_{42} - (\alpha_1 - \alpha_3) C_{13} - (\alpha_1 + \alpha_3) C_{23} + (\alpha_2 + \alpha_4) C_{33} - (\alpha_2 - \alpha_4) C_{43} = 0 \tag{2-30}$$

$$-\mu_3 C_{11} + \mu_1 C_{21} + \mu_4 C_{31} - \mu_2 C_{41} + \mu_3 C_{12} - \mu_1 C_{22} - \mu_4 C_{32} + \mu_2 C_{42} = 0 \tag{2-31}$$

$$-\alpha_3 C_{12} + \alpha_1 C_{22} + \alpha_4 C_{32} - \alpha_2 C_{42} + \alpha_3 C_{13} - \alpha_1 C_{23} - \alpha_4 C_{33} + \alpha_2 C_{43} = 0 \tag{2-32}$$

$$-(\mu_1 + \mu_3) C_{11} + (\mu_1 - \mu_3) C_{21} + (\mu_2 - \mu_4) C_{31} + (\mu_2 + \mu_4) C_{41} + (\mu_1 + \mu_3) C_{12} - (\mu_1 - \mu_3) C_{22} - (\mu_2 - \mu_4) C_{32} - (\mu_2 + \mu_4) C_{42} = 0 \tag{2-33}$$

$$-(\alpha_1 + \alpha_3) C_{12} + (\alpha_1 - \alpha_3) C_{22} + (\alpha_2 - \alpha_4) C_{32} + (\alpha_2 + \alpha_4) C_{42} + (\alpha_1 + \alpha_3) C_{13} - (\alpha_1 - \alpha_3) C_{23} - (\alpha_2 - \alpha_4) C_{33} - (\alpha_2 + \alpha_4) C_{43} = 0 \tag{2-34}$$

Simultaneous solution of Eqs. (2-23) through (2-34) yields the required expressions for the 12 constants C_{ji}, j = 1, 2, 3, 4, i = 1, 2, 3. They are as follows:

$$C_{11} = \frac{A_{22}\,A_{13} - A_{12}\,A_{23}}{A_{11}\,A_{22} - A_{12}\,A_{21}}\ \frac{pR^2}{Et}\ , \tag{2-35}$$

$$C_{21} = \frac{A_{11}\,A_{23} - A_{21}\,A_{13}}{A_{11}\,A_{22} - A_{12}\,A_{21}}\ \frac{pR^2}{Et}\ , \tag{2-36}$$

where

$$\left.\begin{aligned}
A_{11} &= (\lambda_2 - \lambda_4)^2 - (\lambda_1 + \lambda_3)^2 \\
A_{12} &= 2(\lambda_1^{\,2} - \lambda_2^{\,2}) \\
A_{13} &= (\alpha_2 - \mu_2)(\lambda_1 + \lambda_3)^2 - 2\,(\alpha_4 - \mu_4)\,\lambda_1^{\,2} - (\alpha_1 - \mu_1) \\
A_{21} &= 2(\lambda_4^{\,2} - \lambda_3^{\,2}) \\
A_{22} &= (\lambda_2 + \lambda_4)^2 - (\lambda_1 - \lambda_3)^2 \\
A_{23} &= (\alpha_4 - \mu_4)(\lambda_1 - \lambda_3)^2 + 2(\alpha_2 - \mu_2)\,\lambda_3^{\,2} - (\alpha_3 - \mu_3).
\end{aligned}\right\} \tag{2-37}$$

$$C_{31} = (\lambda_2 - \lambda_4)^2\,C_{11} - 2\,\lambda_2^{\,2}\,C_{21} \tag{2-38}$$

$$C_{41} = 2\,\lambda_4^{\,2}\,C_{11} + (\lambda_2 + \lambda_4)^2\,C_{21} \tag{2-39}$$

$$C_{12} = C_{11} - \mu_2\ pR^2/2Et \tag{2-40}$$

$$C_{22} = C_{21} - \mu_4\ pR^2/2Et \tag{2-41}$$

$$C_{32} = C_{31} - \mu_1\ pR^2/2Et \tag{2-42}$$

$$C_{42} = C_{41} - \mu_3\ pR^2/2Et \tag{2-43}$$

$$C_{13} = C_{11} + (\alpha_2 - \mu_2)\ pR^2/2Et \tag{2-44}$$

$$C_{23} = C_{21} + (\alpha_4 - \mu_4)\ pR^2/2Et \tag{2-45}$$

$$C_{33} = C_{31} + (\alpha_1 - \mu_1)\ pR^2/2Et \tag{2-46}$$

$$C_{43} = C_{41} + (\alpha_3 - \mu_3)\ pR^2/2Et \qquad (2\text{-}47)$$

Numerical Calculations. -- The equations of the foregoing analysis were computerized. Using the following data, the deflection w_o at the midpoint of each ring was computed. These deflections together with the values of a and b are given in Table II.

$R \simeq 15/32$ in., $t \simeq 1/16$ in.

$2\ell \simeq 0.956$ in., $p \simeq 65$ psi as per Part 1.

$E \simeq 8.1 \times 10^6$ psi, $\nu \simeq 0.31$

width of a ring $\simeq 0.077$ in.

This value of ring width includes half of the gaps on both sides of the ring. Rings are numbered 1 through 10 starting from the left end of the shell.

TABLE II

PIEZOELECTRIC SHELL DEFLECTIONS
AT MIDPOINTS OF CONDUCTING RINGS

Ring No.	a (in.)	b (in.)	w_o (in x 10^{-6})
1	-0.3935	-0.4705	16.83
2	-0.3165	-0.3935	8.96
3	-0.2395	-0.3165	8.29
4	-0.1625	-0.2395	8.24
5	-0.0855	-0.1625	8.08
6	0.1625	0.0855	8.08
7	0.2395	0.1625	8.24
8	0.3165	0.2395	8.29
9	0.3935	0.3165	8.96
10	0.4705	0.3935	16.83

With this information and some from Part 1, the mechanics of separation of the piezoelectric shell from the shaft in the region of an electrically excited ring may be explained. Recall from Part 1 that the shrink pressure is

65 psi outward and the corresponding deflection of the piezoelectric shell is approximately 24 microinches. This is plotted in Figure 16(a). Table II gives the deflections at the midpoint of the rings due to a narrow band of 65 psi of pressure in the inward direction, the band width in each case being equal to that of the ring. These pressures and deflections for a typical ring are plotted in Figure 16(b). Superposition of the corresponding plots of Figures 16(a) and 16(b) yields the pressure and deflection plots of Figure 16(c). The

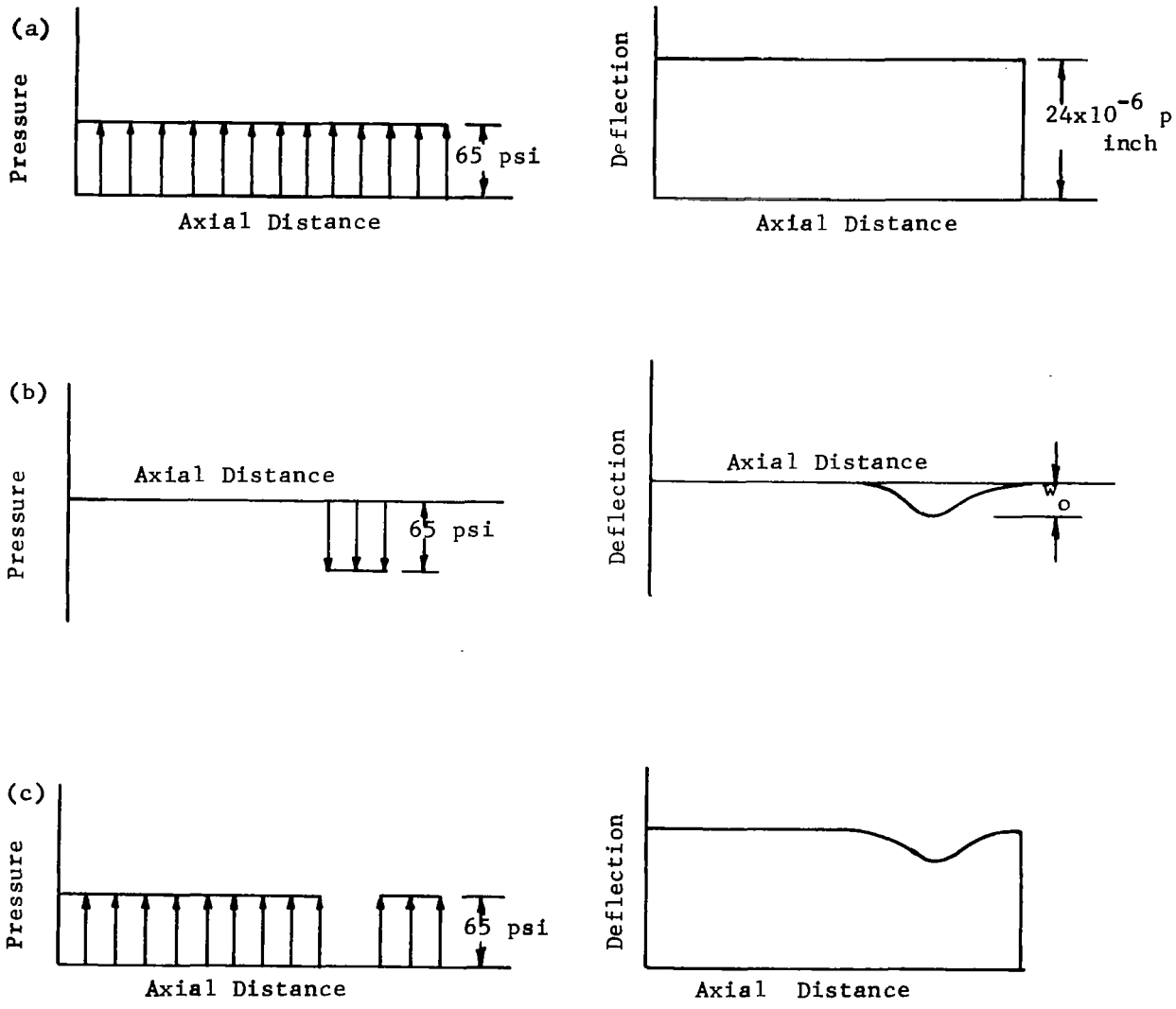

Figure 16. Pressure Deflection Plots and Mechanics of Separation

pressure in the region of the ring has now become zero which signifies the beginning of local separation. In practice, the pressure reduction in the region of the ring is accomplished by exciting the ring electrically. Let V_o denote the voltage required to nullify the 65-psi pressure on the ring. w_o is the deflection corresponding to this pressure. Then if Ω denotes the deflection of the shell per volt,

$$V_o = \frac{w_o}{\Omega} \tag{2-48}$$

From Ref. 5,

$$\frac{\Delta R}{R} = \frac{V}{t} d_{31}$$

or

$$\Omega = \frac{\Delta R}{V} = \frac{R}{t} d_{31}$$

From Ref. 6,

$$d_{31} = 171 \times 10^{-12} \text{ meters/volt} = 0.673 \times 10^{-8} \text{ in./volt}$$

Therefore,

$$\Omega = \frac{R}{t} d_{31} = \frac{15}{32} \times \frac{16}{1} \times 0.673 \times 10^{-8} \simeq 5.05 \times 10^{-8} \text{ in./volt}$$

V_o can be calculated for each ring by using Eq. (2-48) and Table II. The results are summarized in Table III. The separation voltage is fairly constant

TABLE III

SEPARATION VOLTAGES

Ring No.	1,10	2,9	3,8	4,7	5,6
Separation Voltage	333	177	164	163	160

except for the two extreme rings. This is based on a static analysis in which the voltage is applied to rings one at a time. In practice, the voltage is applied to more than one ring at a time as shown later in Part 3. This will change the separation voltages. In general, the larger the width over which the voltage is applied, the larger is the separation voltage. In the extreme case, when the voltage is applied to the entire surface of the shell, the

separation voltage is the largest, because the separation is required to occur over the entire inner surface. This extreme voltage is approximately (24 x 10^{-6} inches)/(5.05 x 10^{-8} inches/volt) = 475 volts. At the opposite extreme, when the ring is very narrow, the separation is required over a very small area and the corresponding voltage is also small. Uniform pressure distributions have been assumed in these calculations for simplicity.

The analysis of Part 2 was initiated with a view to extending it to calculate the axial displacement of the piezoelectric shell. Since a simpler, but no less useful, mathematical model was found, the extension of the analysis was dispensed with. The new mathematical model is considered in Part 3, which thoroughly explains the experimentally observed behavior of the actuator.

Part 3, Relative Axial Displacement Between the Shaft and the Piezoelectric Cylinder

The axial displacement of the actuator shaft relative to the mounting plate is caused by the axial displacement of the piezoelectric cylinder, which is shrink-fitted on the shaft. The axial displacement of the cylinder is, in general, not confined to the narrow ring to which the voltage is applied, but takes place throughout the length of the cylinder, and depends on many contributing factors. An analysis incorporating all the factors is highly involved and prohibitively expensive. Therefore, only a simplified analysis based on a number of assumptions has been attempted. The analysis directly ignores (1) the dynamic nature of the problem, (2) anisotropy of the cylinder, (3) damping and hysteresis, (4) fringing of the electric field, and (5) any nonlinearity that may exist. It only indirectly considers the effect of friction. Linear elastic equations are used. The shrink pressure between the shaft and the cylinder is assumed to be uniform (see Part 1). The reduction in this pressure caused by the application of voltage to any ring is also assumed to be uniform and to be confined to a narrow band whose width equals that of the ring (see Part 2). The shaft is assumed to be rigid in comparison to the cylinder. This assumption has been verified by calculations (see Part 1). The analysis is focused on the axial displacement of the middle cross section of the cylinder relative to the shaft, which is assumed to be grounded, and the mounting plate at the mid-cross section is set free to move

axially. The analytical displacement of the mid-cross section is, therefore, in a direction opposite to that in which the shaft would move if it were free and the mounting plate were grounded.

The analytical model is shown in Figure 17. The compliances k_1 and k_2 in the figure do not represent any springs, but only simulate the axial displacements of the two ends. The dotted line represents the stationary cross section in the electrically excited ring which expands axially because of the piezoelectric effect. The notation used in the analysis is as follows:

ℓ	=	length of the cylinder	(in.)
R_1	=	inner radius of the cylinder	(in.)
R_2	=	outer radius of the cylinder	(in.)
x	=	axial coordinate	(in.)
a	=	distance of the left edge of the electrically excited ring from the left end of the cylinder	(in.)
b	=	distance of the right edge of the electrically excited ring from the right end of the cylinder	(in.)
c	=	width of the electrically excited ring	(in.)
d	=	distance of the stationary cross section from the left end of the cylinder	(in.)
d_o	=	distance of the mid-cross section of the ring from the left end of the cylinder	(in.)
ξ	=	distance of the stationary cross section from the left edge of the ring	(in.)
k_1, k_2	=	equivalent compliances at the left and right ends, respectively	(in./lb.)
α	=	coefficient of axial expansion due to piezoelectric effect	(in./in./volt)
V	=	voltage applied to the ring	(volt)
E	=	average Young's modulus	(psi)
A	=	area of cross section of the cylinder	($in.^2$)
u	=	axial displacement	(in.)
u_o	=	axial displacement at $x = \ell/2$	(in.)
Δ	=	total axial expansion of the ring	(in.)
δ_o	=	net axial displacement due to one complete pulse train	(in.)

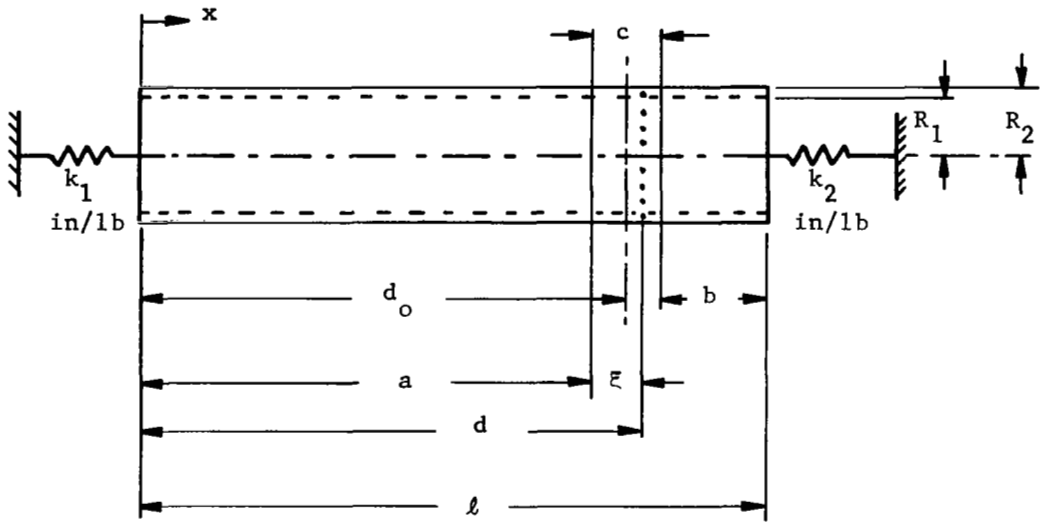

Figure 17. Analytical Model for the Axial Displacement of the Piezoelectric Cylinder

f = factor defining the location of the stationary cross section; lies in the range: $-1/2 \leq f \leq 1/2$.

ϵ = axial strain (in./in.)

n = coefficient that determines the concavity of the compliances (k_1 and k_2) curves

P = effective axial compressive force on the piezoelectric cylinder (lb.)

The axial expansion of a ring due to the application of voltage is not free, but is restrained because of friction and continuity of the piezoelectric material. This results in compression of the material and axial displacement of varying magnitude everywhere. A typical linearized displacement curve may be as shown in Figure 18. In terms of the effective axial compressive force P, which is to be determined later, the unit strains in the ring and in the parts of the cylinder to the left and to the right of the ring are as follows:

$$\left.\begin{aligned} \frac{du}{dx} &= \epsilon = -\frac{P}{AE} \quad \text{(contraction)}, \quad 0 \leq x \leq a \\ \frac{du}{dx} &= \epsilon = \alpha V - \frac{P}{AE} \quad \text{(expansion)}, \quad a \leq x \leq a + c \\ \frac{du}{dx} &= \epsilon = -\frac{P}{AE} \quad \text{(contraction)}, \quad a + c \leq x \leq \ell \end{aligned}\right\} \tag{3-1}$$

Integration of Eq. (3-1) yields the following:

$$u = -\frac{P}{AE} x + c_1, \quad 0 \leq x \leq a \tag{3-2}$$

$$u = \alpha V x - \frac{P}{AE} x + c_2, \quad a \leq x \leq a + c \tag{3-3}$$

$$u = -\frac{P}{AE} x + c_3, \quad a + c \leq x \leq \ell \tag{3-4}$$

c_1, c_2, c_3 and P can be evaluated by applying the boundary conditions and conditions of continuous displacement.

At $x = 0$, $u = -k_1 P$; therefore, $c_1 = -k P$; therefore,

$$u = -\frac{P}{AE} x - k_1 P, \quad 0 \leq x \leq a \tag{3-5}$$

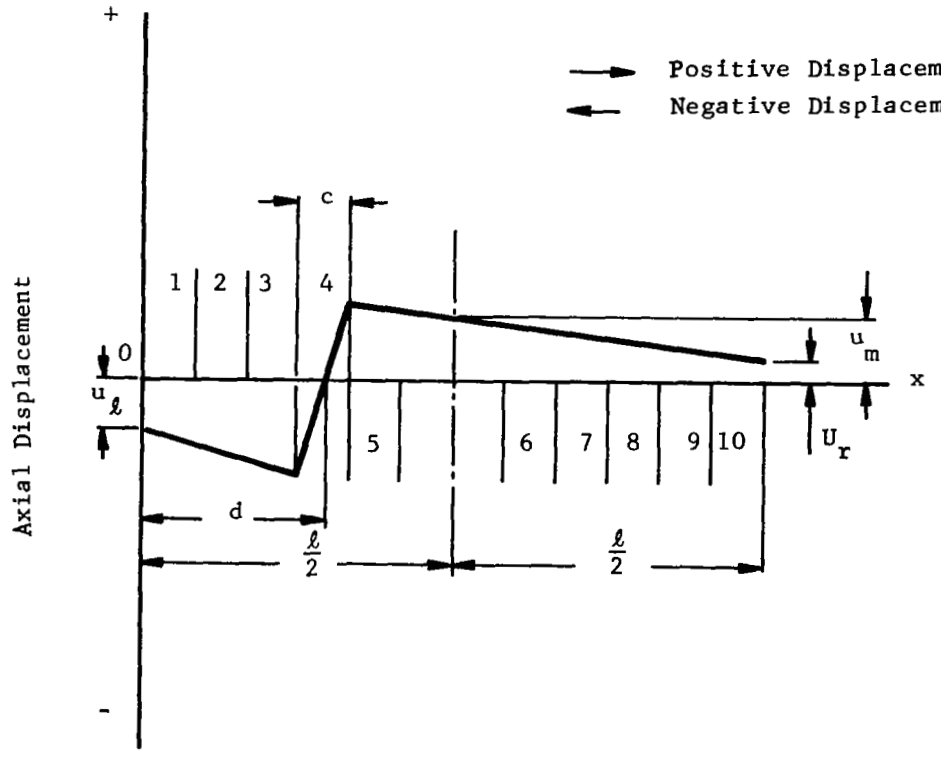

Figure 18. Typical Linearized Curve for the Axial Displacement of the Cylinder

At x = a, u in Eq. (3-3) equals u in Eq. (3-5); therefore

$$\alpha V a - \frac{P}{AE} a + c_2 = - \frac{P}{AE} a - k_1 P$$

Therefore, $c_2 = - k_1 P - \alpha V a$

Therefore,

$$u = \alpha V (x - a) - \frac{P}{AE} x - k_1 P, \quad a \leq x \leq a + c \tag{3-6}$$

At $x = \ell$, $u = k_2 P$; therefore, $c_3 = k_2 P + \frac{P\ell}{AE}$; therefore,

$$u = \frac{P}{AE} (\ell - x) + k_2 P, \quad a + c \leq x \leq \ell \tag{3-7}$$

At x = a + c, u in Eq. (3-6) equals u in Eq. (3-7); therefore

$$\alpha V (a + c - a) - \frac{P}{AE} (a + c) - k_1 P = \frac{P}{AE} (\ell - a - c) + k_2 P$$

or,

$$P = \frac{AE\ \alpha V c}{\ell + AE(k_1 + k_2)} \tag{3-8}$$

Eliminating P from Eqs. (3-5), (3-6) and (3-7) by using Eq. (3-8), we have the following displacement equations.

$o \leq x \leq a$:

$$u = - \alpha V \frac{c(x + AE\ k_1)}{\ell + AE\ (k_1 + k_2)} \tag{3-9}$$

$a \leq x \leq a + c$:

$$u = \alpha V \left[\frac{\{(a + b) + AE(k_1 + k_2)\} x - AE\ k_1\ c}{\ell + AE\ (k_1 + k_2)} - a \right] \tag{3-10}$$

$a + c \leq x \leq \ell$:

$$u = \alpha V \frac{c[(\ell - x) + AEk_2]}{\ell + AE\ (k_1 + k_2)} \tag{3-11}$$

Since u = o at x = d, we have, from Eq. (3-10),

$$\frac{[(a + b) + AE\ (k_1 + k_2)]\ d - AE\ k_1 c}{\ell + AE\ (k_1 + k_2)} - a = o,$$

or,

$$d = \frac{a\ell + AE\,[(a + c)\,k_1 + ak_2]}{(a + b) + AE\,(k_1 + k_2)} \tag{3-12}$$

Therefore,

$$\xi = d - a = \frac{(a + AE\,k_1)c}{(a + b) + AE\,(k_1 + k_2)} \tag{3-13}$$

Special cases. --

(1) Both ends are fixed.

$k_1 = k_2 = 0$

$\xi = \frac{a}{a + b}\ c.$

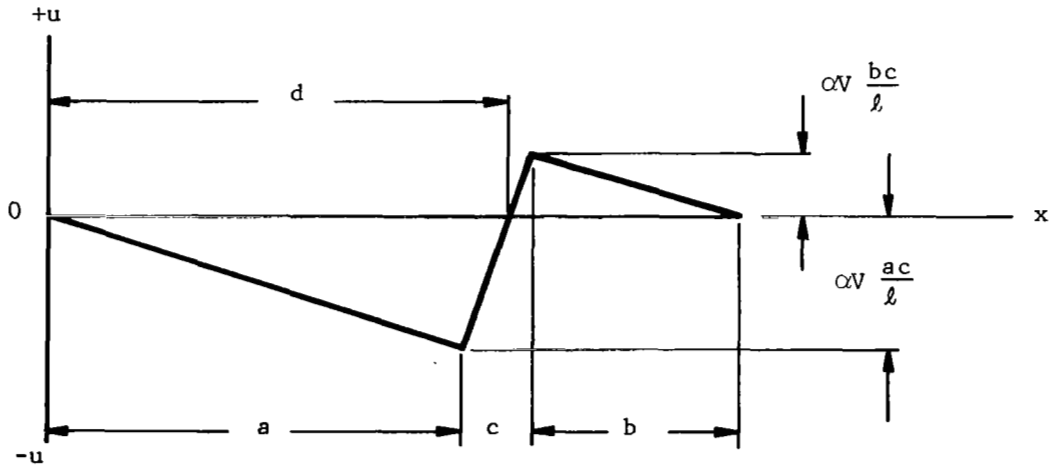

(2) Both ends are free.

$k_1 = k_2 = \infty.$

$\xi = \frac{c}{2}$

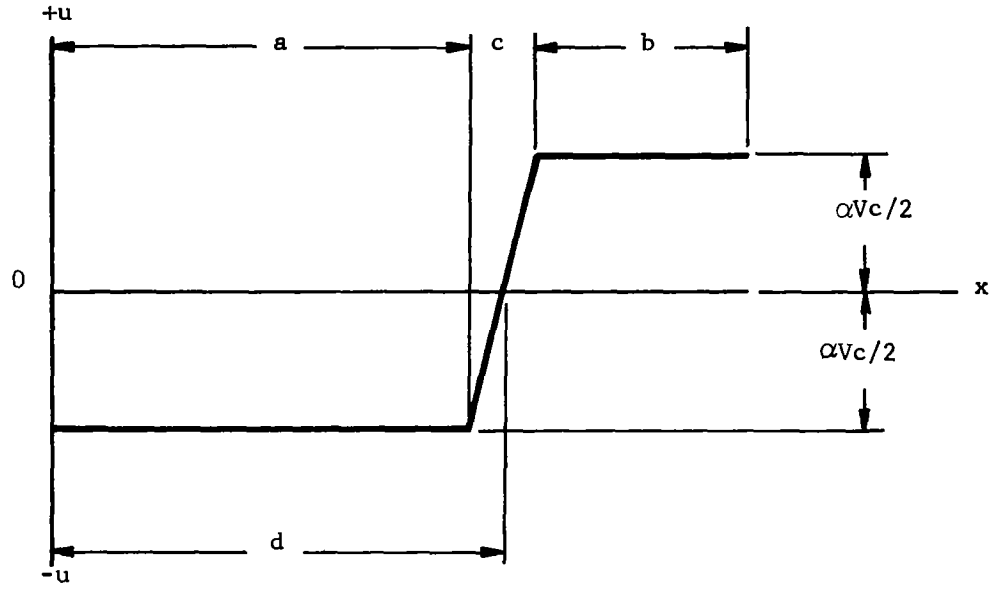

(3) Left end fixed, right end free.

$k_1 = 0,\ k_2 = \infty.$

$\xi = 0.$

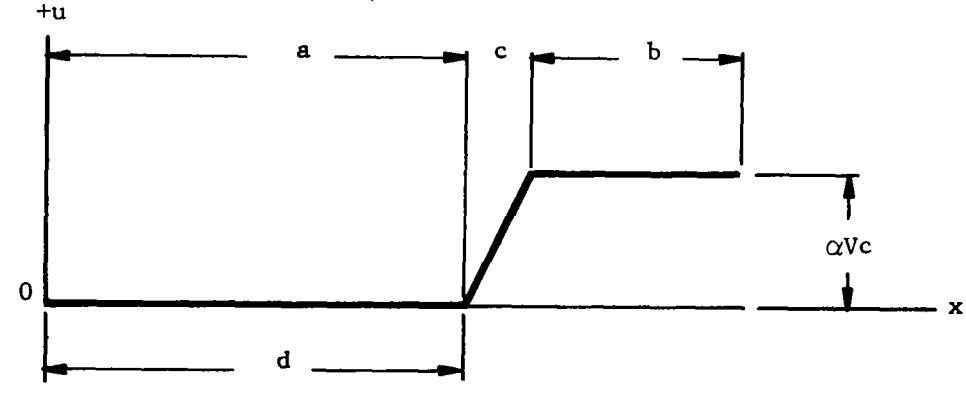

(4) Left end free, right end fixed.

$k_1 = \infty$, $k_2 = 0$.

$\xi = c$.

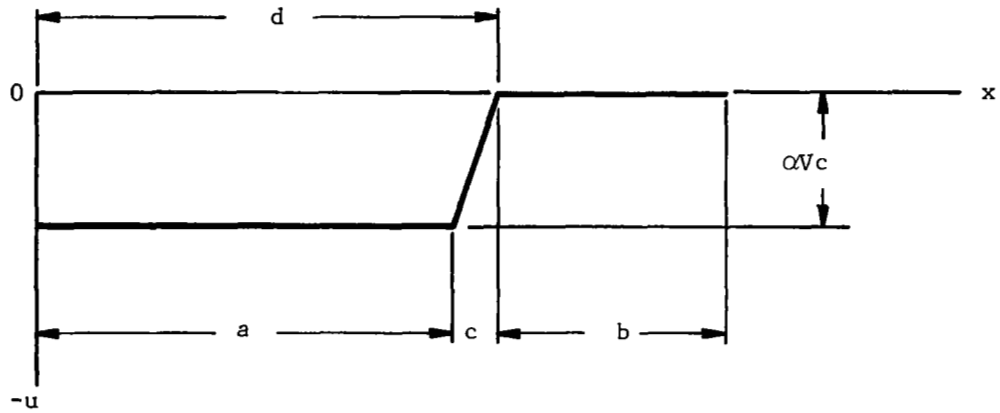

(5) Left end fixed, right end partially fixed and partially free.

$k_1 = 0$, $k_2 = k$ = finite.

$$\xi = \frac{a}{(a + b) + AEk}\, c.$$

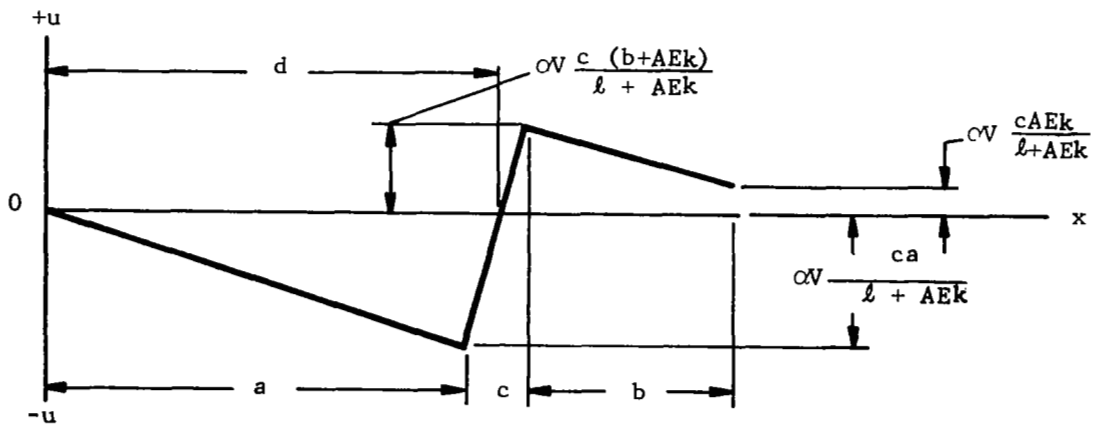

(6) Left end partially fixed and partially free, right end fixed.

$k_1 = k$ = finite, $k_2 = 0$.

$$\xi = \frac{a + AEk}{(a + b) + AEk}\, c$$

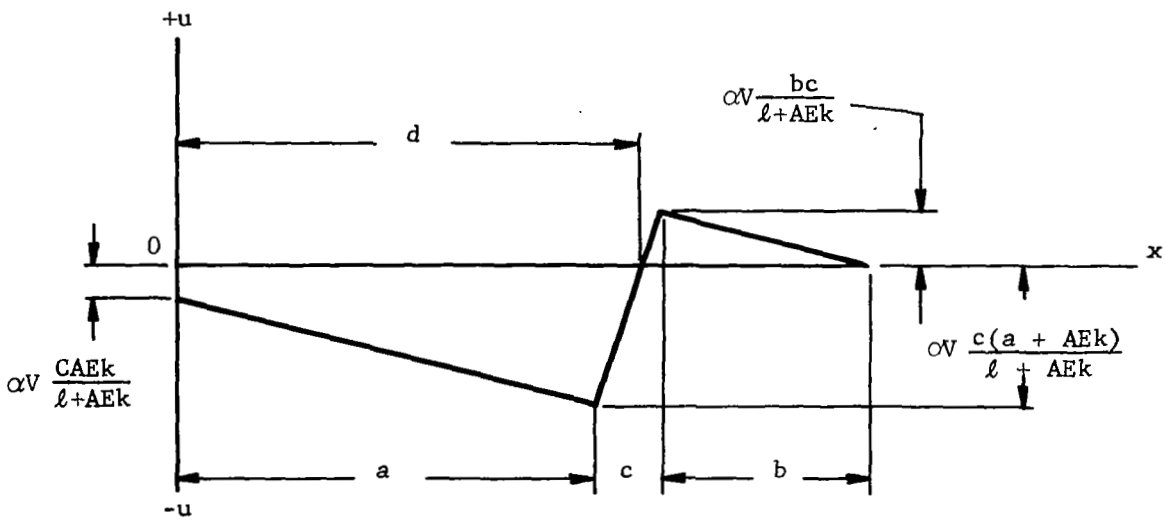

(7) Both ends partially fixed and partially free.

k_1 and k_2 are both nonzero and finite. This is the most general case.

$x = 0$: $\quad u_\ell = -\alpha V \dfrac{cAEK_1}{\ell + AE(k_1 + k_2)}$

$x = a$: $\quad u_a = -\alpha V \dfrac{a + cAEk_1}{\ell + AE(k_1 + k_2)}$

$x = d$: $\quad u_d = 0$

$x = a + c$: $\quad u_b = \dfrac{c(b + AEk_2)}{\ell + AE(k_1 + k_2)}\ \alpha V$

$x = \ell$: $\quad u_r = \alpha V \dfrac{cAEk_2}{\ell + AE(k_1 + k_2)}$

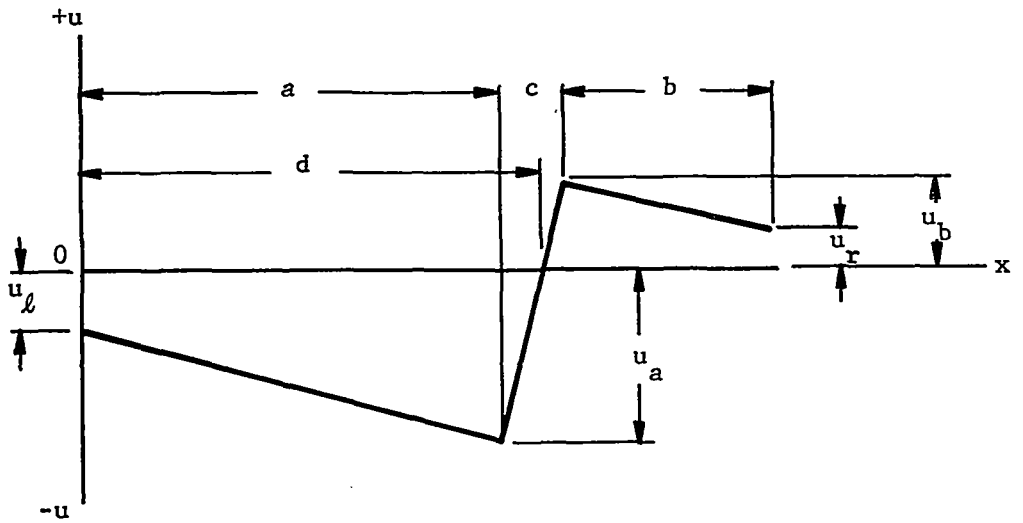

Axial Expansion of the Electrically Excited Ring

$$\Delta = u_b - u_a = \alpha V \frac{c[(a + b) + AE\ (k_1 + k_2)]}{\ell + AE(k_1 + k_2)} \qquad (3\text{-}14)$$

Approximate Determination of d

Eq. (3-12) gives the location of the stationary cross section in the excited ring in terms of k_1 and k_2. These compliances are yet unknown and can, in general, take any values. It is necessary to establish their useful range of values pertinent to the problem under consideration. The approximate determination of d, undertaken here, is a first step toward this goal.

d depends on the position d_o of the excited ring, which is given by

$$d_o = a + c/2. \qquad (3\text{-}15)$$

Let d be assumed to be a linear function of d_o

$$d = \beta_1 + \beta_2 d_o, \tag{3-16}$$

where β_1 and β_2 are constants. By symmetry,

$$d = \ell/2 \text{ at } d_o = \ell/2.$$

Therefore,

$$\beta_1 = \ell/2 - \beta_2 \ell/2.$$

Substitution for β_1 in Eq. (3-16) yields

$$d = \ell/2 + \beta_2 (d_o - \ell/2). \tag{3-17}$$

Now introduce a parameter f such that

$$d = d_o + fc \text{ at } d_o = c/2,$$

where the range of f should be $-1/2 \leq f \leq 1/2$ in order that the stationary cross section remain within the excited ring. Then from Eq. (3-17)

$$\beta_2 = 1 + 2fc/(c-\ell).$$

Substitute this expression for β_2 into Eq. (3-17). Then

$$d = \frac{\ell}{2} + \left[1 + \frac{2fc}{c-\ell}\right] (d_o - \ell/2). \tag{3-18a}$$

Thus d is obtained in terms of the parameter f whose range of values is known. Knowing d Eq. (3-12) can be used in the determination k_1 and k_2.

It may be noted that, if d is taken as a parabolic function of d_o such as

$$d = \beta_3 + \beta_4 d_o^2,$$

the same reasoning as above will give

$$d = \frac{\ell}{2} + \frac{2[\ell-(1+2f)c]}{\ell^2-c^2} \left[d_o^2 - \frac{\ell^2}{4}\right]. \tag{3-18b}$$

Approximate Determination of k_1 and k_2

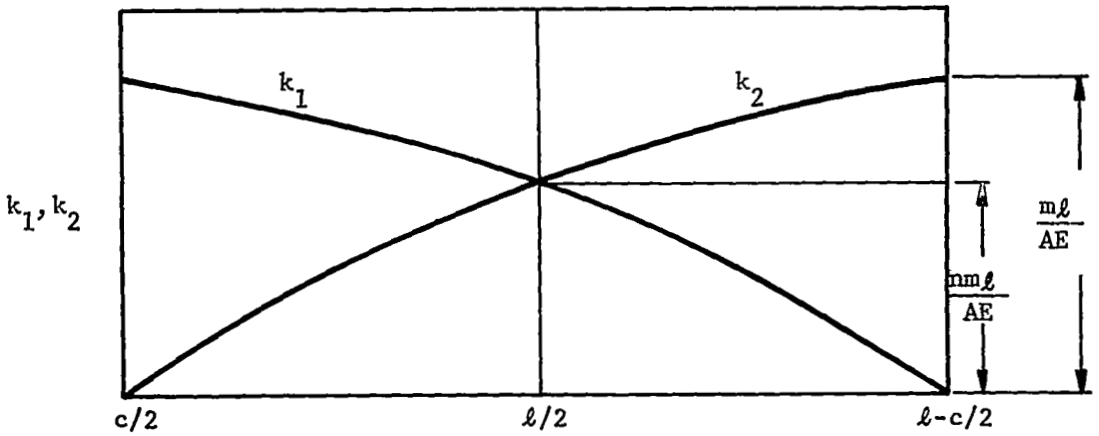

$$d_o = a + c/2$$

Like d, k_1 and k_2 also depend on the position d_o of the excited ring. Let k_1 be assumed to be a second-degree function of d_o, given by

$$k_1 = [\lambda_1 + \lambda_2 d_o + \lambda_3 d_o^2] \frac{\ell}{AE}, \qquad (3\text{-}19)$$

where λ_1, λ_2, and λ_3 will be determined in terms of the known parameter f and a new parameter n. The concavity of the compliance curve depends on n. For example, if $n = \frac{1}{2}$, the curve is a straight line. If $n > \frac{1}{2}$, the curvature is downward and, if $n < \frac{1}{2}$, the curvature is upward. The quantity m in the figure will also be obtained in terms of f and n.

By symmetry of k_1 and k_2 with respect to $d_o = \ell/2$, if $k_1 = g(d_o)$, then $k_2 = g(\ell - d_o)$ where g denotes a function. Therefore, by Eq. (3-19),

$$k_2 = [\lambda_1 + \lambda_2 (\ell - d_o) + \lambda_3 (\ell - d_o)^2] \frac{\ell}{AE} \qquad (3\text{-}20)$$

Let us now proceed to determine λ_1, λ_2, and λ_3 in terms of m and n and m in terms of f and n, so that k_1 and k_2 are eventually known in terms of f and n.

When an end ring is excited, the axial displacement of the other end is negligible provided that the cylinder is not short. Consequently, we may take

$$k_1 = 0 \text{ at } d_o = \ell - c/2.$$

Therefore, from Eq. (3-19)

$$\lambda_1 + \lambda_2 (\ell - c/2) + \lambda_3 (\ell - c/2)^2 = 0 \tag{3.a}$$

Also,

$$k_1 = \frac{m\ell}{AE} \text{ at } d_o = c/2.$$

Therefore, by Eq. (3-19)

$$\lambda_1 + \lambda_2 \, c/2 + \lambda_3 \, c^2/4 = m. \tag{3.b}$$

And,

$$k_1 = n \frac{m\ell}{AE} \text{ at } d_o = \ell/2.$$

So, Eq. (3-19) gives

$$\lambda_1 + \lambda_2 \, \ell/2 + \lambda_3 \, \ell^2/4 = nm. \tag{3.c}$$

Solve Eqs. (3.a), (3.b), and (3.c) simultaneously for λ_1, λ_2, and λ_3.

$$\lambda_1 = \frac{(\ell - c/2)(\ell - 2nc)}{(\ell - c)^2} \, m$$

$$\lambda_2 = \frac{c + (4n-3)\ell}{(\ell - c)^2} \, m$$

$$\lambda_3 = \frac{2(1-2n)}{(\ell - c)^2} \, m.$$

Upon substitution of these expressions for λ's, Eqs. (3-19) and (3-20) become

$$k_1 = \left[(\ell-c/2)(\ell-2nc) + [c+(4n-3)\ell]d_o + 2(1-2n)d_o^2\right] \frac{\ell/AE}{(\ell-c)^2} m \tag{3-21}$$

$$k_2 = \left[[\ell-4n(\ell-c/2)]\, c/2 + [(4n-1)\ell-c]\, d_o + 2(1-2n)\, d_o^2\right] \frac{\ell/AE}{(\ell-c)^2} m \tag{3-22}$$

It now remains to obtain m in terms of f and n. Eliminate k_1 and k_2 from Eq. (3-12) by using Eqs. (3-21) and (3-22) and solve the resulting equation for m.

$$(a+b)d + \frac{m\ell d}{(\ell-c)^2}\left[\ell^2+2nc(c-2\ell) + 4(1-2n)d_o(d_o-\ell)\right]$$

$$= a\ell + \frac{m\ell}{(\ell-c)^2}\left[a\left[\ell^2+2nc(c-2\ell) + 4(1-2n)d_o(d_o-\ell)\right] + c\left\{(\ell-c/2)(\ell-2nc) + [c+(4n-3)\ell]\, d_o + 2(1-2n)d_o^2\right\}\right]$$

Therefore,

$$m = \left[\frac{[(a+b)d-a\ell](\ell-c)^2/\ell}{(a-d)[\ell^2+2nc(c-2\ell) + 4(1-2n)d_o(d_o-\ell)] + c[(\ell-c/2)(\ell-2nc) + \{c + (4n-3)\ell\}d_o+2(1-2n)d_o^2]}\right] \tag{3-23}$$

Since, by Eq. (3-18), d depends on f, m is obtainable in terms of f and n. Therefore k_1 and k_2 in Eqs. (3-19) and (3-20) are obtainable in terms of the parameters f and n. f controls the location of the stationary cross section in the excited ring and falls in the range $-1/2 \leq f \leq 1/2$. The curvature of the compliance curves given by Eqs. (3-19) and (3-20) depends on n. These curves are straight lines if $n = 1/2$. The useful range of n may approximately be taken as $0.2 \leq n \leq 0.8$.

The equations of the foregoing analysis will be used later for numerical calculations. Before making the numerical calculations, we shall attempt to explain some important features of the actuator motion.

A Qualitative Discussion of Actuator Motion

The piezoelectric cylinder has 10 conducting rings, 5 on either side of the mounting plate which is in the middle. When voltage is applied to any ring, for example No. 4, the material moves away on both sides from a stationary cross section in the ring. The displacements u_ℓ and u_r of the left and right ends of the cylinder depend, among other things, on the distances of the two ends from the excited ring. The larger this distance is, the smaller is the end displacement. The displacement of the mid-cross section is denoted by u_m.

Let u_{mi} denote the axial displacement of the mid-cross section due to the excitation of the i th ring. On this basis, the displacement in Figure 18 is u_{m4}. By symmetry, the following relations hold in the static case for a given voltage.

$$\left.\begin{aligned} u_{m6} &= -(u_{m5}) \\ u_{m7} &= -(u_{m4}) \\ u_{m8} &= -(u_{m3}) \\ u_{m9} &= -(u_{m2}) \\ u_{m10} &= -(u_{m1}) \end{aligned}\right\} \qquad (3\text{-}24)$$

These relations will be applied to calculate at any instant the axial displacement δ of the mid-cross section due to the applied electric pulse train which is as shown in Figure 19. Pulse in each ring acts for a time interval $2\,\Delta\,t$. When the $(i+1)$th ring is excited, the pulse on the $(i-1)$th ring is taken off. The displacement of the mid-cross section, due to the expansion of a ring that is being excited, will be identified with a positive sign in front of it and, that due to the contraction of a ring on which the voltage is being taken off, will be identified with a negative sign in front. At any instant, the voltage acts on two adjacent rings, the overlap being on time interval $\Delta\,t$. This includes rings 5 and 6 and rings 10 and 1. Table IV gives the construction of the axial displacement δ of the mid-cross section of the cylinder as a function of time for the pulse trains of Figure 18. δ' is the displacement just before and δ is the displacement just after the indicated time. Eq. (3-24) has been used in this construction. Reversing the sign of δ gives the displacement of the actuator shaft relative to the mounting plate. A plot of the shaft displacement based on Table IV is given in Figure 20(a). This plot clearly explains the main features of the actuator motion, in particular, the jumps occurring in the motion when the electric pulse crosses over from the left side of the mounting plate to the right.

Calculations of Table IV can be generalized for an actuator of N rings as follows. For any location along the axial direction, the axial displacement is

$$\begin{aligned} \delta &= u_i + u_{i+1} && \text{at } t/\Delta t = \eta N + i \quad , \\ & && \text{for } i = 1, 2, \ldots\ldots, N-1; \\ \delta &= u_i + u_{(i+1)-N} && \text{at } t/\Delta t = (\eta+1)N \quad , \\ & && \text{for } i = N. \end{aligned} \qquad (3\text{-}25)$$

where $\eta = 0,1,2,3,4,5, \ldots\ldots$, and u_i denotes the axial displacement at the given location due to the excitation of the ith ring.

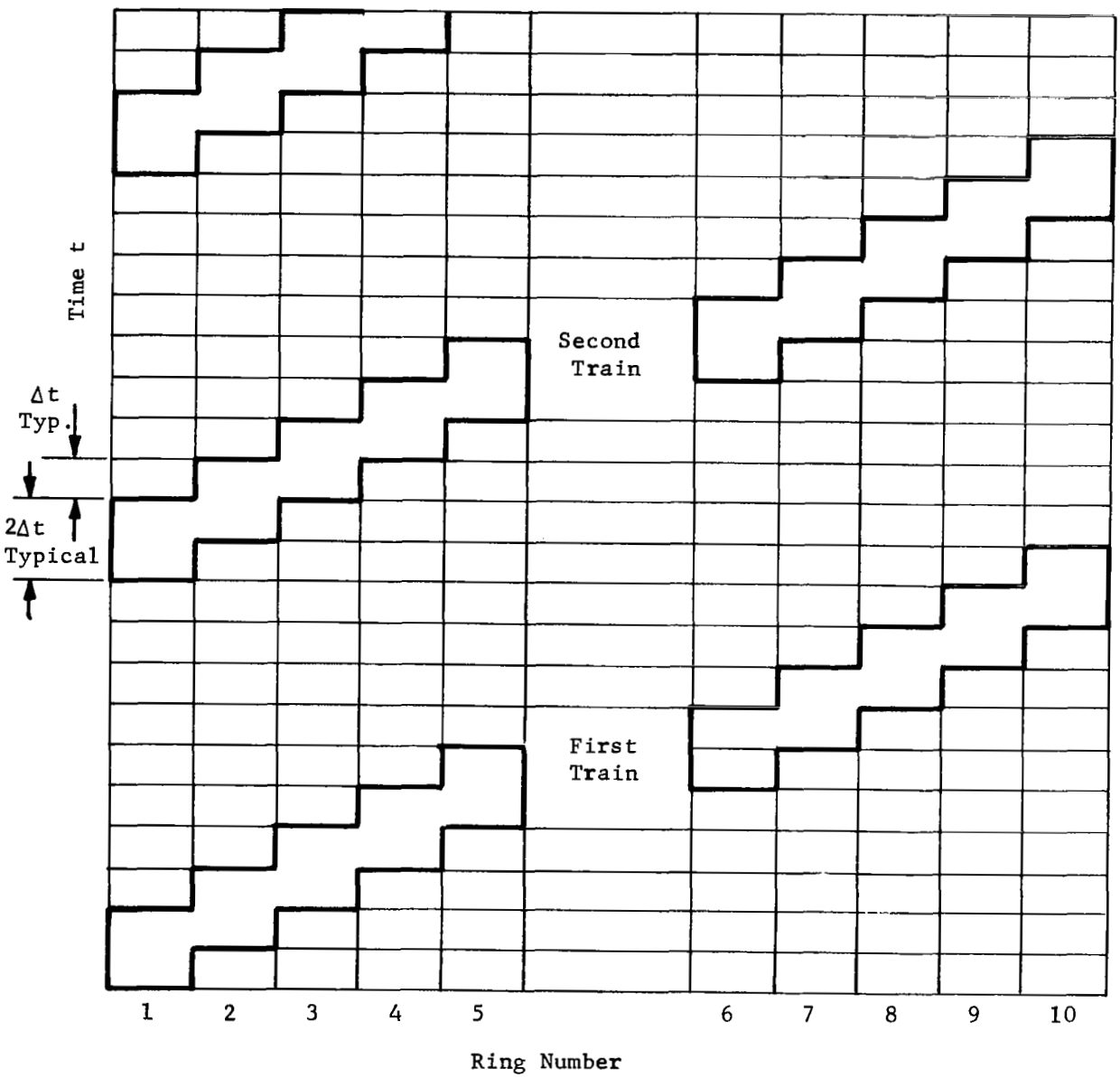

Figure 19. Electric Pulse Trains in the Actuator

TABLE IV

AXIAL DISPLACEMENT OF THE MID-CROSS SECTION OF THE CYLINDER

t	δ'	δ
o	o	u_{m1}
Δt	u_{m1}	$\delta' + u_{m2} = u_{m1} + u_{m2}$
2 Δt	$u_{m1} + u_{m2}$	$\delta' + u_{m3} - u_{m1} = u_{m2} + u_{m3}$
3 Δt	$u_{m2} + u_{m3}$	$\delta' + u_{m4} - u_{m2} = u_{m3} + u_{m4}$
4 Δt	$u_{m3} + u_{m4}$	$\delta' + u_{m5} - u_{m3} = u_{m4} + u_{m5}$
5 Δt	$u_{m4} + u_{m5}$	$\delta' + u_{m6} - u_{m4} = u_{m5} + u_{m6} = 0$
6 Δt	0	$\delta' + u_{m7} - u_{m5} = -(u_{m4} + u_{m5})$
7 Δt	$-(u_{m4} + u_{m5})$	$\delta' + u_{m8} - u_{m6} = -(u_{m3} + u_{m4})$
8 Δt	$-(u_{m3} + u_{m4})$	$\delta' + u_{m9} - u_{m7} = -(u_{m2} + u_{m3})$
9 Δt	$-(u_{m2} + u_{m3})$	$\delta' + u_{m10} - u_{m8} = -(u_{m1} + u_{m2})$
10 Δt	$-(u_{m1} + u_{m2})$	$\delta' + u_{m1} - u_{m9} = -(u_{m2} + u_{m9}) = 0$
11 Δt	0	$\delta' + u_{m2} - u_{m10} = u_{m1} + u_{m2}$
12 Δt	$u_{m1} + u_{m2}$	$\delta' + u_{m3} - u_{m1} = u_{m2} + u_{m3}$
13 Δt	$u_{m2} + u_{m3}$	$\delta' + u_{m4} - u_{m2} = u_{m3} + u_{m4}$

Based on Eqs. (3-25), Figure 20(b) shows the displacement profile of the ten ring actuator when the mounting plate is located at the right end of the cylinder.

Let us now return to Figure 20(a). This figure gives only the oscillatory part of the axial displacement. The net displacement of the oscillatory part for one complete pulse train is zero. We shall superpose the ideal displacement profile on the oscillatory profile to obtain the actual (resultant) profile. The ideal profile for one complete pulse train is shown in Figure 21(a). There is no motion until the pulse crosses the location of the mounting plate. When the pulse crossover occurs, the ideal displacement takes place in two steps of approximately equal magnitudes Δ'. We shall assume Δ' to be of such a magnitude that the sum of Δ' and $|u_{m4} + u_{m5}|$ equals Δ as shown in Figure 21, where Δ is the axial expansion of the excited ring 6 as given by Eq. (3-14). The net axial displacement δ_o of the actuator due to one complete pulse train is given by

$$\delta_o = 2[\Delta - |u_{m4} + u_{m5}|]. \tag{3-26}$$

Correlation Between Analysis and Experiment

The equations of the analysis developed earlier can be used to calculate the axial displacement profile of the actuator. We shall here discuss how to make calculations for the ten-ring actuator given the following data.

$\ell \simeq 1$ in., $R_1 \simeq 7/16$ in., $R_2 \simeq 1/2$ in.

$c \simeq 0.077$ in., $E \simeq 8.1 \times 10^6$ psi, $V = 250$ volts

$f = 0.40$, $n = 0.50$

$A = \pi (R_2^2 - R_1^2) \simeq \pi [(1/2)^2 - (7/16)^2] \simeq 0.1841$ in.^{2}

From Ref. 5,

$$\frac{\Delta \ell}{\ell} = \frac{Vd_{31}}{t}$$

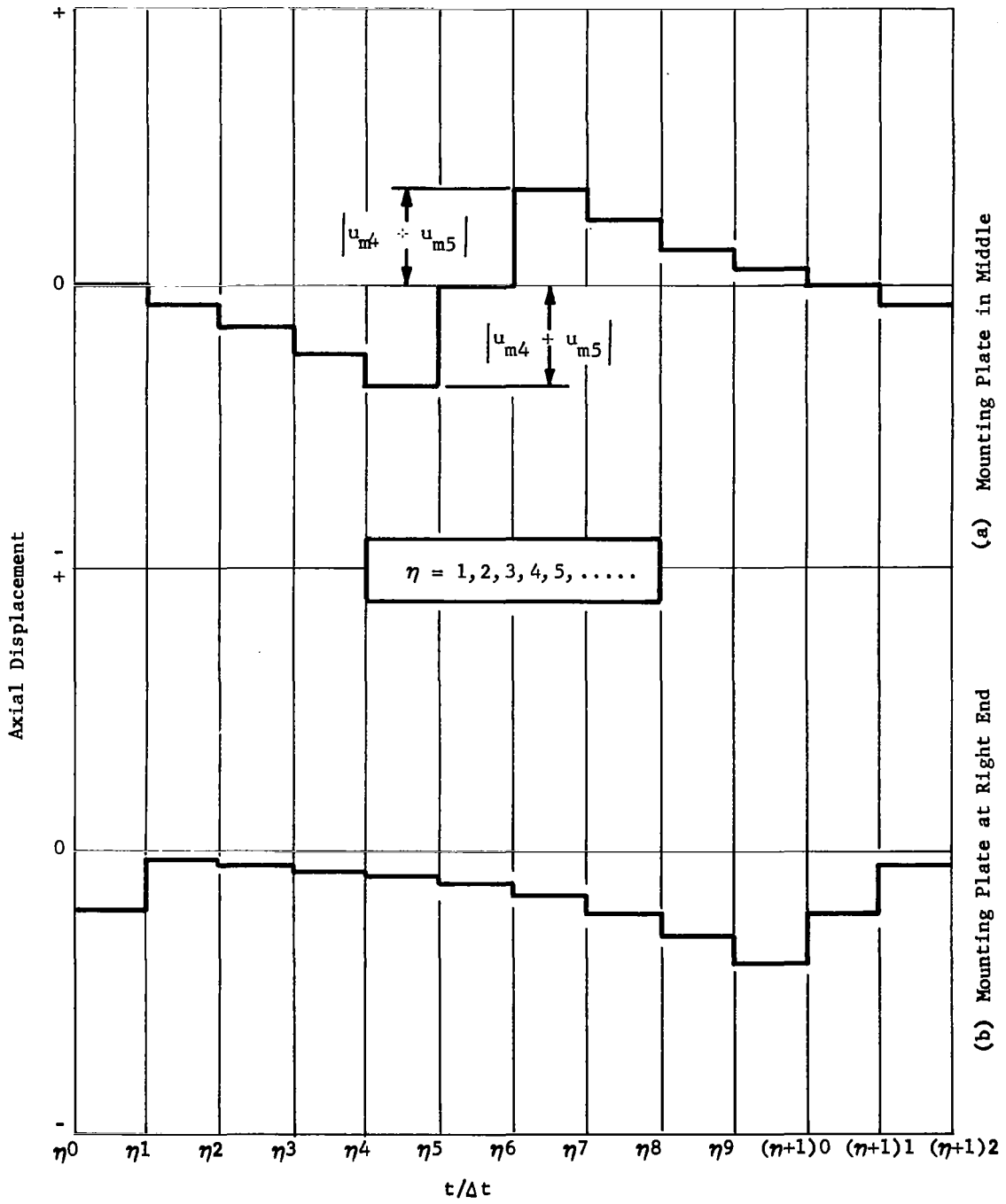

Figure 20. Typical Oscillatory Parts of Displacement Profiles Based on Static Analysis

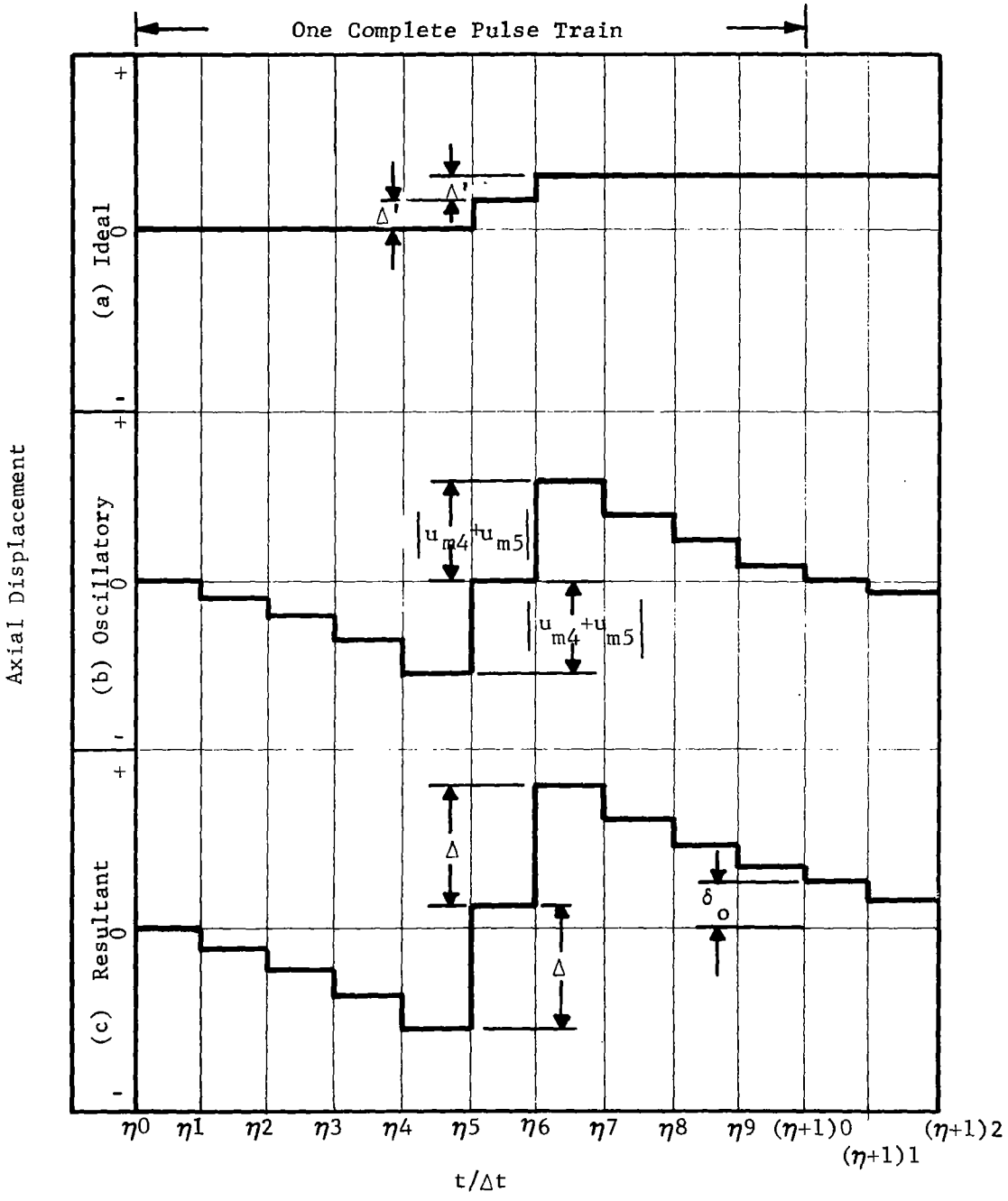

Figure 21. Typical (a) Ideal, (b) Oscillatory and (c) Resultant Displacement Profiles Based on Static Analysis

Therefore, $\alpha = \frac{\Delta \ell}{\ell V} = \frac{d_{31}}{t} = \frac{d_{31}}{R_2 - R_1}$

From page 45,

$d_{31} = 0.673 \times 10^{-8}$ in./volt; therefore,

$$\alpha = \frac{0.673 \times 10^{-8}}{1/16} = 0.1086 \times 10^{-6} \text{ (in./in.)/volt.}$$

It is required to calculate the axial displacement u_{mi} of the middle cross section due to the excitation of ten rings taken one by one ($i = 1,2, \ldots, 9, 10$). By virtue of Eqs. (3-24), we need to make calculations for the first five rings only ($i = 1,2,3,4,5$). The calculation may be carried out in the following order for any value of i.

(1) $a = (i-1)xc$ in Figure 17
(2) $b = \ell - (a+c)$ from Figure 17
(3) d_o from Eq. (3-15)
(4) d from Eq. (3-18a) or Eq. (3-18b)
(5) m from Eq. (3-23)
(6) k_1 and k_2 from Eqs. (3-21) and (3-22), respectively
(7) u_{mi} from Eq. (3-11) for $x = \ell/2$

(Note that this equation is used because $a+c < \ell/2$ for $i = 1,2,3,4,5$.)

(8) Use Table IV or Eqs. (3-24) and (3-25) to construct the the oscillatory profile of Figure 21(b)
(9) Δ from Eq. (3-14)
(10) Construct the resultant profile of Figure 21(c)

Figure 22 compares the experimental and analytical displacement profiles for which the above procedure and numerical data were used in the computer-based calculations. The experimental profile clearly shows the dynamic nature of loading in the form of peaks soon after initiation of each pulse. These peaks are quite prominent when the electric pulse crosses over from one side of the mounting plate to the other. On the whole, the agreement between the two profiles is good.

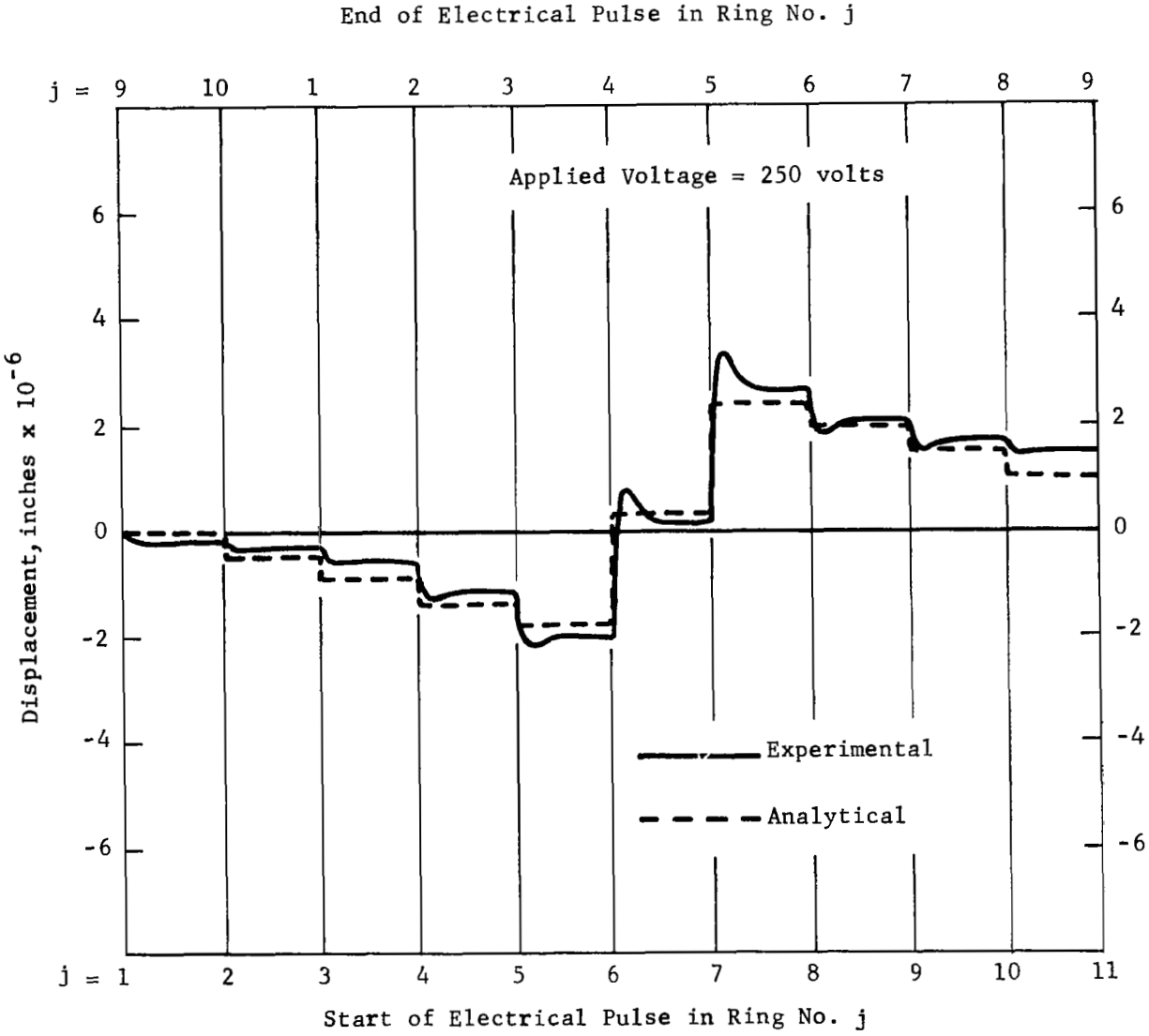

Figure 22. Comparison of Experimental and Theoretical Displacement Profiles

ACTUATOR TESTS

Various tests were performed on the actuators. All of the results, along with samples of the gathered data,are included herein. To insure that the data obtained on actuator performance are traceable to a fixed standard, it was decided to calibrate the Brown & Sharpe electronic dial indicator against an interferometer using the wavelength of light as a reference standard.

Brown & Sharpe Calibration

The measurement and evaluation of the performance characteristics of the peristaltic actuator require the ability to measure and record linear displacements in the range from one-tenth of one-millionth of an inch to several tens of millionths of an inch. The basic instrument we have used to fulfill this requirement is the Brown & Sharpe Electronic Indicator, Model 991,with gage head Model 981. This instrument has four ranges of sensitivity varying from plus-and-minus one-thousandth of an inch full scale to one-millionth of an inch least scale division. This instrument also has analog voltage output proportional to measured displacement capability, which allows the recording of the measured displacements on a standard chart recorder.

Logically, the calibration of the electronic indicator was a prime task to be accomplished. Two techniques were used to calibrate the indicator.

The first technique utilized a differential micrometer, Model No. DS505, manufactured by the Starrett Company and distributed by the Lansing Research Corporation. . This micrometer produces an axial motion of one and one-quarter thousandths of an inch per revolution of the thimble. Each division around the thimble is therefore fifty millionths of an inch and each vernier division is equal to five millionths of an inch. Two electronic indicators were calibrated by the above method. The results of these calibrations are given in Table V.

TABLE V

CALIBRATION RESULTS

Unit	Scale (inch)	Indicated Travel (inch)	Micrometer Travel (inch)	Correction Factor
1	±0.001	0.002	0.00213	1.07
1	±0.0003	0.0006	0.000615	1.03
1	±0.0001	0.0002	0.000225	1.13
1	±0.00003	0.00006	0.000070	1.17
2	±0.001	0.002	0.00186	0.93
2	±0.0003	0.0006	0.00053	0.89
2	±0.0001	0.0002	0.000207	1.03
2	±0.00003	0.00006	0.000062	1.03

The data in Table V indicate an observed maximum error of 17 percent and an average error of approximately 10 percent. Unit two was selected for subsequent use. The second technique utilized the existing peristaltic actuator to generate controlled motions on the millionth of an inch scale. These motions were measured simultaneously be the Brown & Sharpe electronic indicator and a laser-illuminated interferometer. The layout used is shown in Figures 23 and 24.

The laser used was a Perkin-Elmer Model 5000 with beam expander, operating at 6328Å. A sample of the data obtained is shown in Figure 25. Analyzing this data gives the following results:

Forward direction: five fringes on the interferometer equals 62.5×10^{-6} inches and measures 55.2×10^{-6} inches on the Brown & Sharpe indicator. Correction factor is 1.13

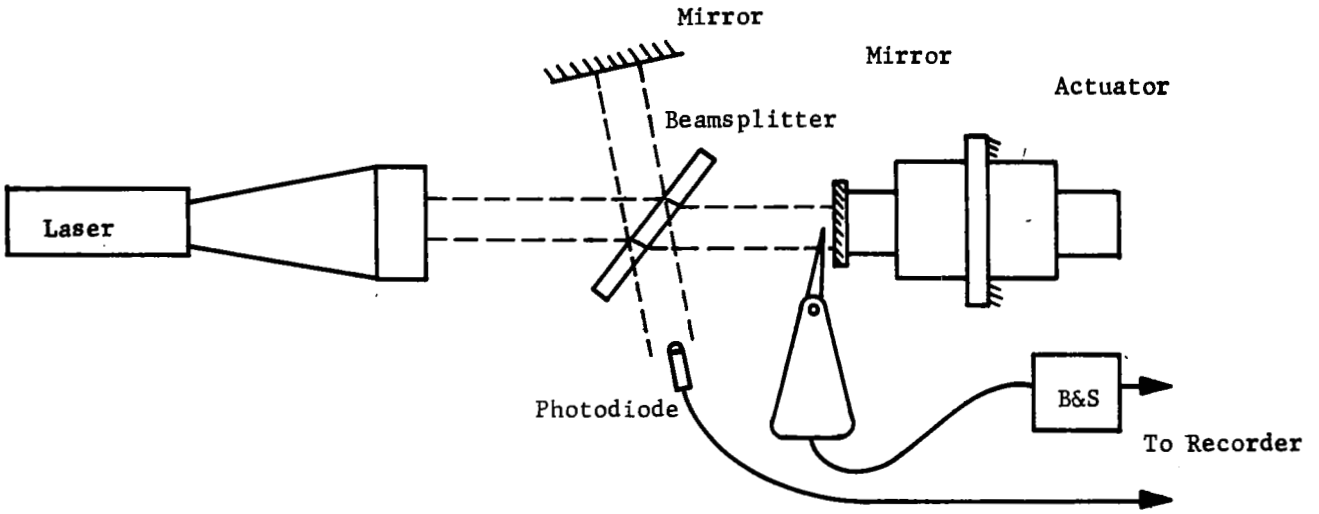

Figure 23. Actuator Calibration With Interferometer

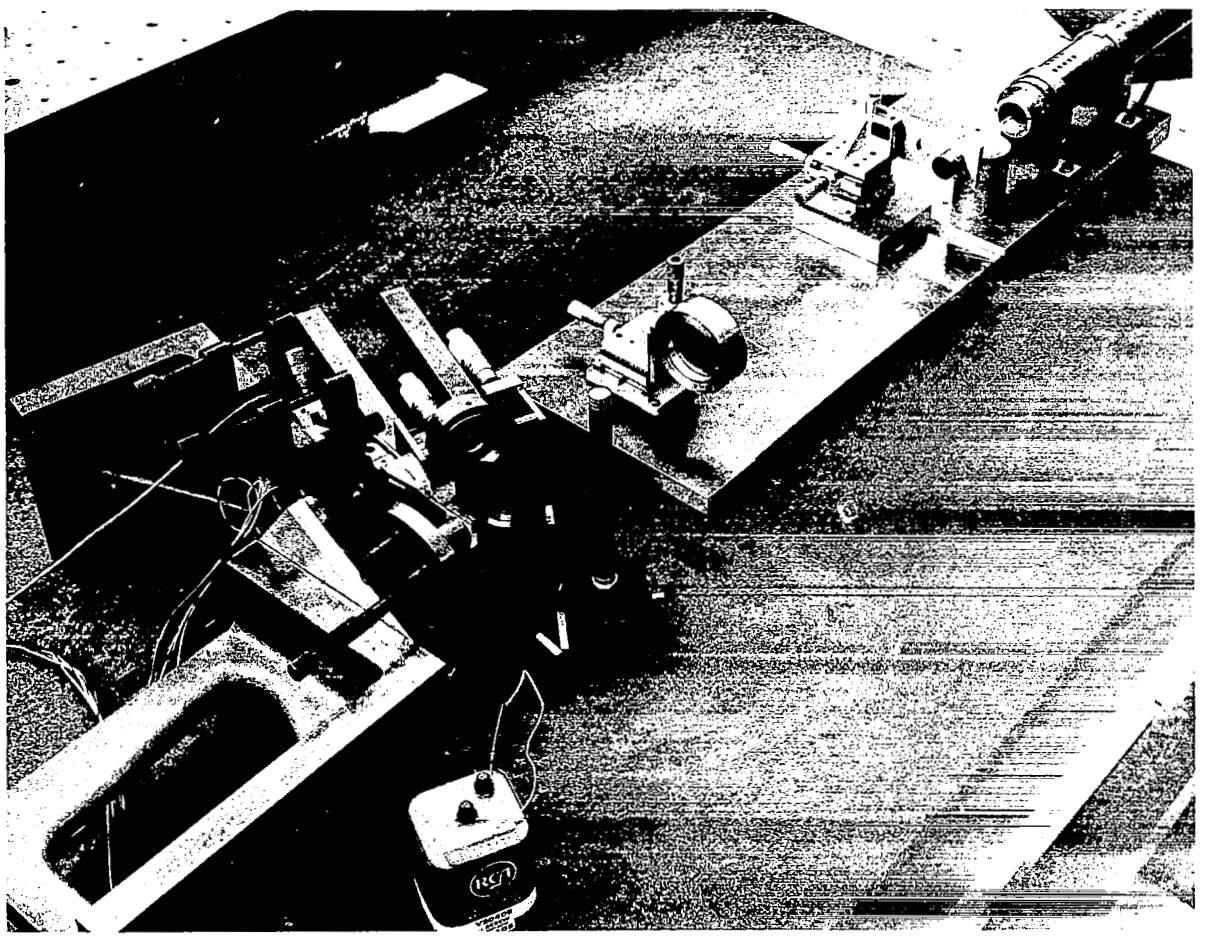

Figure 24. Photograph of Actuator Calibration Setup

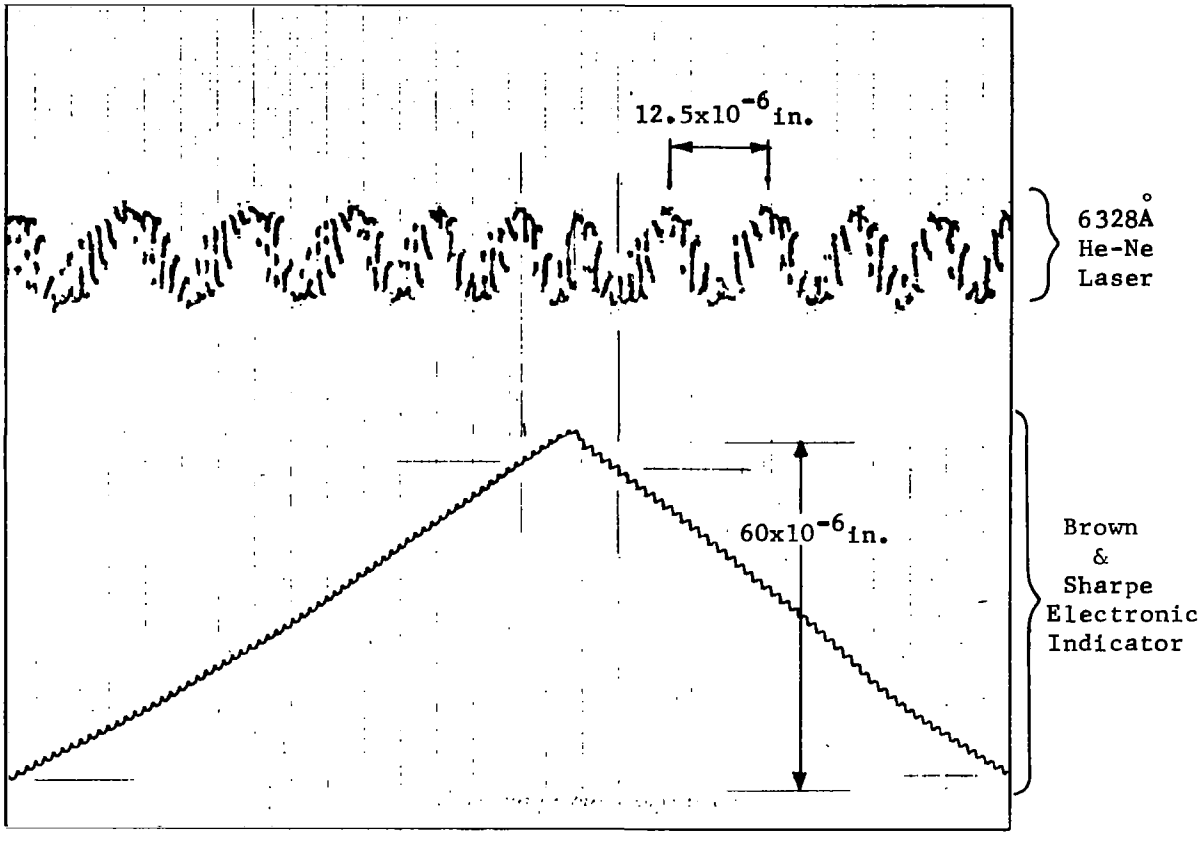

Figure 25. Calibration Data for the Brown & Sharpe Electronic Indicator

Reverse direction: four and one-half fringes on the interferometer equals 56.3 x 10^{-6} inches and measures 52.8 x 10^{-6} inches on the Brown & Sharpe indicator. Correction factor is 1.07.

Therefore the average error on the ±30 x 10^{-6} inch scale for the unit so tested is 10%.

Test Results

The following mounting configurations and measuring locations were utilized.

Configuration A

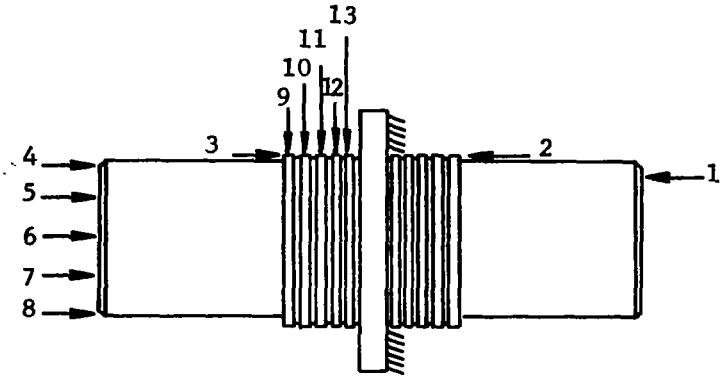

Configuration B

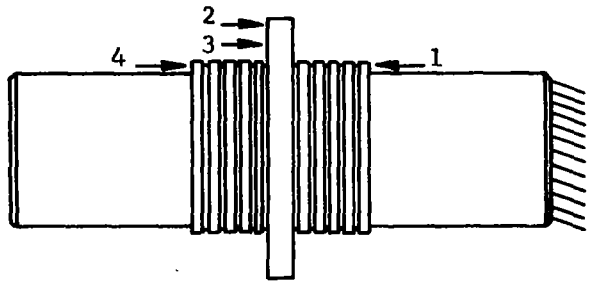

Configuration C

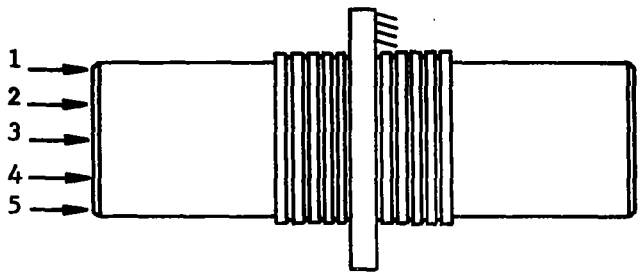

Actuator: Ten Electrode - Shallow Groove

Data: Motion as a Function of Measuring Location

Mounting Configuration: A

Data Point: Variable

Drive Voltage: 250 Volts

Bias Voltage: 0 Volts

Roll and Section Number: 0371 - 133 - Data Points 1 - 8
0371 - 134 - Data Points 9 - 13

Purpose: To Demonstrate Step Shape is not a Function of Measuring Position on Shaft

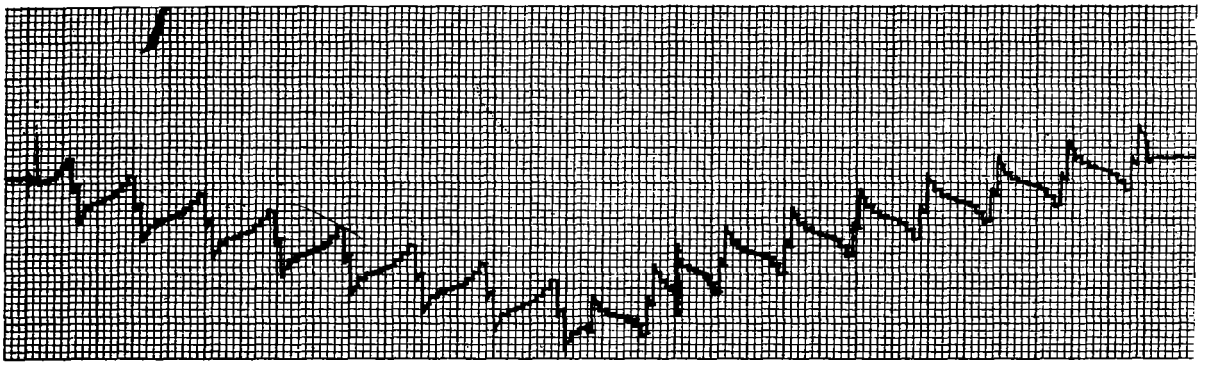

Data Point 1

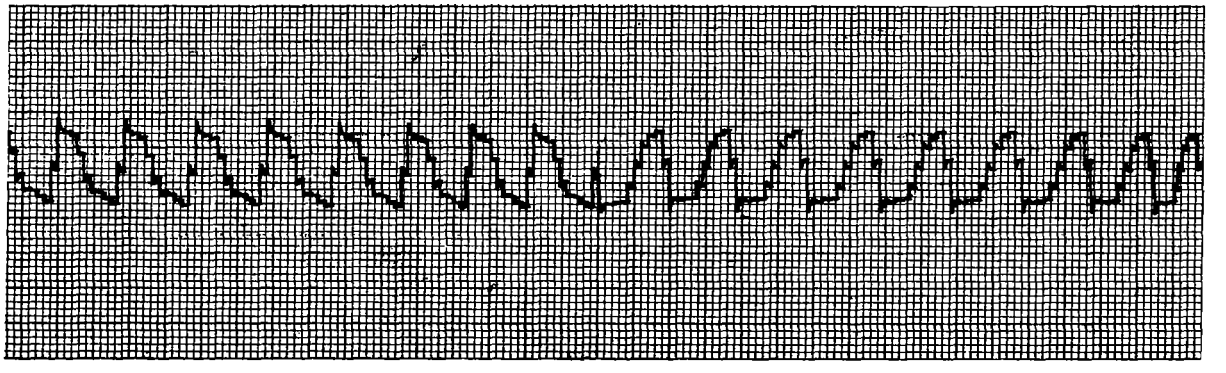

Data Point 2

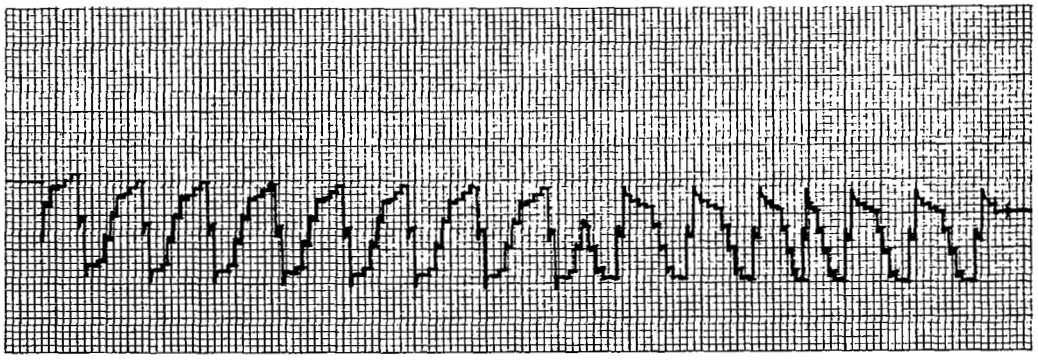

Data Point 3

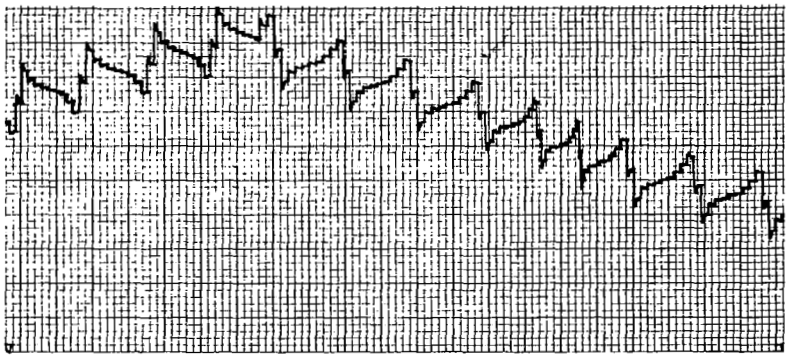

Data Point 4

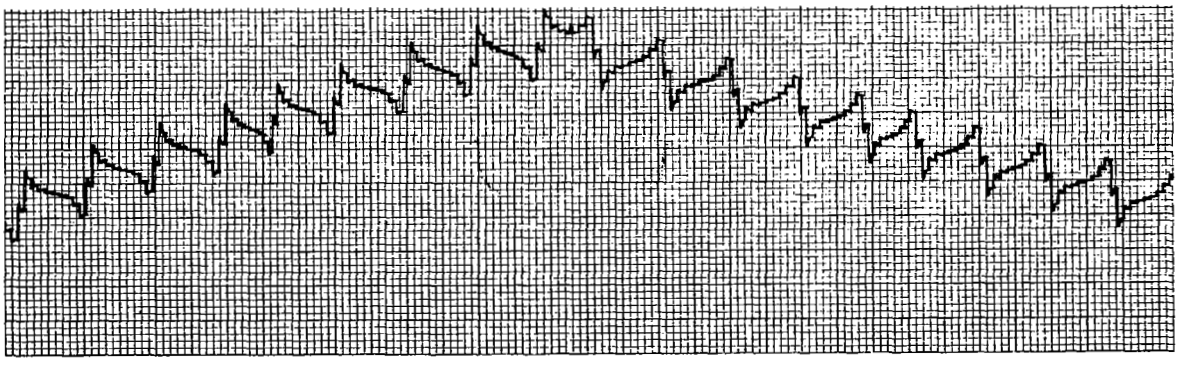

Data Point 5

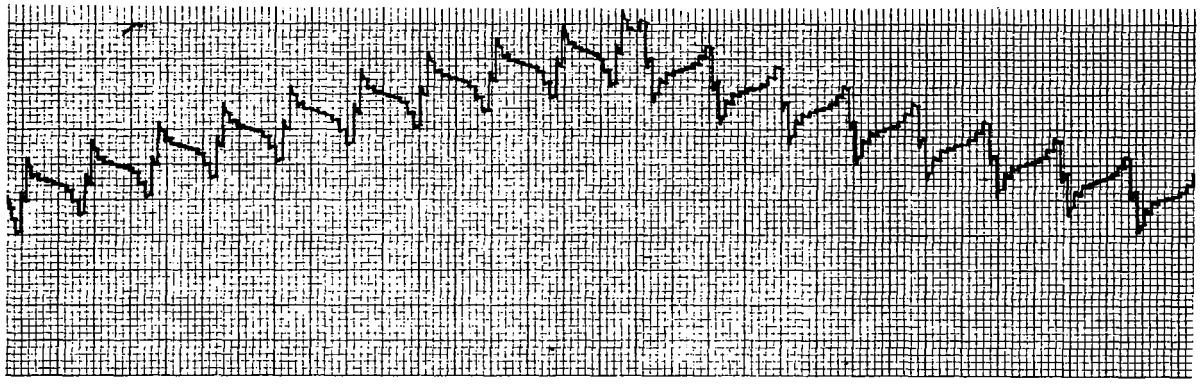

Data Point 6

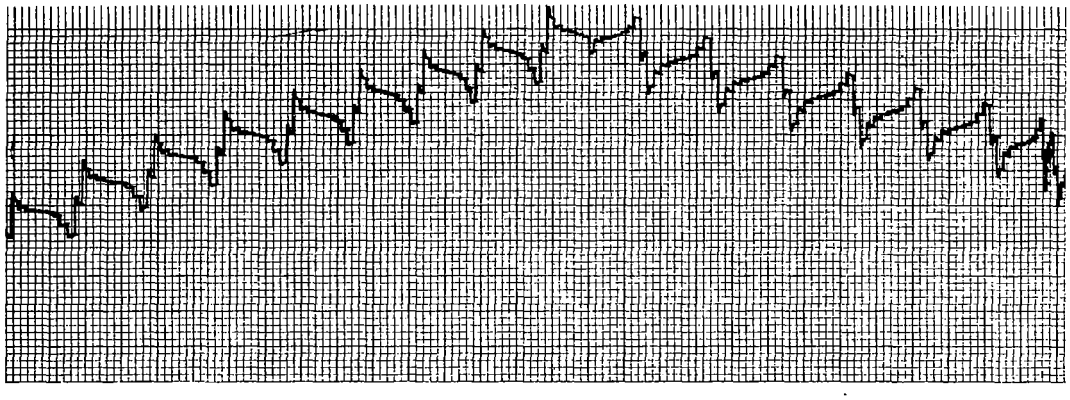

Data Point 7

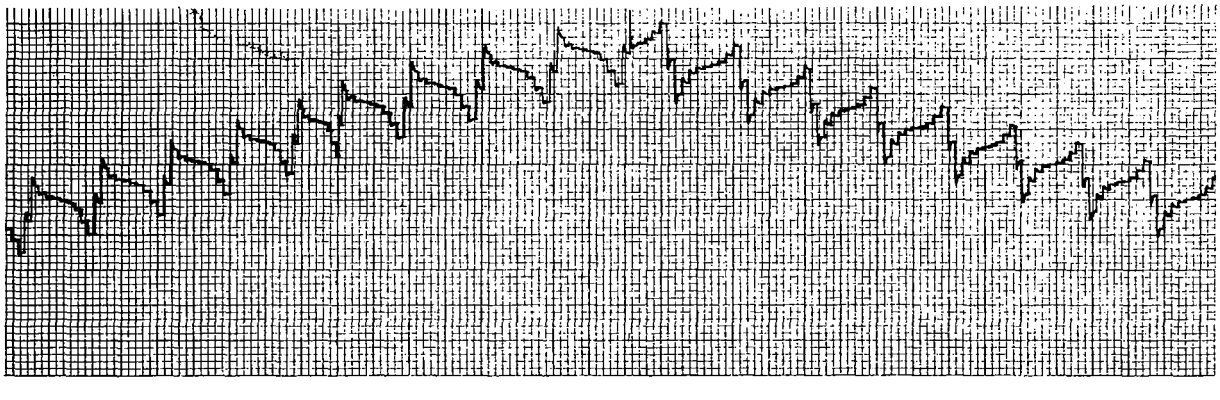

Data Point 8

For Data Points 9 Thru 13 Each Electrode is Individually Excited Three Times

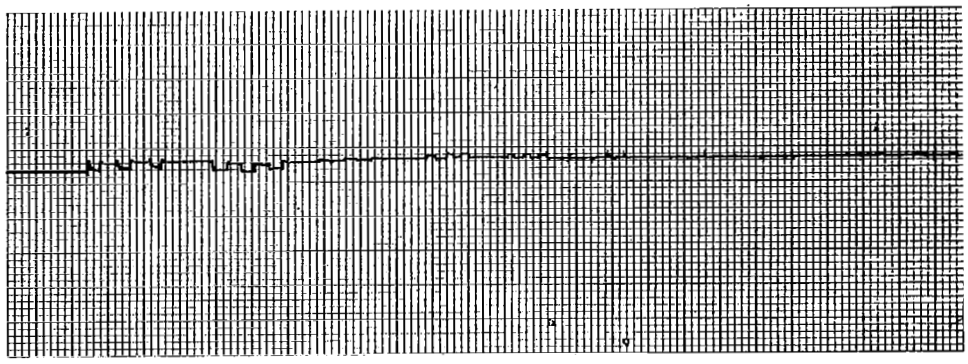

Data Point 9

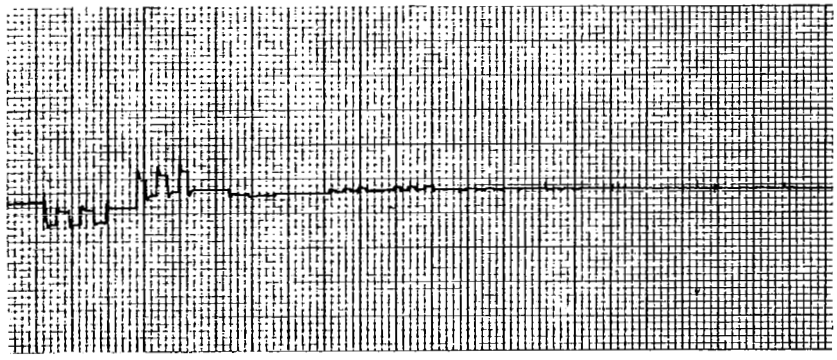

Data Point 10

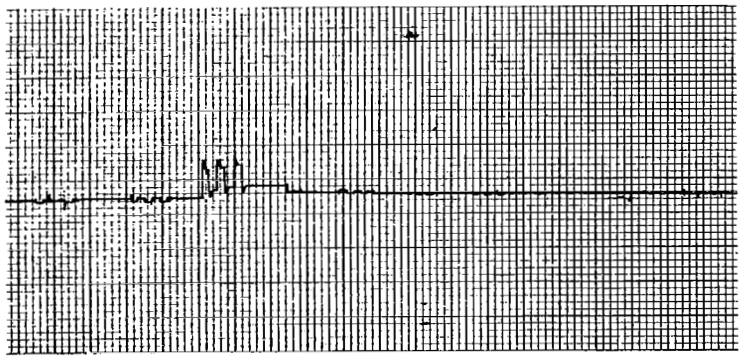

Data Point 11

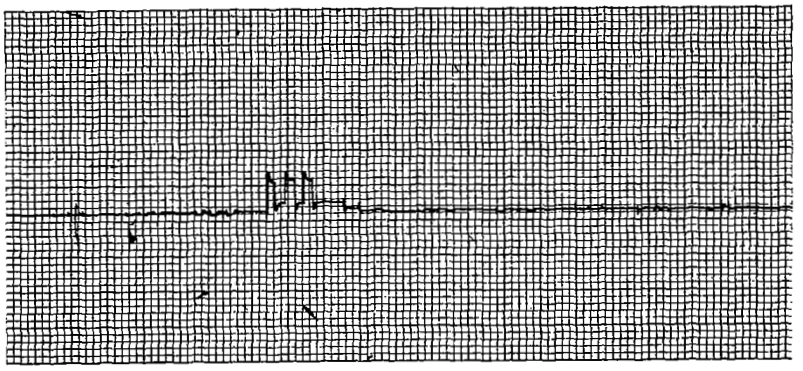

Data Point 12

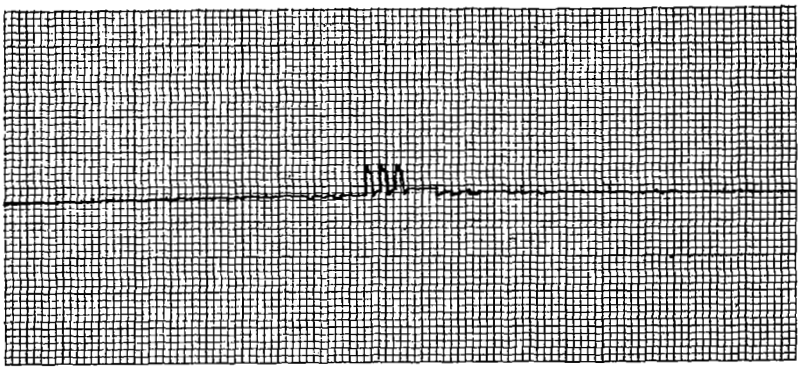

Data Point 13

Actuator: Ten Electrode - Shallow Groove

Data: Motion as a Function of Measuring Location

Mounting Configuration: B

Data Point: Variable

Drive Voltage: 250 Volts

Bias Voltage: 0 Volts

Roll and Section Number: 0371 - 136A - Data Points 1 to 4

Purpose: To Demonstrate that Interchaning Mounting Location does not effect the Actuator Output

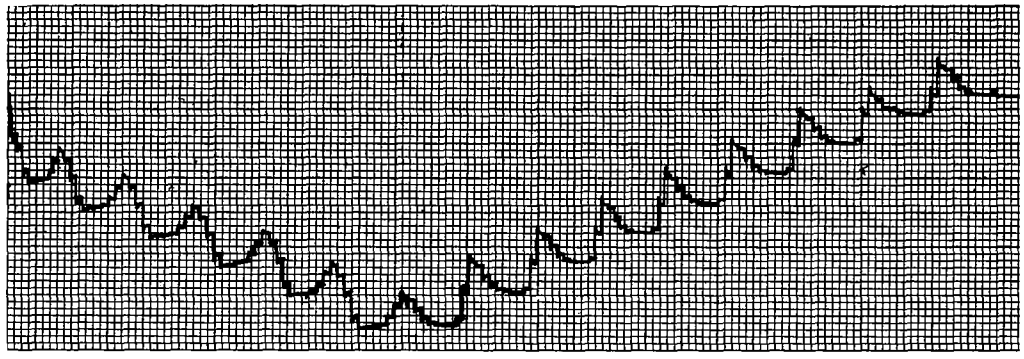

Data Point 1

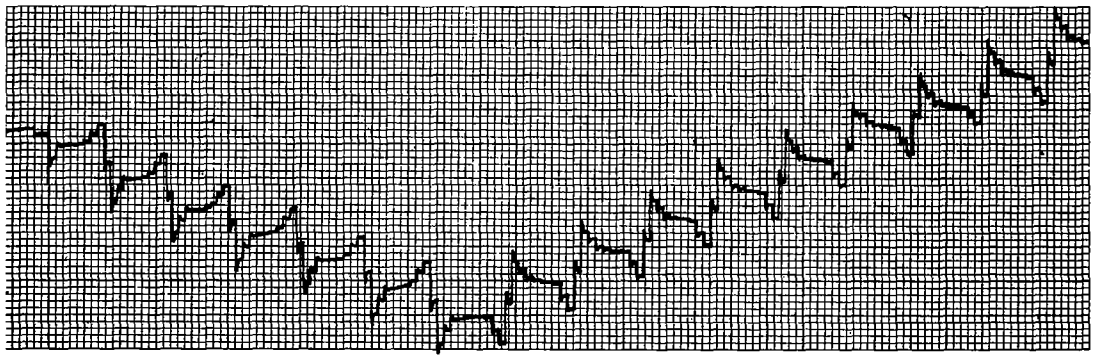

Data Point 2

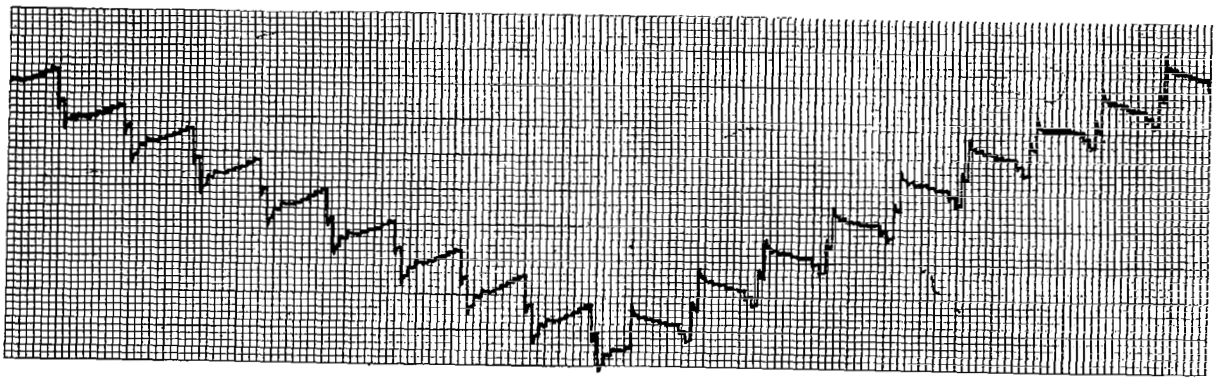

Data Point 3

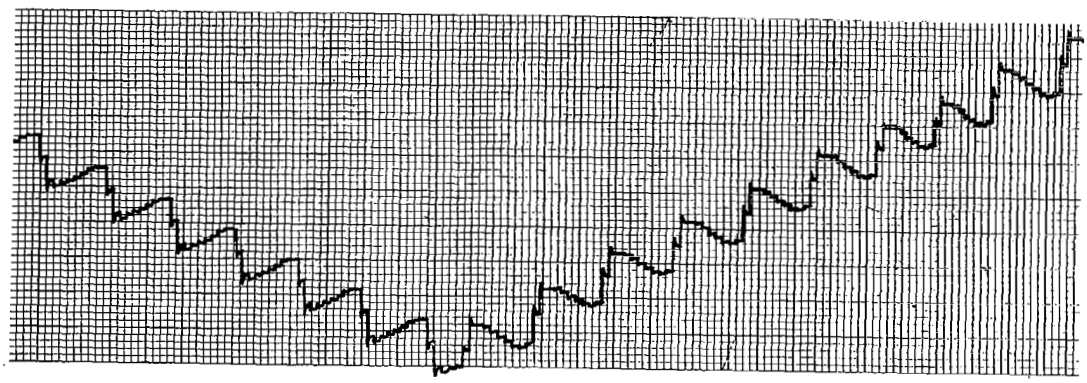

Data Point 4

Actuator: Ten Electrode - Shallow Groove

Data: Motion as a Function of Measuring Location

Mounting Configuration: C

Data Point: Variable

Drive Voltage: 250 Volts

Bias Voltage: 0 Volts

Roll and Section Number: 0371 - 137A - Data Points 1 to 5

Purpose: To Demonstrate the Necessity of Rigidly Mounting the Actuator

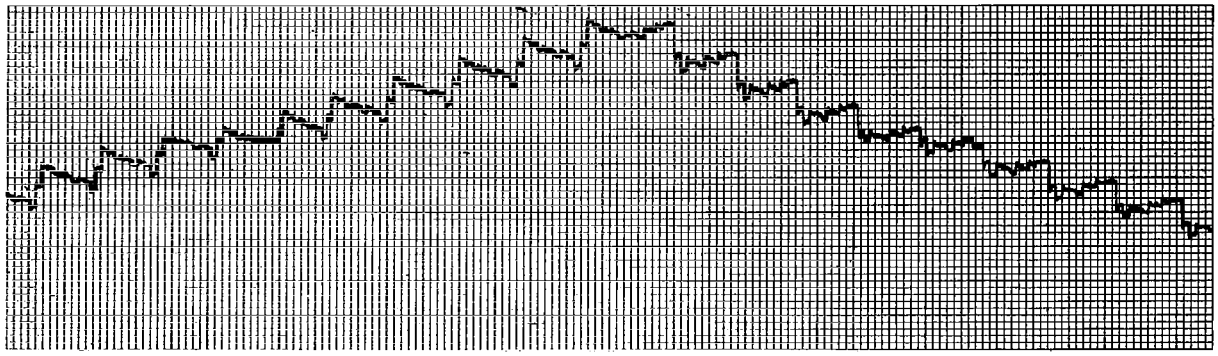

Data Point 1

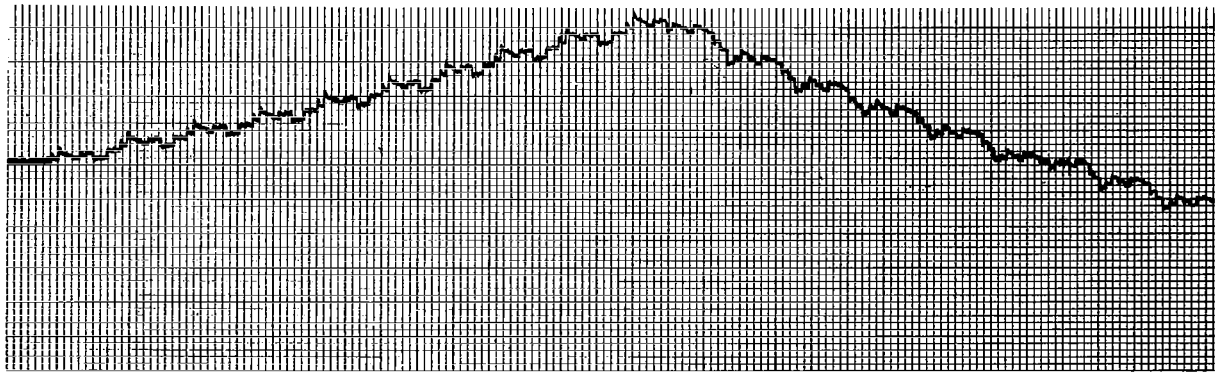

Data Point 2

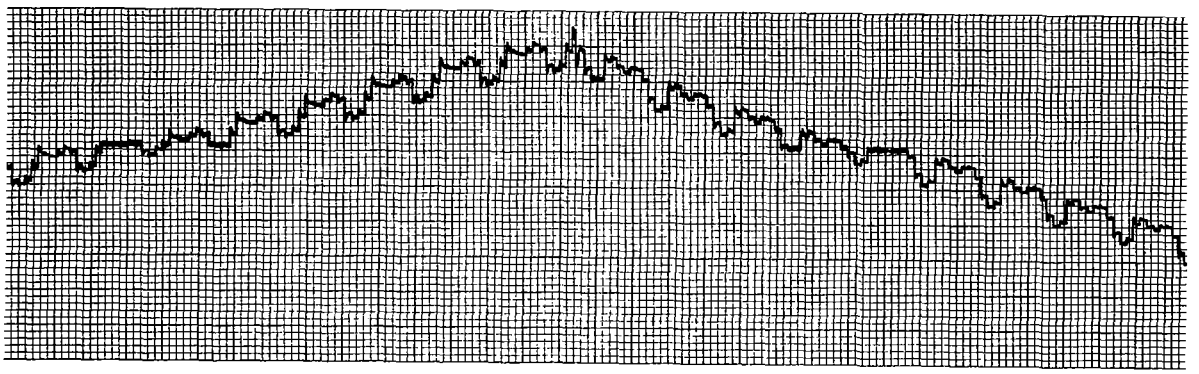

Data Point 3

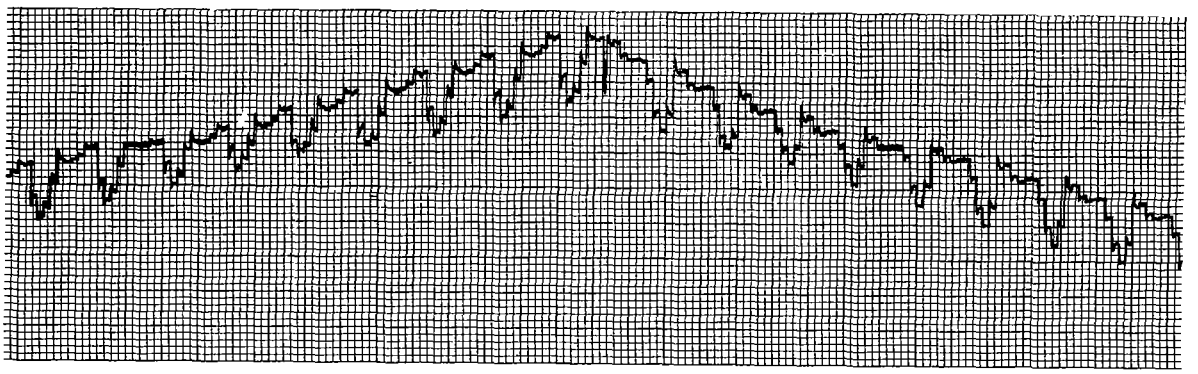

Data Point 4

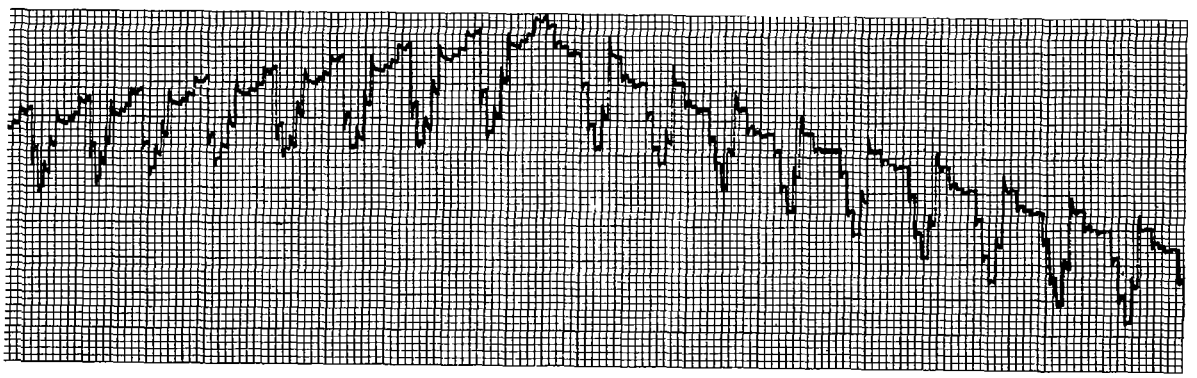

Data Point 5

Actuator: Ten Electrode - Shallow Groove

Data: Step Size as a Function of Drive Voltage

Mounting Configuration: A

Data Point: 6

Drive Voltage: Variable

Bias Voltage: 0 Volts

Roll and Section Number: 0371-139

Purpose: To Demonstrate that Decreasing Voltage Decreases Actuator Step Size

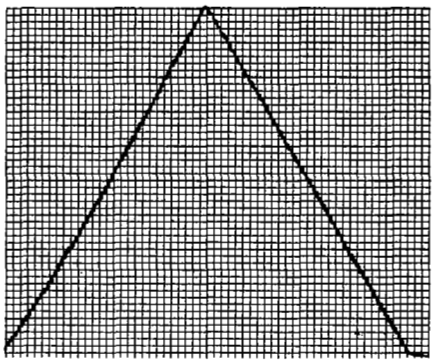

Drive Voltage: 300 Volts

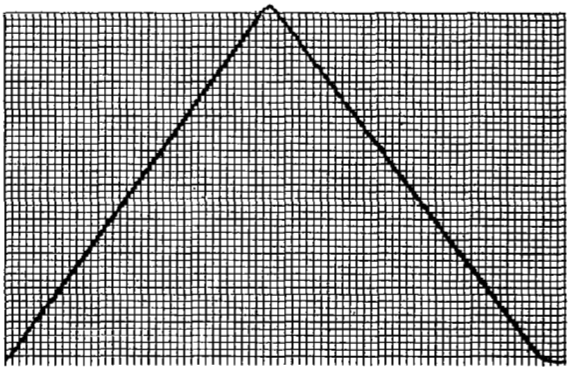

Drive Voltage: 275 Volts

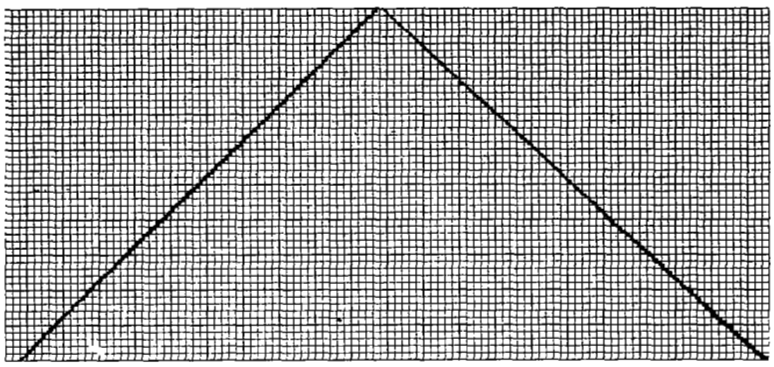

Drive Voltage: 250 Volts

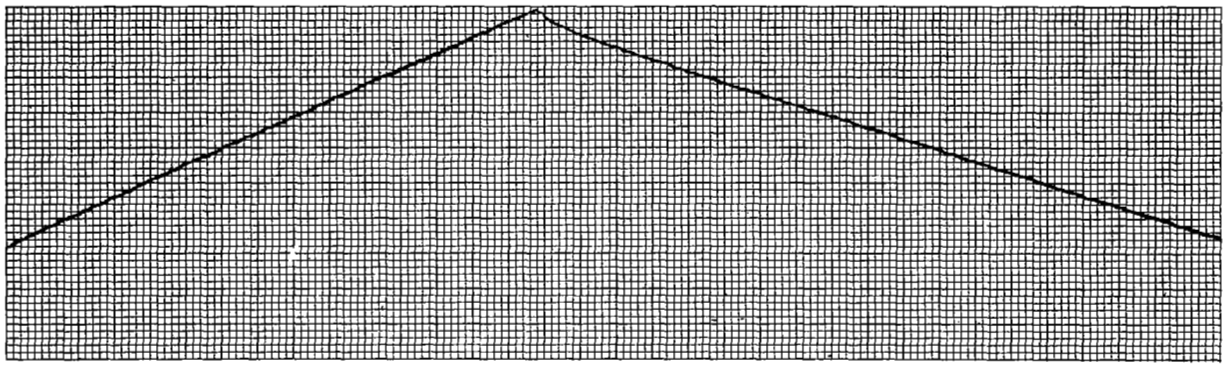

Drive Voltage: 225 Volts

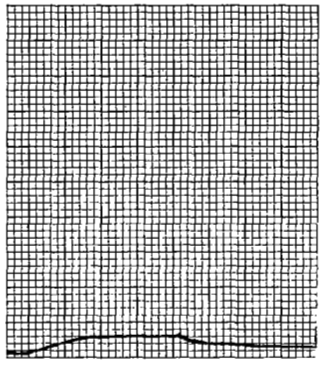

Drive Voltage: 200 Volts

Actuator: Ten Electrode - Shallow Groove

Data: Step Size as a Function of Bias Voltage { - = Increase Interference; + = Decrease Interference }

Mounting Configuration: A

Data Point: 6

Drive Voltage: 300 Volts

Bias Voltage: Variable

Roll and Section Number: 0371-139

Purpose: To Demonstrate that the Interference Fit Affects Actuator Step Size

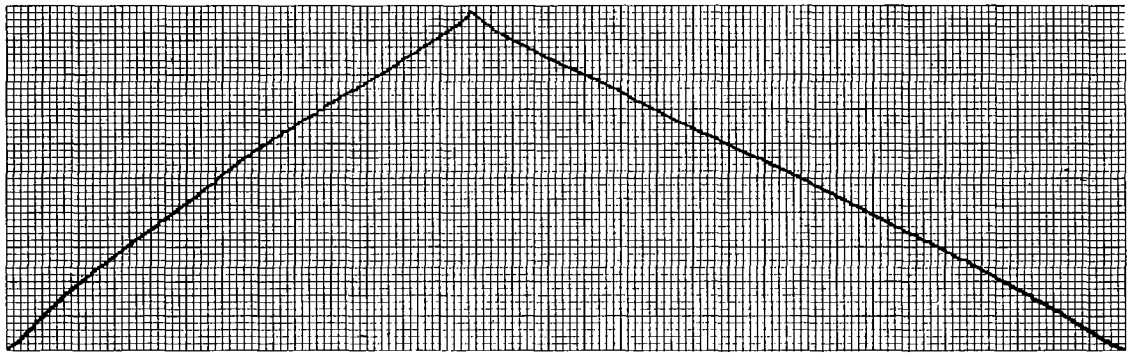

Bias Voltage: -400 Volts

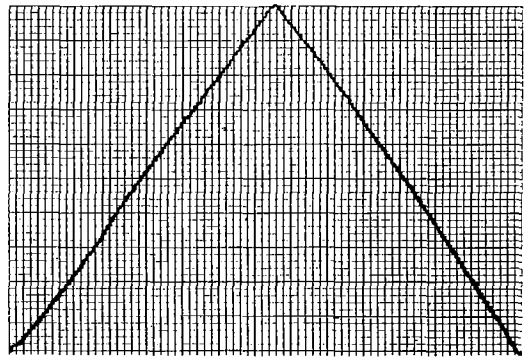

Bias Voltage: -200 Volts

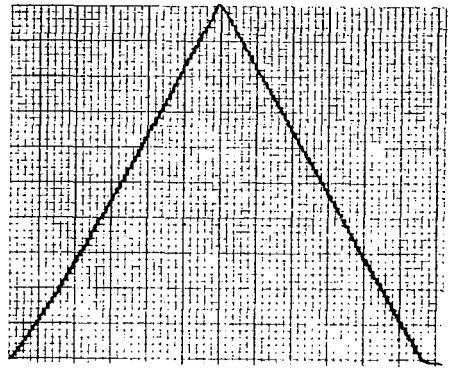

Bias Voltage: 0 Volts

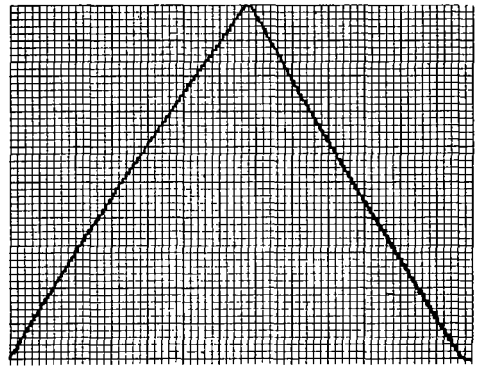

Bias Voltage: +200 Volts

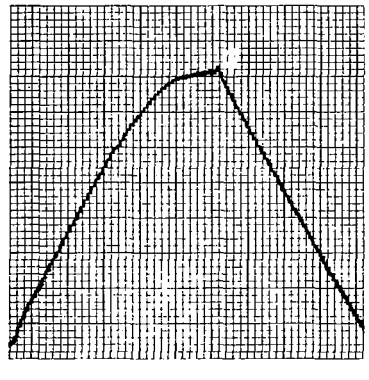

Bias Voltage: +400 Volts

Actuator: Ten Electrode - Shallow Groove

Data: Step Size as a Function of Axial Load

Mounting Configuration: A

Data Point: 6

Drive Voltage: 300 Volts

Bias Voltage: -100 Volts

Roll and Section Number: 0371 - 140 - Load Up To 688 Grams
0115 - 131 - Load 800 and 1,000 Grams

Purpose: To Demonstrate that the Actuator Could Work Against at Least a 1000-gram Load

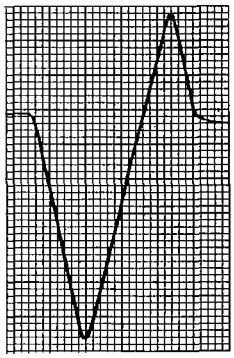

Axial Load: 0 Grams

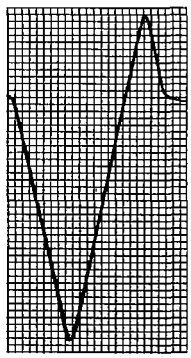

Axial Load: 115 Grams

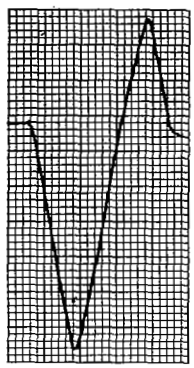

Axial Load: 230 Grams

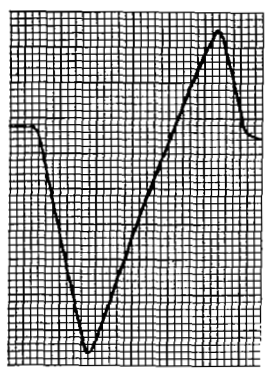

Axial Load: 345 Grams

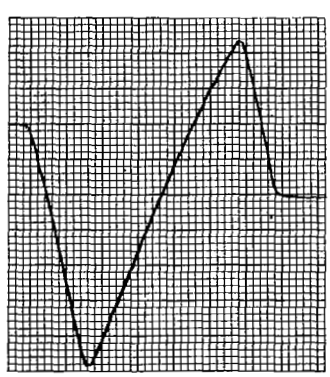

Axial Load: 458 Grams

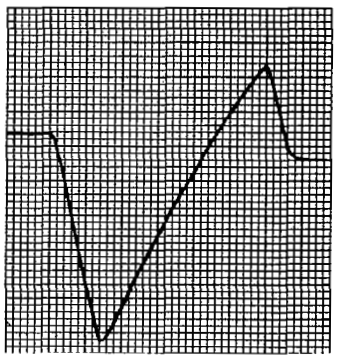

Axial Load: 573 Grams

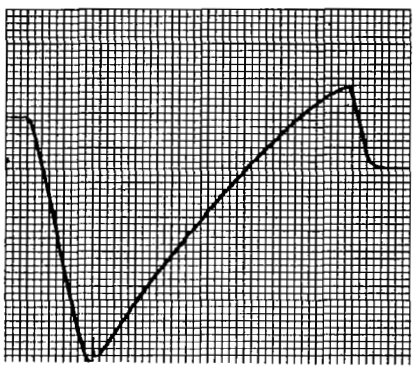

Axial Load: 688 Grams

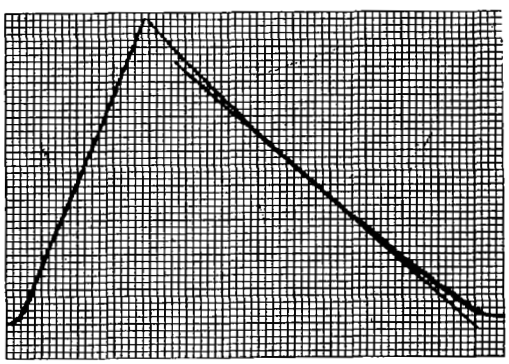

Axial Load: 800 Grams

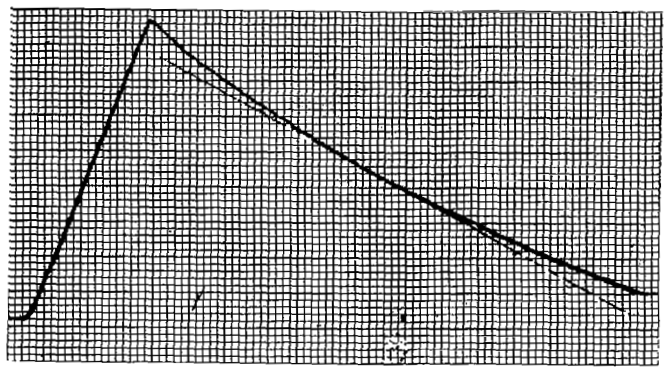

Axial Load: 1000 Grams

Actuator: Ten Electrode - Shallow Groove

Data: Step Size as a Function of Transverse Load

Mounting Configuration: A

Data Point: 6

Drive Voltage: 250 Volts

Bias Voltage: 0 Volts

Roll and Section Number: 0371-141

Purpose: To Demonstrate that Loads up to 1000 grams Applied Perpendicularly to the Direction of Travel Have Negligible Effect on Performance.

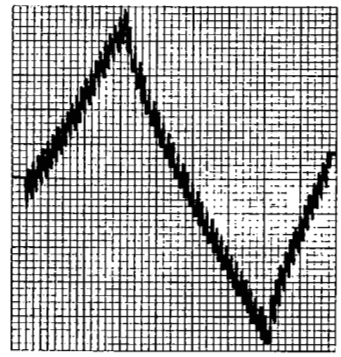

Transverse Load: 0 Grams

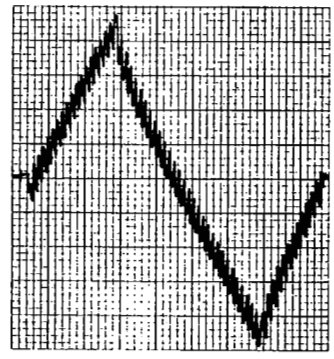

Transverse Load: 250 Grams

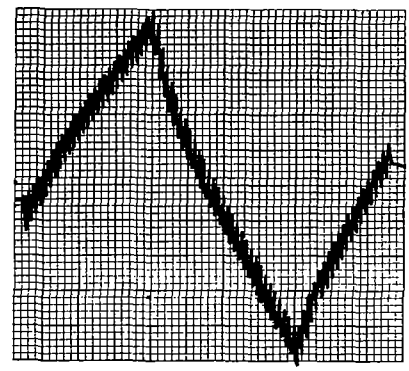

Transverse Load: 500 Grams

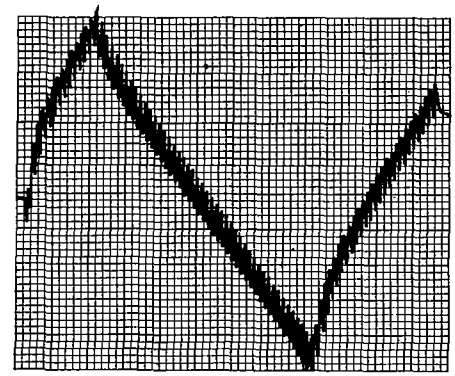

Transverse Load: 750 Grams

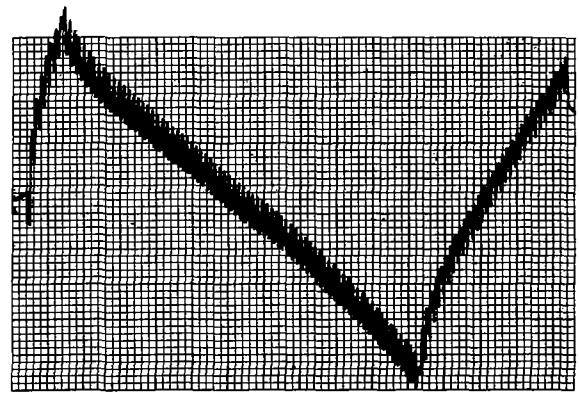

Transverse Load: 1,000 Grams

Actuator: Ten Electrode - Shallow Groove

Data: Step Size as a Function of Stepping Rate

Mounting Configuration: A

Data Point: 6

Drive Voltage: +300 Volts

Bias Voltage: +100 Volts

Roll and Section Number: 0371-125

Purpose: To Demsonstrate the Correlation Between Frequency of Applied Voltage (Step Rate) and Step Size

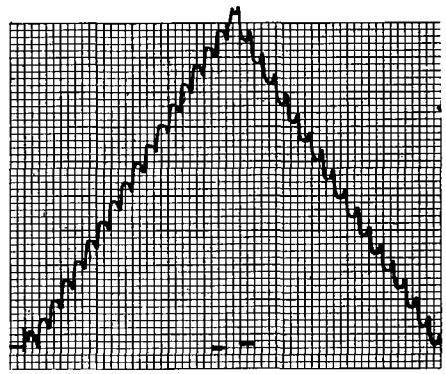

Step Rate: 0.6 Steps/Second

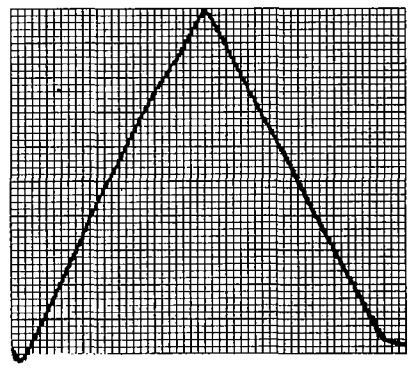

Step Rate: 2 Steps/Second

Actuator: Ten Electrode - Deep Groove

Data: Motion as a Function of Measuring Location

Mounting Configuration: B

Data Point: Variable

Drive Voltage: 400 Volts

Bias Voltage: 0 Volts

Roll and Section Number: 0371-144

Purpose: To Demonstrate the Step Shape of the Deep Groove Configuration

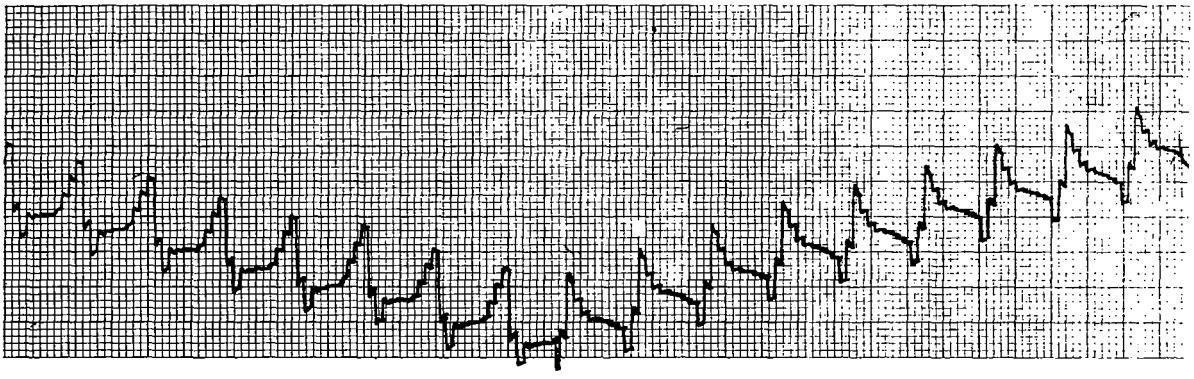

Data Point 1

Data Point 2

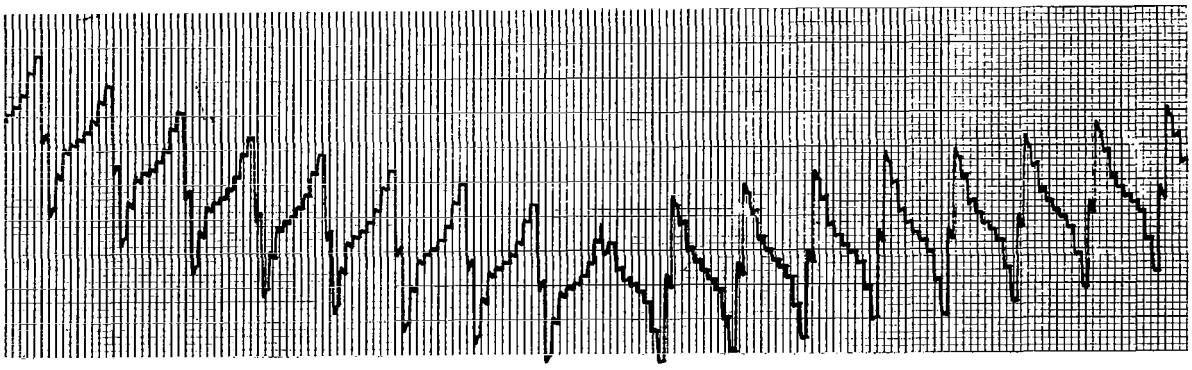

Data Point 3

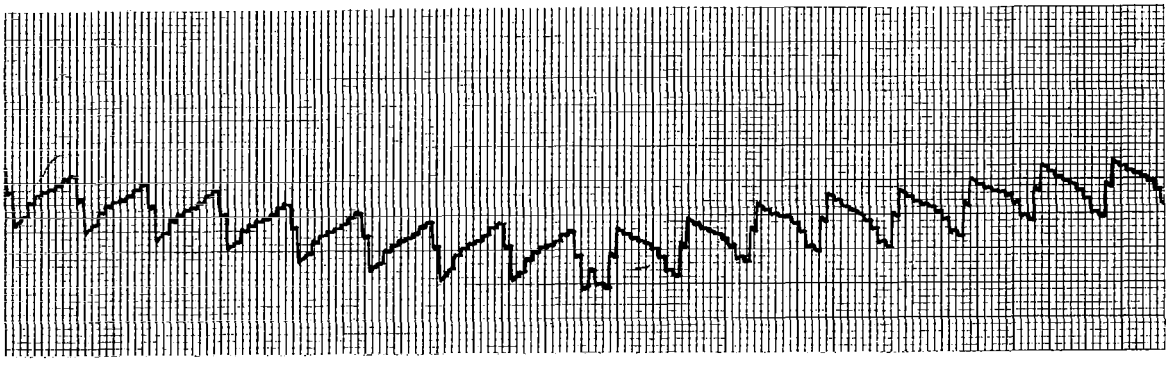

Data Point 4

Actuator: Ten Electrode - Deep Groove

Data: Motion as a Function of Measuring Location

Mounting Configuration: C

Data Point: Variable

Drive Voltage: 400 Volts

Bias Voltage: 0 Volts

Roll and Section Number: 0371 - 145A

Purpose: To Demonstrate the Necessity of Rigidly Mounting the Actuator

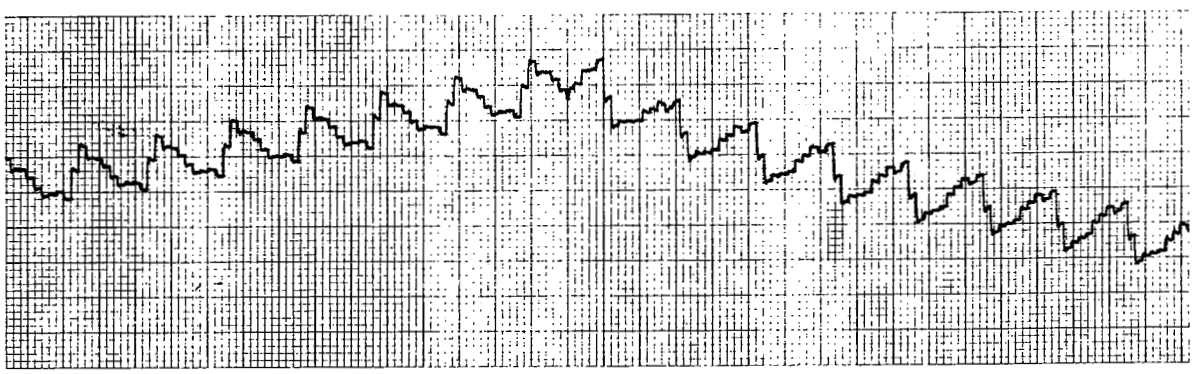

Data Point 1

Data Point 2

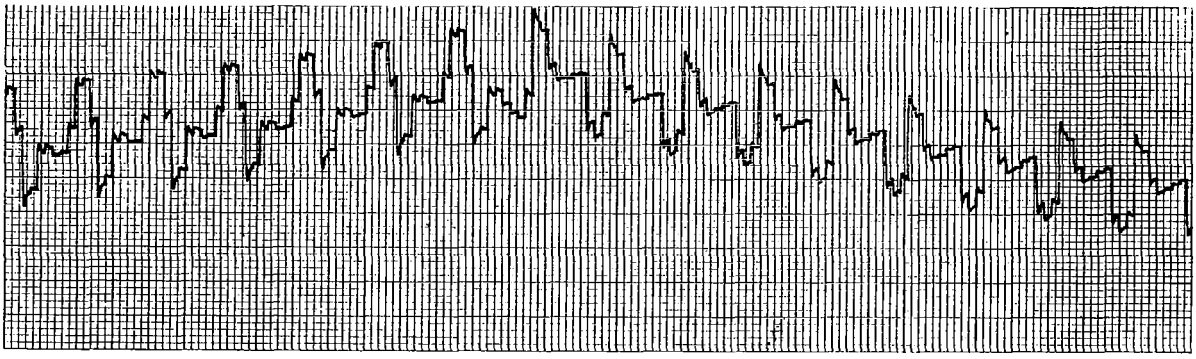

Data Point 3

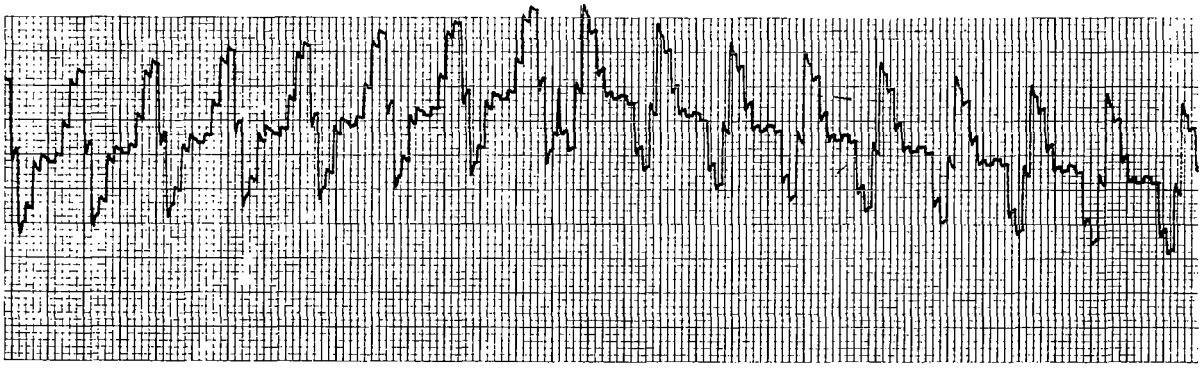

Data Point 4

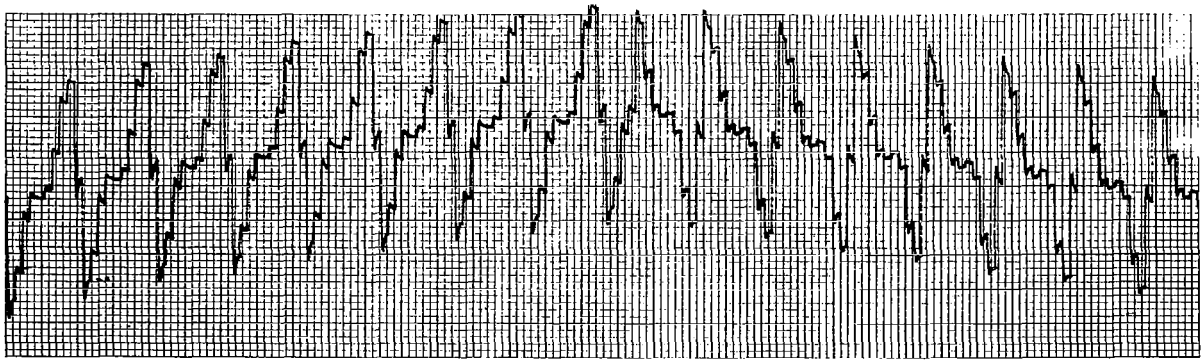

Data Point 5

Actuator: Ten Electrode - Deep Groove

Data: Step Size as a Function of Drive Voltage

Mounting Configuration: B

Data Point: 4

Drive Voltage: Variable

Bias Voltage: 0 Volts

Roll and Section Number: 0371-144

Purpose: To Demonstrate How the Step Size Decrease with Decreasing Voltage

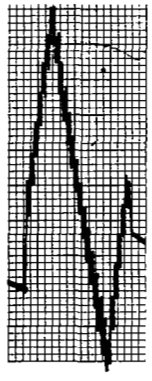

Drive Voltage: 460 Volts

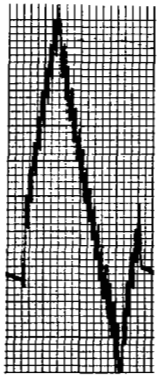

Drive Voltage: 440 Volts

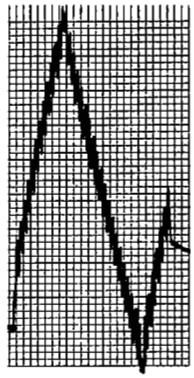

Drive Voltage: 420 Volts

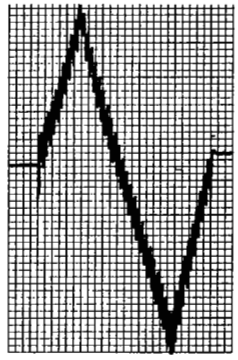

Drive Voltage: 400 Volts

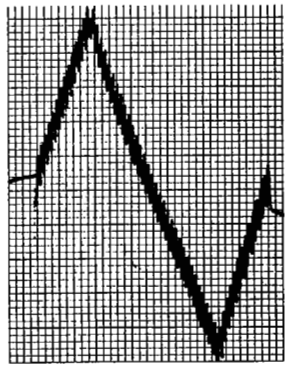

Drive Voltage: 380 Volts

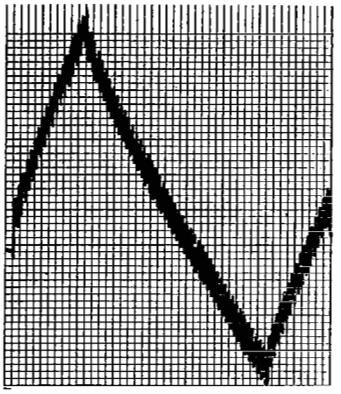

Drive Voltage: 360 Volts

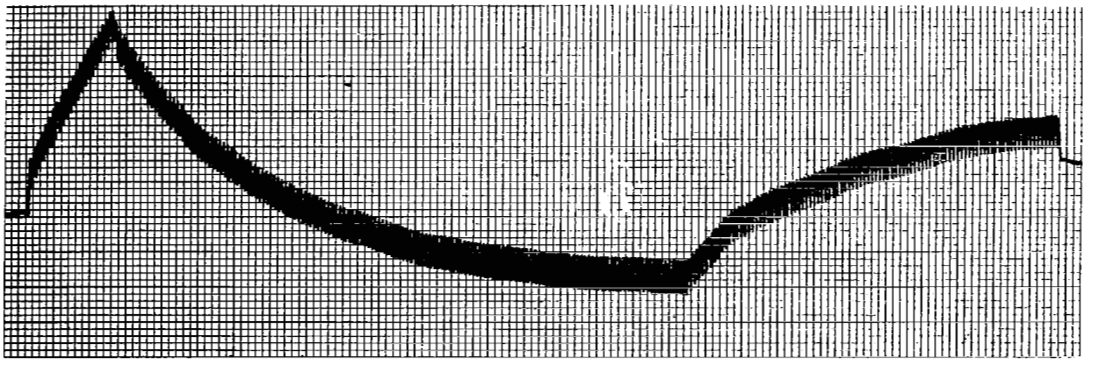

Drive Voltage: 340 Volts

Actuator: Sixteen Electrode - Shallow Groove

Data: Step Size as a Function of Bias Voltage

Mounting Configuration: B

Data Point: 4

Drive Voltage: 400 volts

Bias Voltage: Variable

Roll and Section Number: 2294 - 104 - Data Points 1 - 5

Purpose: To Demonstrate Actuator Motion as a Function of Bias Voltage Noting that Reducing the Interference Fit Changes Actuator Motion

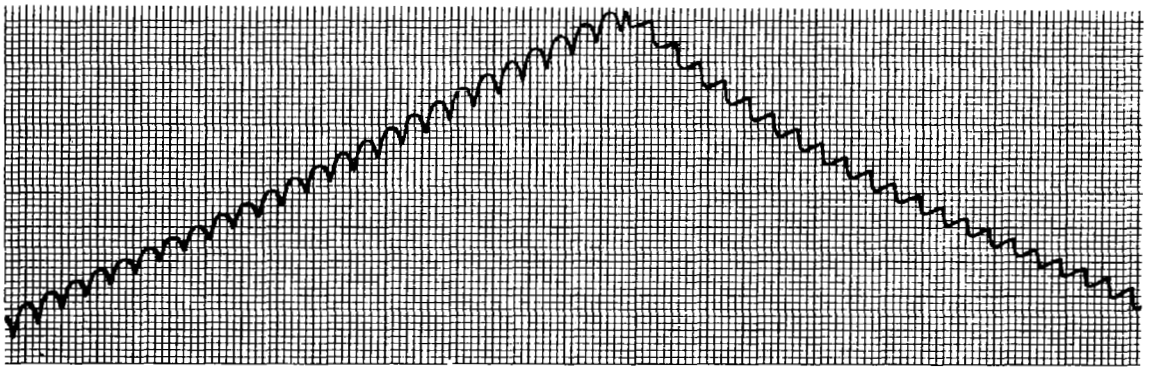

Bias Voltage: -250 Volts

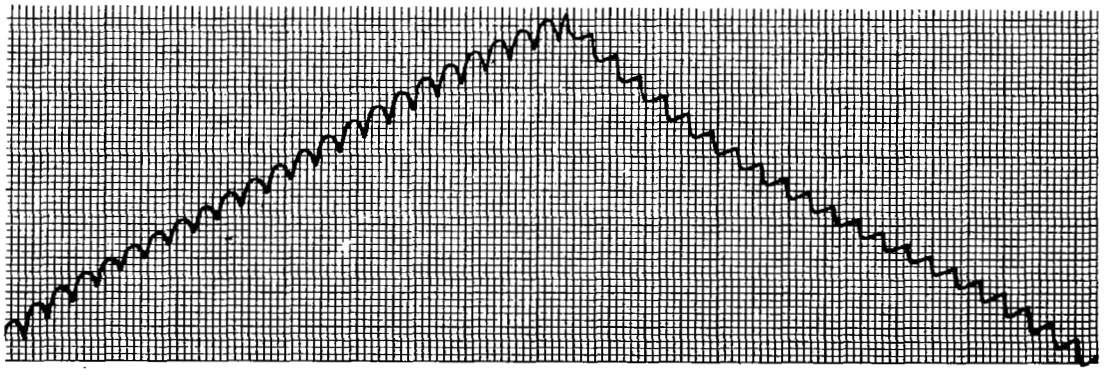

Bias Voltage: -200 Volts

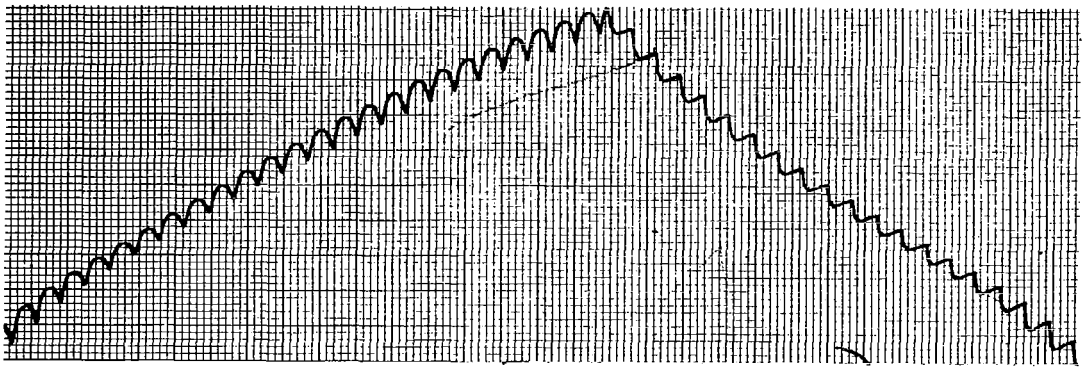

Bias Voltage: -100 Volts

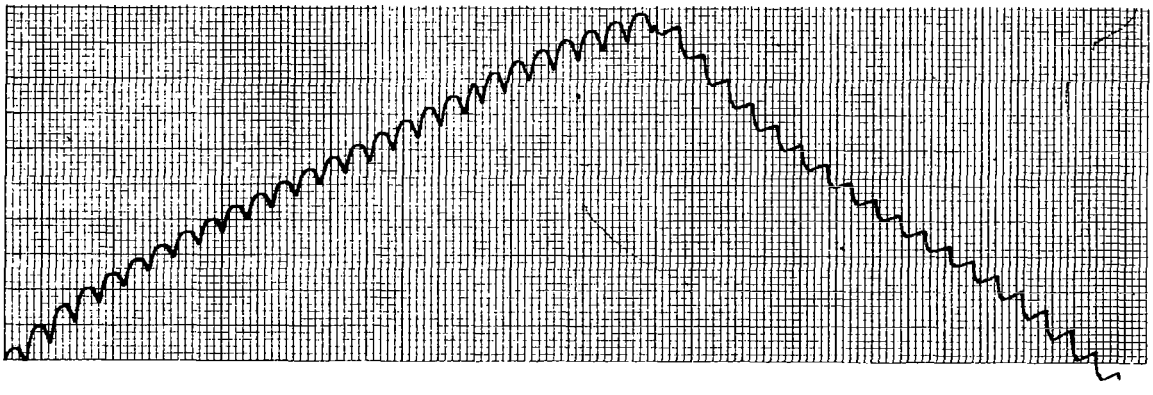

Bias Voltage: 0 Volts

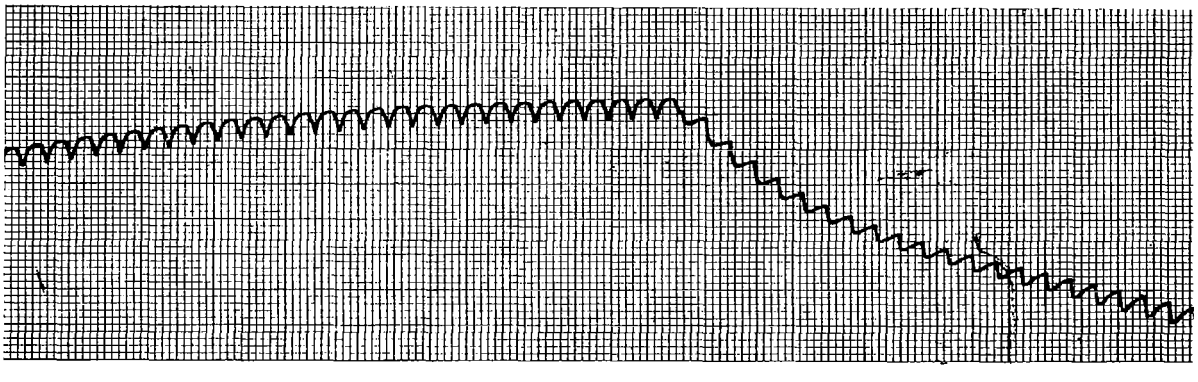

Bias Voltage: +100 Volts

Actuator: Sixteen Electrode - Shallow Groove
Data: Step Size as a Function of Drive Voltage
Mounting Configuration: B
Data Point: 4
Drive Voltage: Variable
Bias Voltage: -200 Volts
Roll and Section Number: 2294 - 105A
Purpose: To Demonstrate Actuator Motion
at Various Voltage Levels

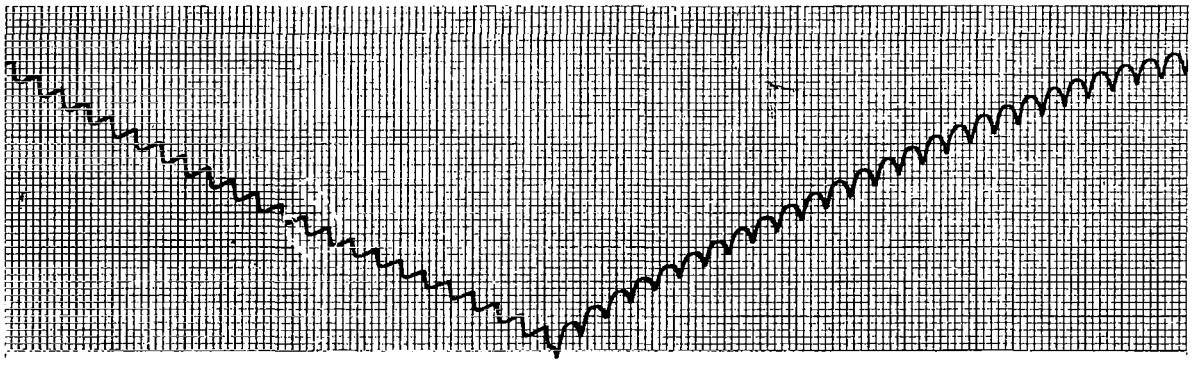

Drive Voltage: 400 Volts

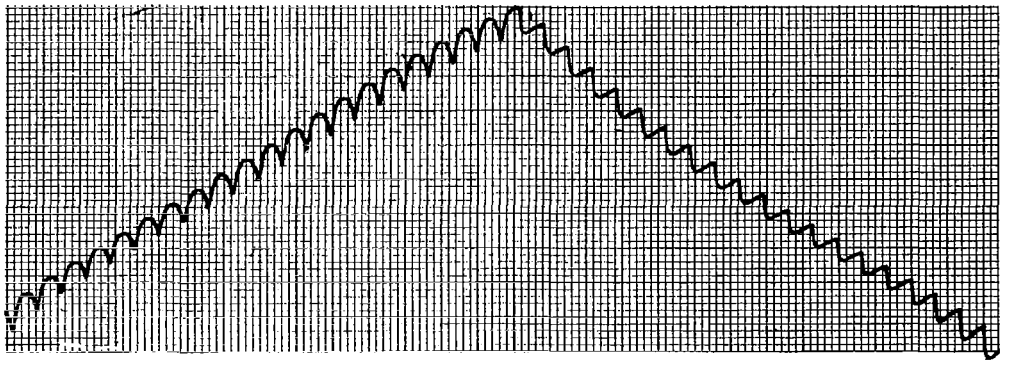

Drive Voltage: 450 Volts

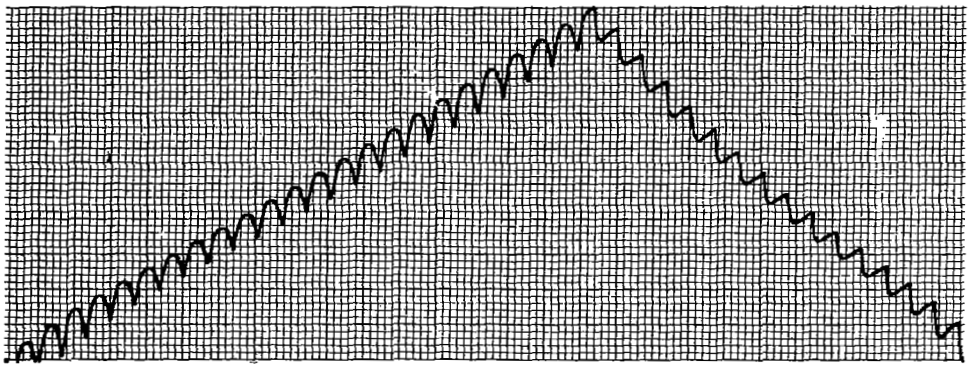

Drive Voltage: 500 Volts

Actuator: Sixteen Electrode - Shallow Groove

Data: Step Size as a Function of Stepping Rate

Mounting Configuration: B

Data Point: 4

Drive Voltage: 450 Volts

Bias Voltage: 200 Volts

Roll and Section Number: 2294 - 105B - Data Points 1 - 4

Purpose: To Demonstrate that Step Size Decreases as Stepping Rate Increases

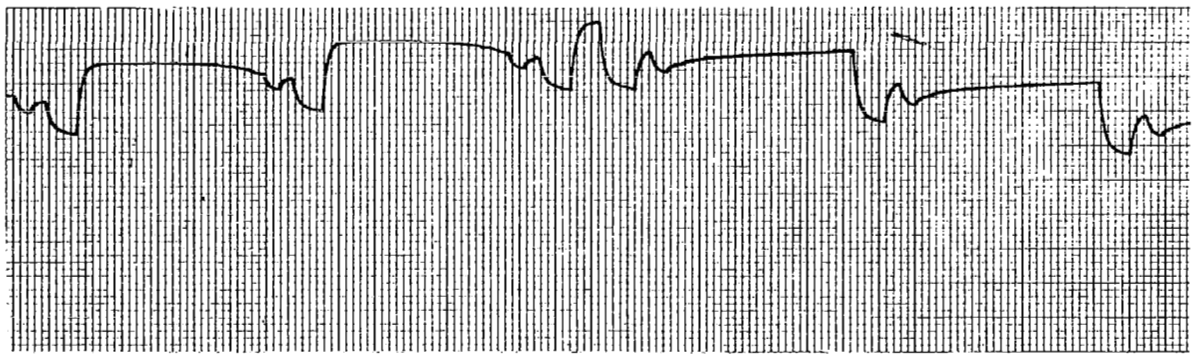

Step Rate: 0.5 step/second

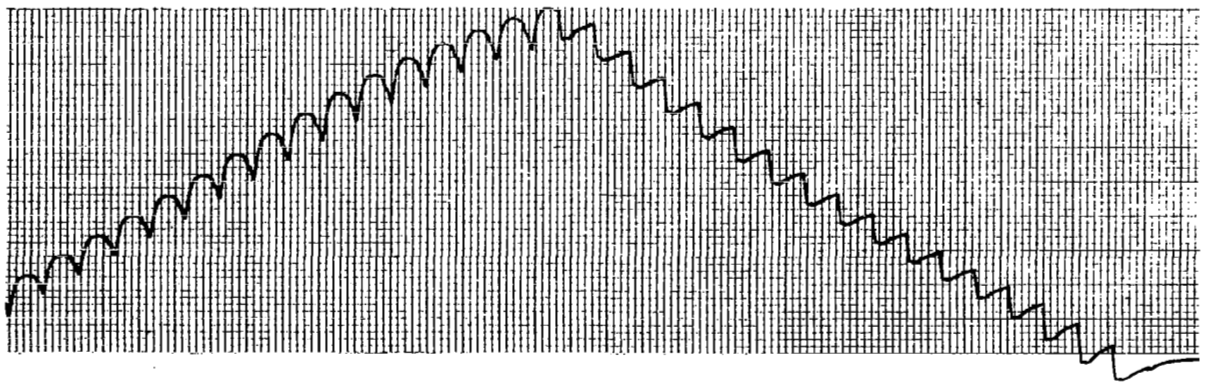

Step Rate: 1 step/second

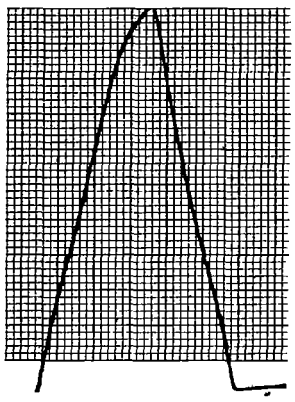

Step Rate: 10 steps/sec

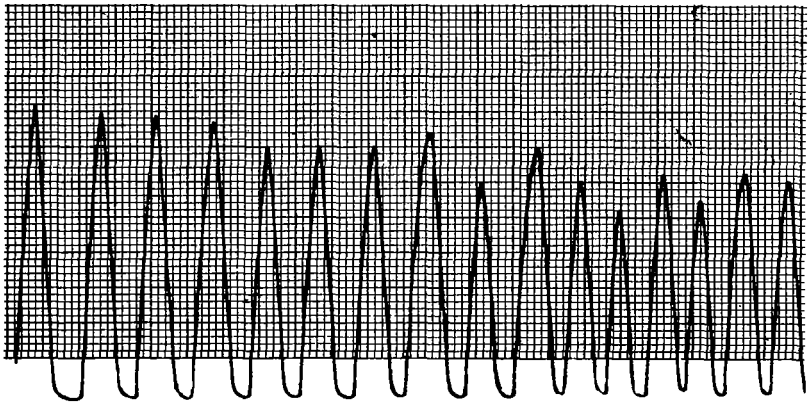

Step Rate: 100 steps/sec

CONCLUSIONS

The Perkin-Elmer Corporation has successfully advanced the state of actuator technology and, as a result, produced working peristaltic microinch actuators. The actuators consistently work against a 1000-gram load in steps of $\lambda/50$ and, under no load, in steps of $\lambda/25$. The other various design goals such as frequency response, no-voltage load holding capability, reversible motion, low power consumption, and the ability to operate in a space environment have all been achieved.

The analytical work performed closely represents the experimental results. The progress made so far has shown that, even though a good level of success has been achieved, there still remain some unanswered questions.

Questions concerning the basic nature of the device are very pertinent. Variation in items such as surface finish, interference fit, and step shape are of concern. How do these parameters, varied singularly or in combination, affect overall performance of the actuator?

Questions concerning step size are of importance. Optical systems operating in the ultraviolet region require an actuator stepping performance of at least five times better than that already achieved. At the present time, it is felt that sufficient questions exist to warrant further study on advanced actuators.

REFERENCES

1. Barton, M.V.: "The Circular Cylinder with a Band of Uniform Pressure on a Finite Length of the Surface", J. Appl. Mech., Trans.ASME, vol. 8, 1941, p. A-97.

2. Rankin, A.W.: "Shrink Fit Stresses and Deformations", J. Appl. Mech., Trans. ASME, vol. 11, 1944, p. A-77.

3. Jahnke, Eugene, and Emde, Fritz: Tables of Functions, Dover Publications, Inc., S 133.

4. Timoshenko, S., and Woinowsky-Krieger, S: Theory of Plates and Shells, Second ed., McGraw-Hill Book Company, 1959, pp. 466-468.

5. Gulton Industries, Inc.: Glennite® Piezoceramics, Microceramics Division, Metuchen, N.J. 08840, p. 22.

6. Clevit Corporation: Piezoelectric Technology, Data for Designers, Piezoelectric Division, 232 Forbes Road, Bedford, Ohio, p. 33.

APPENDIX A

ADVANCED ACTUATOR ELECTRONIC DRIVE SYSTEM OPERATIONS PROCEDURE

The actuator electronic drive system is contained in a single package requiring only the addition of a high voltage power supply for operation. The system acts as an electronic switch between the high voltage power supply and the electrodes of the actuator. Power for the internal operation of the device is provided by self-contained power supplies energized by a line cord for connection to 110-volt, 60-Hz lines.

The front panel carries the system controls and indicator lights. The indicator light at the lower left indicates when the system is connected to the 110-volt lines and turned on. Immediately to the right of the light is the POWER ON-OFF switch, serving its indicated function.

Across the upper portion of the front panel are 16 indicator lights. These lights are connected in such a manner as to indicate the presence of voltage applied to the corresponding electrode on the actuator. As the indicator lamps have a minimum operating voltage, their operation may not be reliable at voltage levels below about 150 volts.

The remaining five controls on the front panel affect the operation of the actuator in the following ways:

The ACTUATOR RINGS switch selects the appropriate electronic output for use with actuators utilizing either 10 or 16 electrodes as marked.

The RISE TIME switch allows two modes of operation, one with a relatively slow output voltage waveform rise time and, hence, a reduced maximum stepping rate, and a second setting with a relatively fast rise-time allowing the higher step-rates to be satisfactorily produced. In the slow setting, up to 100 steps per second are available. In the fast setting, up to 1000 steps per second are available. In the fast setting the electronic system draws considerably more current from the high voltage power supply and this must be taken into account to prevent overloading of the power supply.

The use and effect of the FORWARD-OFF-REVERSE switch is self explanatory. It controls the direction of propagation of the pulse train along the actuator length and, therefore, the direction of the produced step motion.

The stepping rate is controlled by two STEP/SEC controls. The first is the COARSE control, a four-position rotary switch that gives stepping rates as labeled. These stepping rates are produced with the FINE rate control in the full clockwise position. The FINE rate control is a variable control that can slow the stepping rate by as much as a factor of 10. This control arrangement gives a continuously variable stepping rate ranging from 1/10 step per second up to 1000 steps per second. The electronic system is so designed that the stepping rate is independent of whether a 10-electrode or 16-electrode actuator is being operated.

The rear panel carries the 110-volt ac line cord 1/2-ampere fuse, actuator cable connector, and three binding posts. The three binding posts are stacked vertically, with the upper post connected to the shaft of the actuator, the center post to the system ground, and the lower post to the input connection for the high voltage power supply. This power supply is connected between the center and lower binding posts with the positive polarity connected to the lower post.

If the actuator is to be operated with no bias voltage applied to the device, the upper binding post is connected to the center binding post. This electrically grounds the actuator shaft. If it is desired to operate the actuator with a bias, an additional high voltage power supply is connected between the upper two binding posts. The polarity connected to the upper binding post will be the polarity of the shaft relative to the electrodes. If the upper post is made negative, the crystal will expand and the interference fit will be reduced. The converse is true if the upper post is made positive.

The connector for the cable between the electronic drive system and the actuator has each pin numbered. Those numbered 1 through 16 are used for the connections to the actuator electrodes. The number of the pin corresponds to the number of the front panel indicator light, counting from the left end, and the number of the electrode on the actuator in progression from one end to the other. Pin number 17 is used for the return connection from the actuator shaft.

NASA-Langley, 1970 —— 14 CR-1658